



Building Integration of a Solar Air Heating System: Transfer Report

Fernando Superbi Guerreiro, BSc, MSc

Supervisors: Dr. Mick McKeever, Prof. David Kennedy, Prof. Brian Norton

School of Electrical and Electronic Engineering

Technological University Dublin

Republic of Ireland

LIST OF SYMBOLS

Acronym

CFD	Computational Fluid Dynamics
CPC	Compound Parabolic Concentrator
IACPC	Inverted Absorber Compound Parabolic Concentrator
ITA	Inverted Transpired Absorber
ODE	Ordinary Differential Equation
PV	Photovoltaic
SEH	Square Elliptical Hyperboloid

Latin

$\overline{W}_{\text{glaz}}$	Glazing characteristic length (m)
A'_{abs}	Absorber area without the holes (m^2)
A	Area (m^2)
C_p	Specific heat (J/kg.K)
C	Geometric concentration ratio
d_{air}	Air density (kg/m^3)
dx	Displacement in x (m)
dy	Displacement in y (m)
e_i	Single ray's energy
ET	Equation of time (min)
f	Focal distance (m)
G_{air}	Mass airflow rate based on the absorber area ($\text{kg/m}^2.\text{s}$)
g	Acceleration of gravity (9.81 m/s^2)
I_B	Beam solar radiation (W/m^2)
I_D	Diffuse solar radiation (W/m^2)

I_T	Global solar radiation (W/m^2)
k_{air}	Air thermal conductivity ($\text{W}/(\text{m}\cdot\text{K})$)
L_{col}	Collector length (m)
l_{local}	Local longitude (deg.)
l_{st}	Standard time meridian for the local time zone (deg.)
MAE	Mean absolute error 
M	Mass (kg)
N_{obs}	Number of observations
N_{rays}	Number of rays from the aperture
Nu	Nusselt number
n	Day number
Pr	Prandtl number
$Q_{L,1}$	Heat loss rate from the absorber (J/s)
$Q_{L,2}$	Heat loss rate from the glazing (J/s)
Q_u	Useful energy rate transferred to the airflow (J/s)
r_{acc}	Ray acceptance
Ra	Rayleigh number
Re	Reynolds number
S	Solar radiation rate absorbed (J/s)
T_c	Temperature at the surroundings of the glazing (K)
t_{LST}	Local standard time (h)
t_{st}	Solar time (h)
T	Temperature (K)
t	Time (s)
U_L	Overall heat loss coefficient ($\text{W}/(\text{m}^2\text{K})$)
U	Internal energy (J)
v	Air velocity (m/s)
W	Width (m)
x_{apt}	x-coordinate of both parabolas at the aperture
X_{exp}	Experimental or observed value of the variable X
X_{sim}	Simulated or predicted value of the variable X
$y_{\text{apt,lower}}$	y-coordinate of the lower parabola at the aperture
$y_{\text{apt,upper}}$	y-coordinate of the upper parabola at the aperture
H	Height (m)

h	Heat transfer coefficient (W/m ² .K)
R	Thermal resistance (K/W)

Greek

α	Absorptivity
α_{P1}	Upper parabola axis angle (deg.)
α_{P2}	Lower parabola axis angle (deg.)
α_s	Solar altitude angle (deg.)
β	Glazing inclination angle (deg.)
β_{th}	Volume expansion coefficient of the air (K ⁻¹)
Δt	Time step (s)
δ_s	Solar declination angle (deg.)
η_o	Optical efficiency
η_R	Reflective efficiency
η_{th}	Thermal efficiency
γ_s	Solar azimuth angle (deg.)
ν_{air}	Air kinematic viscosity (m ² /s)
ω_s	Solar hour angle (deg.)
$\bar{\eta}_o$	Average optical efficiency
$\bar{\eta}_R$	Average reflective efficiency
$\bar{\tau}_{glaz}$	Average glazing light transmittance
ϕ	Latitude angle (deg.)
ρ_{ref}	Reflector reflectance
ΔT_m	Logarithmic mean difference temperature (K)
ℓ	Hole pitch (m)
φ_h	Hole size (m)
φ_p	Absorber porosity 
σ	Stephan-Boltzmann constant ($5.67 \cdot 10^{-8}$ W/m ² .K ⁴)
τ	Light transmittance
θ_{acc}	Angular acceptance
θ_a	Parabola half acceptance angle (deg.)
θ_i	Incidence angle at the glazing surface (deg.)
θ_R	Angle of rotation (deg.)
ε	Infra-red emissivity

ε_{eff}	Effective emissivity
ξ	Fraction of total solar radiation accepted

Subscripts

abs	Absorber
amb	Ambient
apt	Aperture
C1	Convection from absorber to glazing
C11	Convection from absorber to bottom of tertiary section
C12	Convection from bottom of tertiary section to glazing
C2	Convection from glazing to ambient
glaz	Glazing
h	Hole
HX	Convection from absorber to airflow
in	Air at the inlet
out	Air at the outlet
R1	Radiation from absorber to glazing
R2	Radiation from glazing to ambient
TS	Tertiary section
w	Wind

TABLE OF CONTENTS

	Page
List of Figures	4
List of Tables	8
1 Introduction	9
1.1 Aim and objectives of the research	10
1.2 Significant New Knowledge to the Research Area	10
1.3 Report Overview	11
2 Literature Review	12
2.1 Compound Parabolic Concentrator (CPC)	12
2.2 Asymmetric CPC	14
2.3 ACPC with Inverted Absorber	17
2.4 Optical systems and Ray tracing technique	19
2.5 Chapter Summary	22
3 Optical Modelling and Design Analysis	24
3.1 Introduction	24
3.2 Concentrator's design specification	27
3.2.1 Primary reflector design	27
3.2.2 Secondary reflector design	30
3.2.3 Tertiary reflector design	31
3.3 Ray Tracing and Optical Modelling	31

3.4 Results and Discussion	36
3.4.1 Effect of the parabolic shape and tertiary section	36
3.4.2 Evaluation of the length on the optical performance	40
3.4.3 Effect of the glazing inclination on the light transmittance	43
3.5 Chapter Summary	44
4 Experimental performance analysis	46
4.1 Materials for the prototype	46
4.1.1 Absorber surface selection	46
4.1.2 Glazing Cover selection	47
4.1.3 Reflector sheet selection	48
4.1.4 Prototype's structure	48
4.2 Instrumentation and experimental unit	49
4.3 Experimental results from the air heating prototype	52
4.3.1 Experimental results at transient state	53
4.3.2 Experimental results at nearly steady state	59
4.4 Chapter summary	61
5 Heat Transfer Modelling and Simulation	63
5.1 Air heating system's heat transfer modelling	64
5.1.1 Absorbed solar radiation terms	66
5.1.2 Radiative heat transfer coefficients	67
5.1.3 Convective heat transfer coefficients	68
5.1.4 Useful energy rate and outlet air temperature	71
5.2 Simulation results and discussion	73
5.2.1 Simulation settings	73
5.2.2 Model validation	75
5.2.3 Thermal characterisation from simulation results	79
5.3 Chapter Summary	83
6 Remaining work	85

References	93
-------------------	-----------

LIST OF FIGURES

2.1	Basic CPC's cross section design in 2D (Duffie and Beckman, 2013)	13
2.2	Truncated and untruncated CPC with a tubular absorber.	14
2.3	Angular acceptance function of a full and truncated CPC. Adapted from Norton et al. (1991).	14
2.4	General design of an asymmetric CPC.	15
2.5	Dielectric ACPC with 78% truncated at the vertical for building integration photovoltaic.	16
2.6	Sketch of the box-type solar cooker employing an ACPC.	17
2.7	Basic CPC geometry with inverted absorber.	17
2.8	Law of reflection applied on a reflecting surface.	19
2.9	The focusing effect of solar beam incident on a solar concentrating mirror.	21
2.10	The focusing effect of solar beam incident on a solar concentrating mirror.	21
2.11	Comparison between the 3D crossed CPC and the 2D CPC.	22
2.12	Cross section of the integrated collector storage system for water heating.	22
2.13	The focusing effect of solar beam incident on a solar concentrating mirror.	23
3.1	Concentrator's cross section view, where: ① is the primary section; ② is the secondary section; and ③ is the tertiary section.	25
3.2	Solar position diagram for 53.35° of latitude.	27
3.3	Parabolas at the initial position (dashed line) and after Affine technique (full line) for the (a) upper and (b) lower parabolas.	28
3.4	Two parabolas assembled to form the untruncated primary section (ABP'Q')	29
3.5	Truncated primary section (ABCD)	29

3.6	Circular reflector drawing with centre (W_{abs} , W_{abs}) and radius W_{abs}	30
3.7	Concentrator's cross section view.	31
3.8	Final concentrator's design in 3D.	32
3.9	Concentrator's orientation in the space and one incoming ray going through the aperture.	32
3.10	Visualisation in 2D of six rays coming through the aperture at an angle α_s	34
3.11	Visualisation in 3D of two sets of six rays coming through the aperture at a particular pair of angles α_s and γ_s	34
3.12	Concentrator's initial design.	37
3.13	Angular acceptance vs. solar altitude angle for the initial design.	37
3.14	Average reflective efficiency <i>versus</i> lower parabola axis angle.	38
3.15	Comparison between concentrators at 60° of α_{P_2} (blue) and at 50° of α_{P_2} (red).	39
3.16	Average reflective efficiency <i>versus</i> tertiary section height for 2D and 3D models.	39
3.17	Ray tracing diagram in 2D and energy distribution over the absorber width with no tertiary section.	40
3.18	Ray tracing diagram in 2D and energy distribution over the absorber width at 72.5 mm of tertiary section.	41
3.19	Ray tracing diagram in 2D and energy distribution over the absorber width at 145 mm of tertiary section.	41
3.20	Average reflective efficiency <i>vs.</i> L_{col}	42
3.21	Cost and weight of reflector as function of the collector length.	42
3.22	Average transmittance versus glazing inclination.	43
3.23	Average transmittance versus glazing inclination.	44
3.24	Cross section of the concentrator's final design.	44
4.1	Morphology image of carbonfibre sample taken at magnification of 15x.	47
4.2	Parts of the prototype's structure and assembled	50

4.3	Positions of the 12 thermocouples placed on the absorber surface (dimensions in mm).	50
4.4	Position of the three thermocouples placed on the glazing surface (dimensions in mm).	51
4.5	Schematic diagram of the experimental unit.	52
4.6	Open loop outdoor experimental unit.	52
4.7	Experimental results from 2 nd and 3 rd July at zero airflow.	54
4.8	Experimental results from 9 th June at 0.040 kg/m ² .s.	54
4.9	Hourly performance from 9 th June at 0.040 kg/m ² .s.	55
4.10	Experimental results from 22 nd June at 0.055 kg/m ² .s.	56
4.11	Hourly performance from 22 nd June at 0.055 kg/m ² .s.	56
4.12	Experimental results from 29 th May at 0.070 kg/m ² .s.	57
4.13	Hourly performance from 29 th May at 0.070 kg/m ² .s.	57
4.14	Experimental results from 31 st May at 0.090 kg/m ² .s.	58
4.15	Hourly performance from 31 st May at 0.090 kg/m ² .s.	58
4.16	Experimental results from 28 th June at 0.115 kg/m ² .s.	59
4.17	Houly performance from 28 th June at 0.115 kg/m ² .s.	60
4.18	Thermal efficiency curve.	61
4.19	Graphs of thermal efficiency (a), and airflow temperature rise (b) at different airflow rates at nearly steady state condition.	62
5.1	Block diagram of the heat transfer model	64
5.2	Thermal network to illustrate heat flows in the air heater.	65
5.3	Convective heat transfer taking place within the tertiary section and at the surroundings of the glazing (whose coefficients are h_{c11} and h_{c12} , respectively).	69
5.4	Carbon fibre magnified image and drawing for indication of geometric parameters.	72
5.5	(a) Experimental and simulated results, (b) residues of T_{out} , and (c) residues of Q_u from 09 th June at 0.04 kg/m ² .s.	76

5.6 (a) Experimental and simulated results, (b) residues of T_{out} , and (c) residues of Q_u from 22 nd June at 0.055 kg/m ² .s.	77
5.7 (a) Experimental and simulated results, (b) residues of T_{out} , and (c) residues of Q_u from 29 th May at 0.07 kg/m ² .s.	78
5.8 Experimental and simulated results from 31 st May at 0.09 kg/m ² .s.	79
5.9 (a) Experimental and simulated results, (b) residues of T_{out} , and (c) residues of Q_u from 28 th June at 0.115 kg/m ² .s.	80
5.10 Residues vs. solar radiation for (a) T_{out} , and (b) Q_u	80
5.11 Residual cumulative frequency distribution of (a) T_{out} , and (b) Q_u	81
5.12 Simulated T_{out} at the five different airflow rates used in the tests, under conditions of 30 th June.	82
5.13 (a) Surface and (b) contour plot of air temperature rise vs. solar radiation and airflow rate.	82
5.14 (a) Surface and (b) contour plot of useful energy vs. air temperature rise and airflow rate.	83
5.15 Thermal efficiency curves for experimental and simulated data.	83

LIST OF TABLES

3.1	Expressions for the parabolas' parameters.	28
3.2	Geometric parameters of the concentrator to be fabricated.	45
4.1	Carbon fibre weaver properties.	47
4.2	Glazing cover properties.	48
4.3	<i>MiroSun</i> reflector properties (Alanod, 2016).	49
4.4	Mass and volumetric flow rates calculated at each voltage input.	51
5.1	Model parameters values used in the heat transfer modelling.	74

CHAPTER 1

INTRODUCTION

Solar thermal systems for water and air heating are well established technologies. Their use promote environmental sustainability, as it reduces the need to provide heat by combusting fossil fuels and therefore contributing to reducing greenhouse gas emissions.

The solar collectors or entire solar thermal systems in many locations are usually installed on roofs rather than forming an integral part of the building  roof or façade. The consequences of non-integration may include the aesthetical unacceptance and high expenditure for installation which leads to unaffordable initial capital cost. The full building integration has the potential to increase significantly the prevalence of solar thermal systems as well as to reduce, or eliminate, the barriers existing to their adoption, improving both aesthetic appearance and economic viability.

Solar air heaters are devices that convert solar thermal energy into hot air to be used for many applications: space heating of buildings and dwellings, timber seasoning, and drying of agricultural products (Alta et al., 2010). To deliver hot air flow at temperatures higher than those from flat-plate collectors, concentrators offer a reasonable alternative (Duffie and Beckman, 2013). They are designed to receive solar radiation through an aperture area and direct it towards a smaller absorber area by employing a reflective material (Goswami, 2015).

1.1 Aim and objectives of the research

The research aim to design and characterise a building integrated air heating system comprising several collectors capable of receiving 8 hours of solar radiation per day to heat air flow in the summer for  cooling. The specific objectives of the research are to:

- build an optical model to design the collector (and an assembly of multiple units) then characterise it using a ray tracing technique in 2D and 3D;
- undertake field tests for the collectors characterisation to achieve a well understanding of the variables that affect its performance;
- simulate the collector's thermal behaviour through a transient heat transfer modelling and a CFD analysis;
- fabricate a prototype and, via experiments, characterise its thermal performance;
- validate the heat transfer model using the experimental results; 
- build a second prototype, connect both together and perform outdoor experiments;
- model, simulate and control the system;

1.2 Significant New Knowledge to the Research Area

The significant new contribution to knowledge in the area of solar thermal energy for air heating are:

- Design of an Asymmetric CPC considering period of operation, concentration ratio, size and material cost and optical characterisation of the concentrator using a 3D ray tracing algorithm;
- Optical performance of multiple units accounting for over-shading and physical size;
- Thermal modelling and simulation of connected concentrators in transient state with analysis of the cavity design responsible for suppressing convective losses;
- Operation of two units connected for thermal characterisation to achieve understanding of the variables that affect the system's performance;

- System control to maintain airflow temperature by manipulating airflow rate for standalone and multiple units;
- CFD simulation to understand the convective fluid motion associated with the heat transfer operation in a single collector;

1.3 Report Overview

Chapter 1 describes the introduction of the topic which is followed by the research motivation and then to establish the problem statement. The main aim of the research, specific objectives and methodology used are presented here.

Chapter 2 presents a literature review that identifies the state-of-the-art of conventional concentrating collectors. It focuses on optical concentrator design and building integrated solar collectors. Optical concentrator design and concentrator integrated with solar collectors were studied to identify possible ways to concentrate solar radiation on an inverted absorber.

Chapter 3 presents the design of the solar air heating concentrator as well as the development of a model to calculate its optical efficiency. It also depicts details of the concentrator's geometric specification. A 2D and 3D ray tracing technique implemented in Matlab software were used in this research to calculate the energy distribution at the absorber surface.

Chapter 4 describes the components for both prototypes fabrication and the experimental results of the tests under different levels of airflow rate. The performance of the system depends on wind speed, solar radiation, inlet air and ambient temperatures. The temperature of the outlet air and absorber showed significant rise during the experiments.

Chapter 5 depicts a heat transfer model developed to characterise and simulate the thermal performance of the proposed solar air heater in operation. This model was also used to analyse the effect of the tertiary section and estimate the outlet airflow temperature. Simulations in CFD will also be conducted in order to understand how the heat is transferred from the absorber to the airflow.

CHAPTER 2

LITERATURE REVIEW

This chapter reviews the literature on optical concentrator design and subsequent optical performance. Optical concentrator designs and concentrators integrated with solar collectors were studied to identify possible ways to concentrate solar radiation on an inverted absorber.

2.1 Compound Parabolic Concentrator (CPC)

The compound parabolic concentrator (CPC) is a non-imaging solar concentrator that has the advantages (compared to focusing ones) of i) there being no need for solar diari^{tracking}, and ii) the ability to collect a portion of diffuse radiation Winston (1974). The main purpose of a CPC is to collect as much incident solar energy as possible then direct that energy to either a heat exchanger for heating or directly to PV cells for electricity production (Jaaz et al., 2017).

A CPC cross section is shown in Figure 2.1. The concentrator accepts direct solar radiation within a certain angular acceptance range through the aperture to be focused onto a receiver/absorber by reflection at the two symmetrical parabolic reflectors.

The geometrical concentration ratio is defined as the ratio of the aperture area to the absorber area. This parameter has an upper limit calculated by Eq. (2.1) based on the second law of thermodynamics, where the half-acceptance angle θ_a is the angular limit over which radiation is fully accepted without moving all or part of the collector (Rabl, 1976a). If the reflectors are specular, all the solar rays incident at angles within the

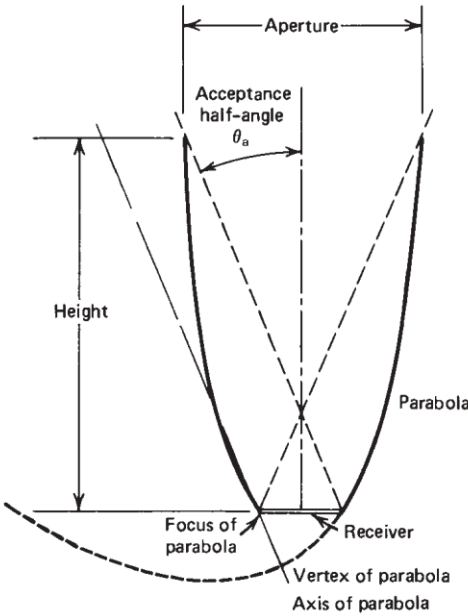


Figure 2.1: Basic CPC's cross section design in 2D (Duffie and Beckman, 2013).

acceptance range (between $\pm\theta_a$) will reach the absorber surface. If a high concentrating CPC is needed, the acceptance angle should be small at the cost of receiving less solar radiation.

$$CR = \frac{1}{\sin\theta_a} \quad (2.1)$$

The full geometry of compound parabolic troughs are high, which demand high reflector costs. To address this, most concentrators are truncated to reduce costs and weight (Figure 2.2 shows the untruncated and truncated versions of the same CPC). The effect of truncation on the design parameters concentration ratio, height-aperture width ratio (H_{CPC}/W_{apt}) and reflector length has been presented by graphs or equations by McIntire (1979) and Rabl (1976b). Figure 2.3 shows the angular acceptance function for an untruncated (full) CPC and for a truncated configuration. 

Carvalho et al. (1985) derived analytic expressions of angular acceptance range and evaluated the yearly collectable energy as function of the truncation level. Hence they could observe that truncated concentrators accept solar rays at broader incident angles and collect more solar energy due to reduction of reflections. Francesconi and Antonelli (2018) simulated a five-CPC assembly's performance in CFD; they concluded that the

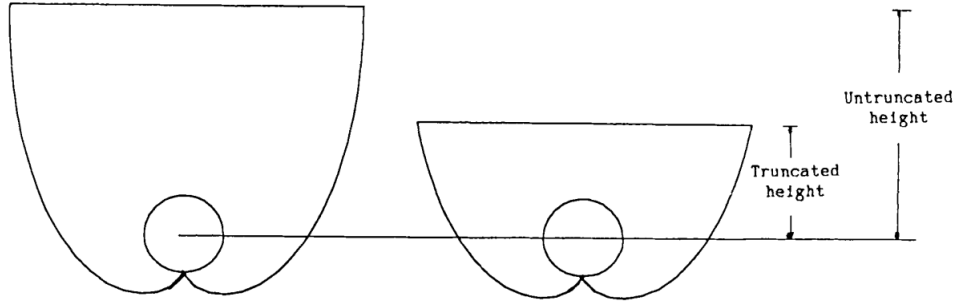


Figure 2.2: Truncated and untruncated CPC with a tubular absorber.

concentration ratio reduction from 2.0 to 1.96 resulted in a 2% increase of the system's thermal efficiency.

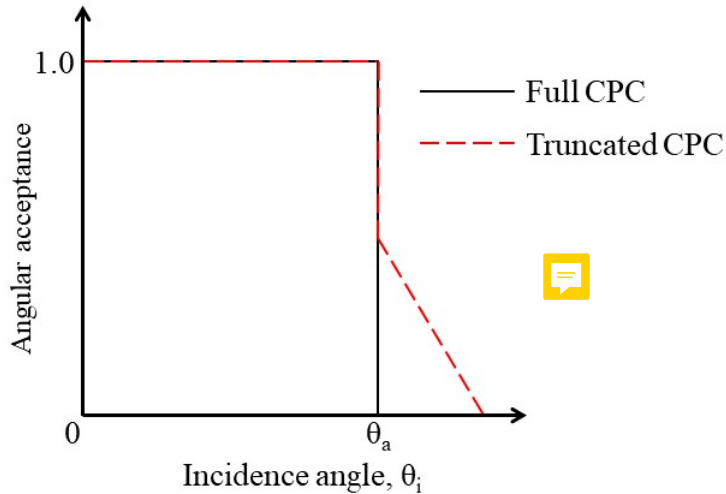


Figure 2.3: Angular acceptance function of a full and truncated CPC. Adapted from Norton et al. (1991).

2.2 Asymmetric CPC

CPCs are symmetric in the original design with two equal half acceptance angles in relation to the optical axis. The design evolution has led to the asymmetric compound parabolic concentrator (ACPC) introduced by Rabl (1976b), where the CPC is a particular case of its asymmetric counterpart. Figure 2.4 shows a general cross section design of an ACPC, where the acceptance angle is $2\theta_a = \alpha_{PU} + \alpha_{PL}$ and the geometric concentration ratio is also the ratio of the areas. The axis of upper (lower) parabola subtends an angle $\alpha_{PU}(\alpha_{PL})$ with the normal of absorber. Therefore, broader angular acceptance range and

designs with higher concentration ratios can be achieved due to the asymmetry (Tian et al., 2018). The ACPC is found to be a suitable solution for building integration at vertical facades because of design flexibility and the ability to collect 40% of solar radiation even outside the angular acceptance range (Zacharopoulos et al., 2000).

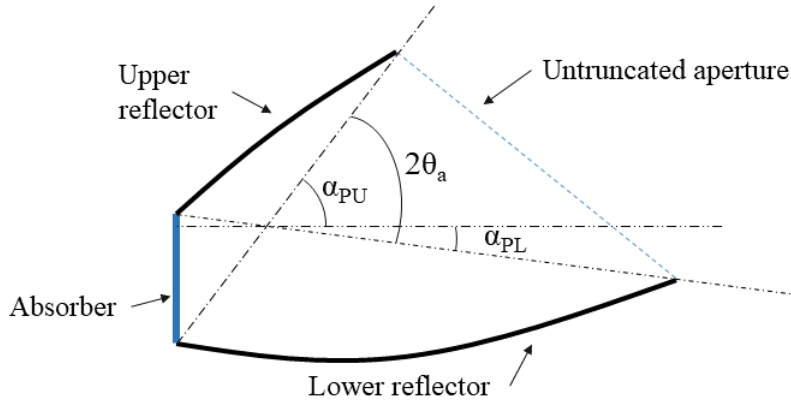


Figure 2.4: General design of an asymmetric CPC.

Asymmetric concentrator systems were designed as an alternative to the symmetric versions as they present the following advantages (Mills and Giutronich, 1978):

- Improvement in the solar concentration vs. operation-time relation to compensate lower solar radiations in early morning and late afternoon, allowing more uniform output;
- Greater operational flexibility for unexpected variations in energy demand and higher yearly average energy input per reflector surface area.

Researchers have studied this type of concentrator in details. Zacharopoulos et al. (2000) analysed the optical performance of a 3D dielectric ACPC with a 78% truncation at the vertical compared to a symmetric version (Figure 2.5). The analysis showed that the asymmetric concentrator design is more suitable for use in a building facade compared to a symmetric one. Tripanagnostopoulos et al. (2000) proposed a collector design based on a truncated asymmetric CPC reflector, consisting of a parabolic and a circular part. This design features a flat bifacial absorber installed at the upper part of the collector, parallel to the glazing to form a thermal trap space between the reverse absorber surface and the circular part of the mirror. The experimental results showed that the proposed

collector could achieve a maximum efficiency of 71% and a stagnation temperature of 180 °C. Mallick et al. (2006) presented a comparative experimental characterisation of a non-imaging line-axis 0 – 50° acceptance-half angles asymmetric compound parabolic photovoltaic concentrator (ACPPVC-50) suitable for vertical building facade integration with its non-concentrating counterpart. Mallick et al. (2007) performed an optical and heat transfer analysis for a truncated ACPC of concentration ratio 2.01 suitable for photovoltaic applications with the aim of using airflow to alleviate temperature at the solar cells. Sarmah et al. (2011) compared the optical performance of three dielectric ACPC designs (all truncated with concentration ratio of 2.82) of acceptance angles 0 – 55°, 0 – 66°, and 0 – 77°, in order to optimize the concentrator for building facade photovoltaic applications in northern latitudes ($> 55^{\circ}\text{N}$). Based on the annual solar energy collection by all the designs, it was found that the system of acceptance angles 0 – 55° is more optically efficient and can collect more energy compared to the other two. Harmim et al. (2012) constructed and evaluated the performance of a box-type solar cooker equipped with an ACPC of concentration ratio 2.12 which sketch is shown in Figure 2.6. The reflectors were designed so that the absorber could receive solar rays of which the solar altitude angle was between 30 and 75°.

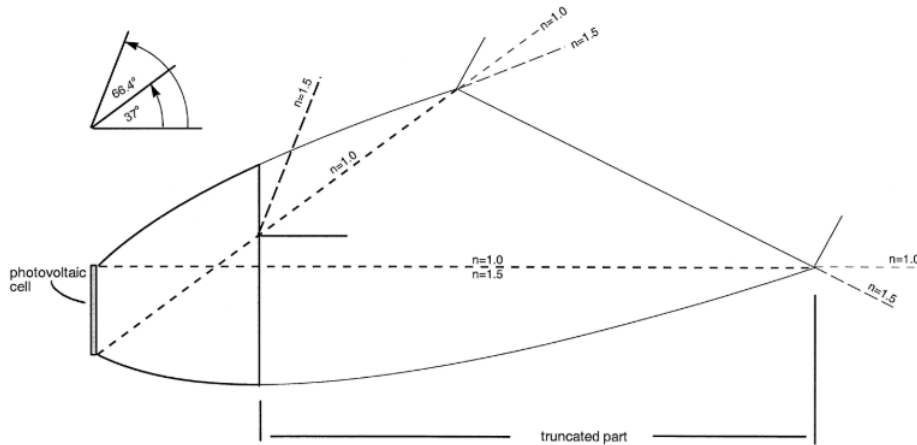


Figure 2.5: Dielectric ACPC with 78% truncated at the vertical for building integration photovoltaic.

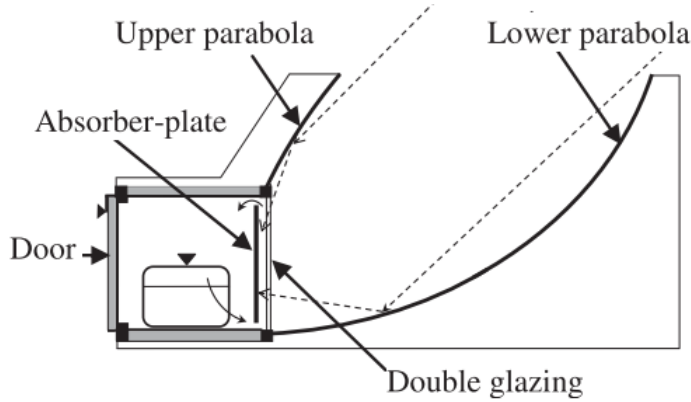


Figure 2.6: Sketch of the box-type solar cooker employing an ACPC.

2.3 ACPC with Inverted Absorber

Collectors employing inverted absorber in which solar radiation is reflected from below onto the downward-facing absorbing surface have been proposed by Rabl (1976b). They are also called inverted absorber asymmetric compound parabolic concentrator (IACPC). Such collectors (shown in Figure 2.7) have been able to achieve higher absorber temperatures by suppressing convection losses (Kienzlen et al., 1988). This is due to the formation of thermally stratified air layers below the absorber surface (Norton et al., 1991). The configuration also provides radiation suppression as the downward facing absorber surface does not view the aperture directly (Eames et al., 2001).

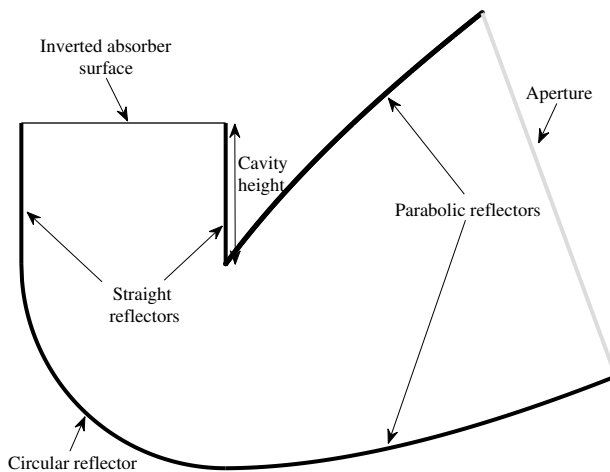


Figure 2.7: Basic CPC geometry with inverted absorber.

Researchers have reported studies aiming to evaluate the performance of this type of

collector. Kothdiwala et al. (1996) developed a ray trace model to simulate and optimise the optical performance. This model considered the effect of beam and diffuse radiation separately. They verified that the beam optical efficiency decreases with the increase of the cavity height and concentration ratio.

Eames et al. (1996) predicted the thermo-physical performance of the IACPC system. In their study, the energy flux at the absorber was determined by a ray trace technique and a finite element model was developed to predict the system's thermo-fluid behaviour. Kothdiwala et al. (1997) conducted indoor experiments under a solar simulator to analyse the performance of the IACPC, which was copper sheeting onto a tubing along the concentrator's long axis. The tests were carried out using water as the flowing fluid at various cavity heights. Kothdiwala et al. (1999) compared a tubular absorber CPC with glass envelope to an IACPC at different cavity heights, both for water heating purposes. They concluded that the appropriate use of an absorber configuration on the IACPC maximises convection suppression and minimises optical losses. Furthermore, at the optimum configuration, this system outperforms the other compared in this study. Eames et al. (2001) simulated the performance of an IACPC by using a combined ray trace and finite element computational fluid dynamics model previously developed by Eames and Norton (1993). This model was validated by direct comparison with experimental results.

Tiwari and Suneja (1998) modelled and evaluated the performance of an inverted absorber solar still for distillation purpose. They found that this inverted configuration provided double the hourly yield compared to a conventional still. The experimental comparison between an inverted absorber solar still and conventional single slope solar at various water depths has been conducted by Dev et al. (2011). They found that the water temperature in the basin of an inverted absorber solar still is higher than the conventional one.

In order to suppress convection losses, Smyth et al. (2005) investigated the use of transparent baffles at different locations within the collector cavity; the system consisted of an integrated collector storage solar water heater (ICSSWH) mounted in the cavity of an IACPC. Shams et al. (2016) designed and fabricated a concentrating transpired air

heating system comprised by an IACPC with a perforated absorber. This collector had the absorber surface made of carbon fibre placed at a fixed cavity height, a glazed aperture, a concentration ratio of 2.0, and was experimentally tested at different air flow rates. 

2.4 Optical systems and Ray tracing technique

A major part of the design and analysis of concentrating collectors involves ray tracing techniques, which are algorithms to simulate sunlight rays passing through an optical system. Ray tracing analysis is an important method adopted in optical systems to obtain the optical performance for complex geometries regarding direct and diffuse solar radiation (Ali et al., 2013). When a ray hits a real reflecting surface, most part of its energy will be reflected. To formulate a suitable ray tracing procedure, the law of reflection can be applied into vector form (Winston et al., 2005). Figure 2.8 shows the unit vectors r_{inc} and r_{ref} along the incident and reflected rays and a unit vector r_n at the normal point of incidence into the reflecting surface. The law of reflection is expressed by Eq. (2.2):

$$r_{ref} = r_{inc} - 2(r_n \cdot r_{inc})r_n \quad (2.2)$$

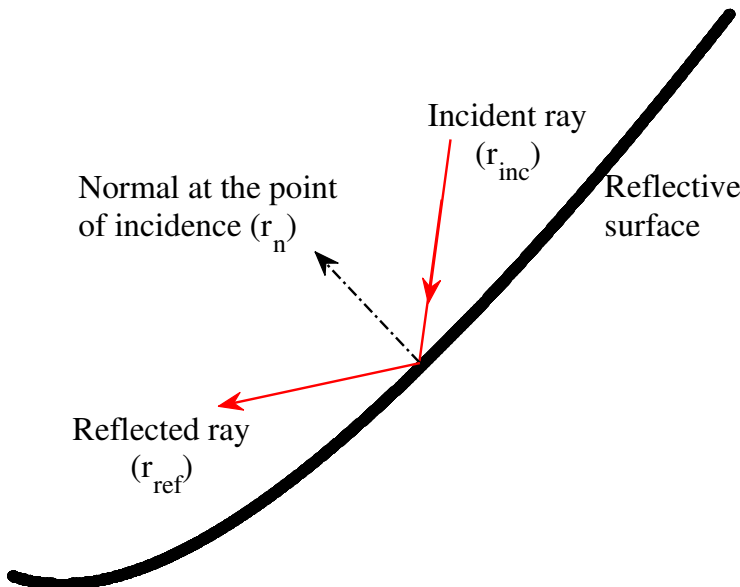


Figure 2.8: Law of reflection applied on a reflecting surface.

Several concentrating systems  have been proposed and optically analysed for differ-

ent purposes and reported in literature in details. The analysis can provide:

- Average number of reflections before the incoming rays reach the absorber plate (Shams, 2013; Benrejeb et al., 2016);
- Optical efficiency as a function of the incidence angle (Kothdiwala et al., 1996; Souliotis et al., 2011);
- Visualisation of rays' path and reflection points (Mallick and Eames, 2007; Ratishmith et al., 2014; Ustaoglu et al., 2016);
- Intensity of energy distributed at the absorber surface (Sellami and Mallick, 2013; Ali et al., 2014; Bellos et al., 2016);
- System's optical characterisation for further thermal modelling and simulation (Mallick and Eames, 2007; Shams, 2013; Bellos et al., 2016);
- Comparison between two or more systems (Zacharopoulos et al., 2000; Sarmah et al., 2011; Wu, 2009).

Bellos et al. (2016) performed an optical analysis and optimised the geometry of a CPC with an evacuated tube, where this design is considered to be optimum because all the reflected rays reach the receiver. They also calculated the optical losses at different solar angles. The authors also indicate the need of tracking the collector in order to minimise the incident angle. Qin et al. (2013) designed and optimised the geometry of an aspheric reflecting solar concentrator (Figure 2.9) with the aim of focusing sunlight on a narrow line segment. To do so, they used a particular aspheric equation in three dimensions together with the law of reflection to trace the incident rays.

Using the OpticsWorks software, Sellami et al. (2012) performed an optical analysis and developed a novel geometry of a 3D static concentrator in form of a square elliptical hyperboloid (SEH) to be integrated in glazing windows or facades for photovoltaic application. The SEH of concentration ratio 4.0 was optically optimised considering different incident angles of the incoming light rays. Ali et al. (2013) evaluated the optical performance of a static 3D elliptical hyperboloid concentrator, as shown in Figure 2.10, using a ray tracing software called Optis. Effective concentration ratio, optical efficiency and geometric parameters were analysed. Furthermore, the geometry was optimised to improve the overall performance.

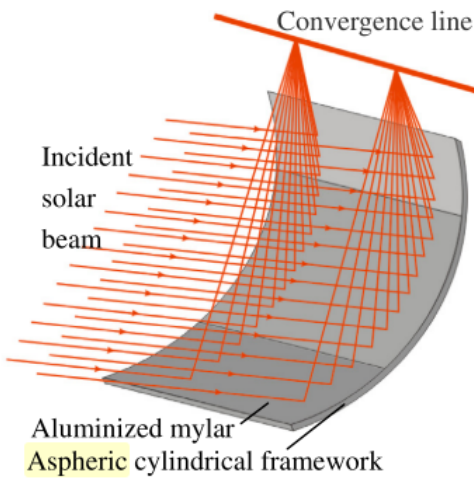


Figure 2.9: The focusing effect of solar beam incident on a solar concentrating mirror.

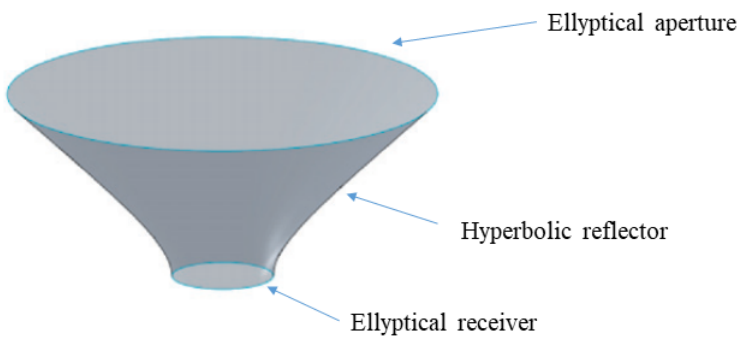


Figure 2.10: The focusing effect of solar beam incident on a solar concentrating mirror.

Abdullahi et al. (2015) used a ray tracing technique to investigate the effect of the receiver size on the optical efficiency of a CPC with two tubular receivers aligned horizontally and vertically. Sellami and Mallick (2013) developed a 3D ray trace code in Matlab to determine the beam optical efficiency and the energy distribution of a 3D crossed CPC (CCPC) for different incident angles. Figure 2.11 shows a CCPC geometry compared to a 2D CPC. The authors found that this type of CPC is an ideal concentrator for a half-acceptance angle of 30° and concentration ratio of 3.6.

Benrejeb et al. (2015) used mathematical equations describing the geometric design of an integrated collector storage system where its cross section is shown in Figure 2.12. Therefore, an optical study was given with details to achieve the ray tracing technique results and the energy flux distribution on the absorber surface. Furthermore the optical results were used as inputs in the heat transfer model to simulate the temperature of the water inside the absorber.

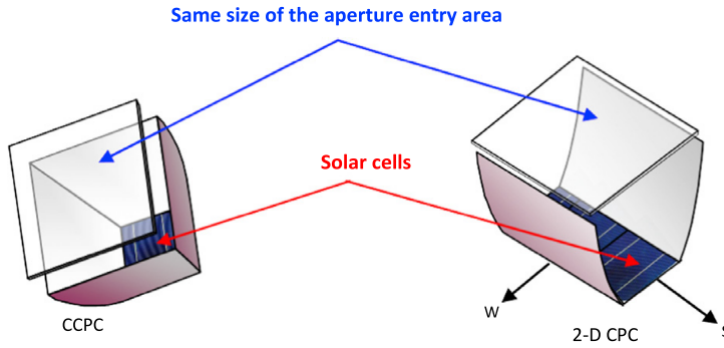


Figure 2.11: Comparison between the 3D crossed CPC and the 2D CPC.

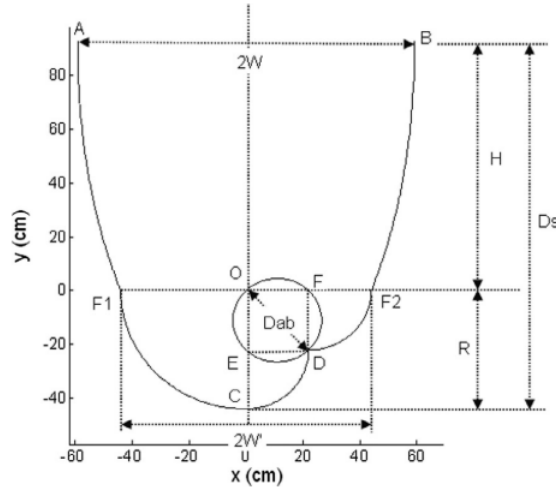


Figure 2.12: Cross section of the integrated collector storage system for water heating.

Abu-Bakar et al. (2014) proposed a new type of concentrator, known as the rotationally ACPC which is shown in Figure 2.13, for use in building integrated systems for PV applications, where the geometrical concentration gain and the optical concentration gain were evaluated. From the simulations, it has been found that the concentration could produce an optical concentration gain as high as 6.18 when compared with the non-concentrating cell depending on the half-acceptance angle.

2.5 Chapter Summary

In this chapter, a review of published research on symmetric, asymmetric and inverted absorber parabolic concentrators was undertaken. The review also regards the optical systems reported and how the optical analysis can be undertaken in order to characterise them. There has been no previous relevant research reported on an inverted asym-

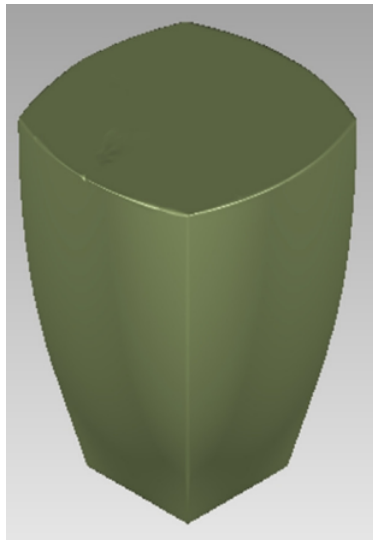


Figure 2.13: The focusing effect of solar beam incident on a solar concentrating mirror.

metric CPC collector to heat air for building integration. The system was designed to minimise heat losses and deliver airflow at a temperature set by an application. Considering high latitude locations, an integrated ACPC can increase the density of solar radiation reaching the absorber area. A highly reflective concentrator can allow solar radiation to be reflected onto the inverted absorber.

CHAPTER 3

OPTICAL MODELLING AND DESIGN ANALYSIS

The aim of this chapter is to define the design of a concentrator for building an air heating system using optical analysis with the assistance of a ray tracing technique based on an optical modelling. The specific objectives are to:

- Develop a ray tracing technique in 2D and in 3D, and an optical model by using an algorithm implemented in Matlab[®];
- Evaluate the effect of the parabolic reflectors and the tertiary section height on the optical performance;
- Assess the concentrator's length and its impact on the reflector cost;
- Analyse the influence of the glazing inclination on the light transmittance;
- Characterise the optical profile of the concentrator used for experimental tests.

3.1 Introduction

The proposed solar concentrator is a combination of an inverted transpired absorber and an asymmetric compound parabolic concentrator (ACPC), where its cross-section view can be seen in Figure 3.1. The concentrator can be divided into the following sections:

- **Primary section ①:** This consists of the aperture and two asymmetric parabolic reflective surfaces. These reflectors are responsible for reflecting solar rays coming

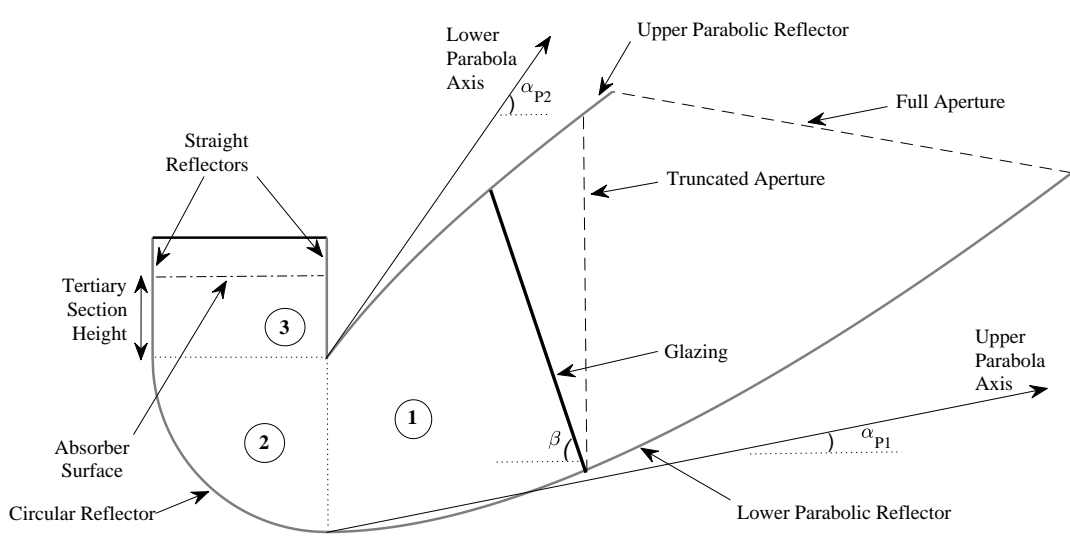


Figure 3.1: Concentrator's cross section view, where: ① is the primary section; ② is the secondary section; and ③ is the tertiary section.

through the aperture and concentrate them to the next section;

- **Secondary section ②:** This comprises a circular reflector, whose radius is the absorber width, that reflects all the incoming rays upwards towards the tertiary section;
- **Tertiary section ③:** This consists of a cavity composed of two vertically straight reflectors that receives the solar rays from the secondary section and directs them to the absorber surface.

The absorber surface is inverted to reduce radiation loss and stabilise the thermal layers below, which improves the heat transfer mechanism. Additionally, it is perforated to allow the airflow to percolate through the holes, thus enhancing the heat transferred from the absorber (Shams et al., 2016).

The concentrator's aperture is set at the vertical position (at the truncation line indicated in Figure 3.1) so that shading can be avoided when two or more collectors are stacked on a wall. The actual aperture width (W_{apt}) will be 330 mm in order to have three collectors stacked on every metre of wall height. The glazing placed in the primary section works as a heat trap, as well as offering protection for the interior of the unit against weather conditions. Its position at a given inclination β seeks to maximise light transmittance over the operation period considered.

Considerations have also been given to the angles of both parabolas axes (α_{p_1} and α_{p_2}), which influence the primary section shape. Those angles also determine the range of solar altitude angle accepted by the system (Zacharopoulos et al., 2000). The selection of all these design variables must take into account the compromise between optical efficiency and geometric concentration ratio to maximise solar radiation collection at the absorber surface.

This solar air heating system is designed to operate for:

- Summer season (from 21/06 to 21/09): day number (n) from 172 to 264;
- 8 hours per day, from 9 am to 5 pm;
- Dublin, Ireland, where the latitude (ϕ) is 53.35° and the longitude (l_{local}) is -6.26° .

Such information are essential to calculate the sun angles in the period of operation. They are obtained from the solar time (t_{st}), which does not coincide with the local standard time. The relationship between these two times is calculated by Eq. (3.1). This difference is due to the deviation between the local longitude and the meridian on which the local standard time is based; and irregularity of the earth's motion around the sun, accounted by the Equation of Time (ET) as a function of the year's day (Goswami, 2015).

$$t_{\text{st}} = t_{\text{LST}} + \frac{4(l_{\text{st}} - l_{\text{local}}) + \text{ET}}{60} \quad (3.1)$$

Therefore, the solar hour angles (ω_s) are obtained from the solar time for each day of operation. Sequentially, the solar altitude and the solar azimuth angles (α_s and γ_s) can be calculated as:

$$\alpha_s = \sin^{-1} (\sin \phi \sin \delta_s + \cos \phi \cos \delta_s \cos \omega_s) \quad (3.2)$$

$$\gamma_s = \sin^{-1} \left(\frac{\cos \omega_s \sin \delta_s}{\cos \alpha_s} \right) \quad (3.3)$$

where the solar declination δ_s is a function of the year's day.

A solar position plot of α_s vs. γ_s at the latitude of Dublin is shown in Figure 3.2, where each graph corresponds to a particular day in the operation period. The values of

α_s and γ_s at any point in time in the operation period will be used as inputs in the optical modelling to be discussed further.

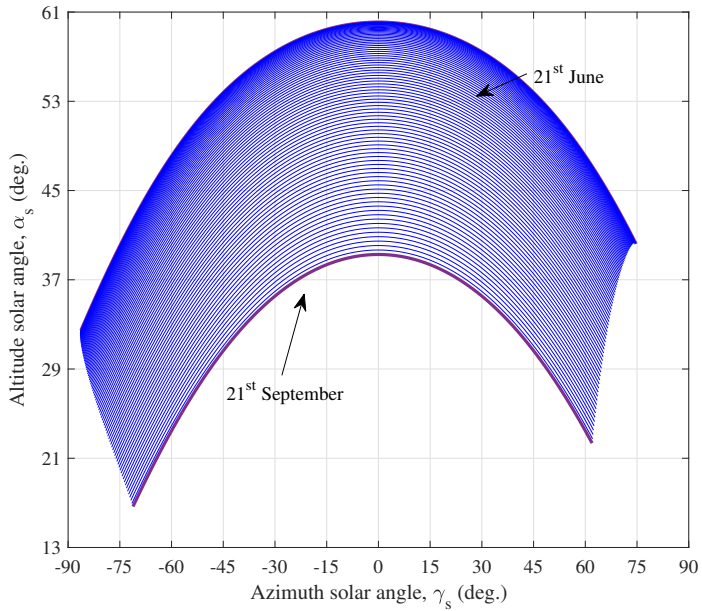


Figure 3.2: Solar position diagram for 53.35° of latitude.

3.2 Concentrator's design specification

This part describes how the reflectors of each section were designed and placed to form the proposed air heating concentrator. The design was performed in Matlab® with the help of SolidWorks® by using positive x-y coordinates.

3.2.1 Primary reflector design

To design the parabolic reflectors of the primary section, the first step is to define the equation of the parabola whose axis is coincident to the y-axis and the vertex set at the origin (0,0):

$$y = \left(\frac{1}{4f}\right)x^2 \quad (3.4)$$

where f is the focal distance (Winston et al., 2005), calculated by Eq. (3.5):

$$f = \frac{W_{\text{abs}}}{2} (1 + \sin \theta_a) \quad (3.5)$$

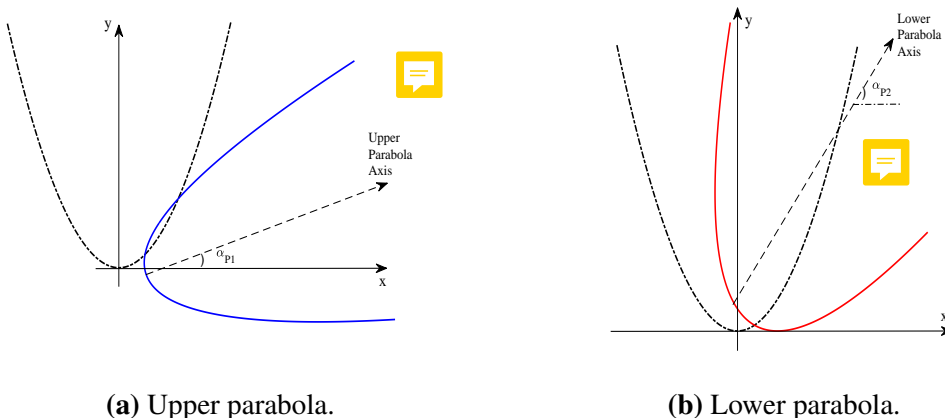
and θ_a is the parabola acceptance angle. The next step is to translate and rotate the parabola to form the primary section. This can be done by using the Affine transformation technique (Duffy, 2016), which consists of applying a matrix multiplication as shown in Eq. (3.6):

$$\begin{bmatrix} x_p \\ y_p \\ 1 \end{bmatrix} = \begin{bmatrix} 1 & 0 & dx \\ 0 & 1 & dy \\ 0 & 0 & 1 \end{bmatrix} \begin{bmatrix} \cos \theta_R & \sin \theta_R & 0 \\ -\sin \theta_R & \cos \theta_R & 0 \\ 0 & 0 & 1 \end{bmatrix} \begin{bmatrix} x \\ y \\ 1 \end{bmatrix} \quad (3.6)$$

 with the parameters dx and dy as the displacements in x and y , respectively, θ_R as the angle of rotation (which is the complement of the parabola axis angle), and x_p and y_p are the new coordinates of the parabola calculated by the Affine transformation technique. The expressions for calculating θ_a , θ_R , dx and dy for each parabola are shown in Table 3.1. They were obtained using basic geometry and sketches in SolidWorks®. After applying the transformation, both parabolas were plotted as shown in Figure 3.3.

Table 3.1: Expressions for the parabolas' parameters.

Parameter	Upper Parabola	Lower Parabola
θ_a	$-\alpha_{p1}$	$2\alpha_{p2} - 90^\circ$
dx	$W_{abs} - f \cos \alpha_{p1}$	 $W_{abs} - (W_{abs} + f) \cos \alpha_{p2}$
dy	$-f \sin \alpha_{p1}$	$(W_{abs} - f) \sin \alpha_{p2}$



(a) Upper parabola.

(b) Lower parabola.

Figure 3.3: Parabolas at the initial position (dashed line) and after Affine technique (full line) for the (a) upper and (b) lower parabolas.

The next step is to arrange the parabolas in the same coordinate system to form the

full or untruncated primary section shape ABP'Q', shown in Figure 3.4 . In this case, the point B should intercept the x-axis and the vertical segment AB should be equal the absorber width (W_{abs}), as it is the section end. The full aperture indicated by the segment P'Q' is obtained according to the parabola axes angles.

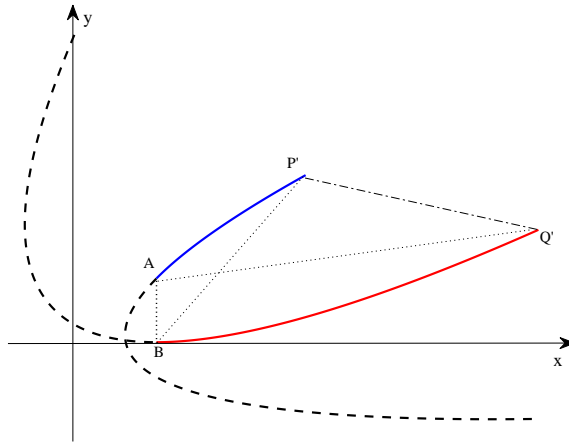


Figure 3.4: Two parabolas arranged to form the untruncated primary section (ABP'Q'). Dashed curves of the parabolas were eliminated.

However, as mentioned earlier, the aperture was set to be vertical and therefore the section is truncated whose line is indicated by the segment CD in Figure 3.5. The curves AC and BD then represent the upper and lower reflectors, respectively.

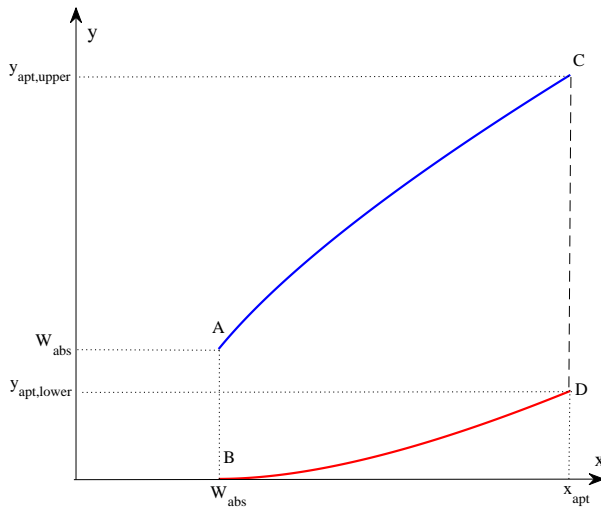


Figure 3.5: Truncated primary section (ABCD), where AC and BD are the upper and lower reflectors, respectively.

For this section the coordinate limits are:

Upper reflector: $W_{abs} \leq x \leq x_{apt}$ and $W_{abs} \leq y \leq y_{apt,upper}$

Lower reflector: $W_{abs} \leq x \leq x_{apt}$ and $0 \leq y \leq y_{apt,lower}$



In order to undertake the optical analysis, a 20th degree polynomial was fit to model each parabolic reflector, and the polynomial equations are presented in Eqs. (3.7) and (3.8) as follows:

$$y_{P1} = a_0 + a_1 x + a_2 x^2 + a_3 x^3 + \dots + a_{20} x^{20} \quad (3.7)$$

$$y_{P2} = b_0 + b_1 x + b_2 x^2 + b_3 x^3 + \dots + b_{20} x^{20} \quad (3.8)$$

where the linear coefficients $a_0, a_1, a_2, a_3, \dots, a_{20}$ and $b_0, b_1, b_2, b_3, \dots, b_{20}$ are determined in a way to maximise the fit.

3.2.2 Secondary reflector design

For this section, a quarter of a circle was used, whose centre was set at (W_{abs}, W_{abs}) and radius W_{abs} . Eq. (3.9) expresses the calculation for the circular section obtained:

$$y = W_{abs} - \sqrt{W_{abs}^2 - (x - W_{abs})^2} \quad (3.9)$$

where the coordinate limits are $0 \leq x \leq W_{abs}$ and $0 \leq y \leq W_{abs}$. Figure 3.6 illustrates the circular shape drawing.

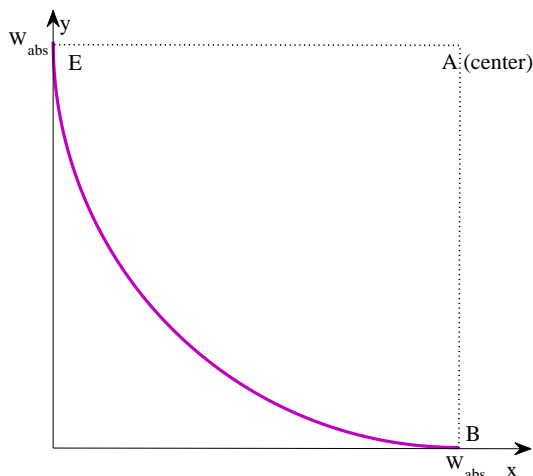


Figure 3.6: Circular reflector drawing with centre (W_{abs}, W_{abs}) and radius W_{abs} .

3.2.3 Tertiary reflector design

This section comprises two vertically straight reflector of height H_{TS} above the circular section and ends at the absorber surface (whose y -coordinate is y_{TS}). The coordinate limits here are $0 \leq x \leq W_{abs}$ and $W_{abs} \leq y \leq y_{TS}$.

After going through all the three sections that form the concentrator, Figure 3.7 illustrates all the reflectors arranged along with the main coordinates.

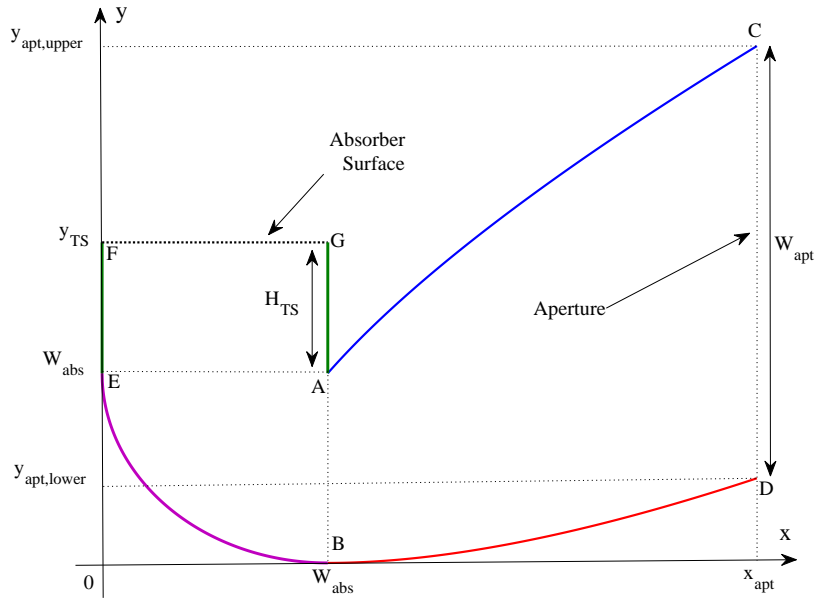


Figure 3.7: Concentrator's cross section view.

Additionally, Figure 3.8 shows the concentrator (with length L_{col}) in 3 dimensions, where the faces ACDBEFG and A'C'D'B'E'F'G' are the boundaries of the ends.

3.3 Ray Tracing and Optical Modelling

To assist the optical analysis, a 2D and a 3D ray tracing algorithms were implemented in Matlab® and used to simulate direct solar rays that come through the aperture, reflected at the reflectors before reaching the absorber. Figure 3.9 shows the concentrator's orientation in space (south facing) and one ray entering the aperture at its angular components (α_s, γ_s) for illustration purposes.

The following assumptions were used for the algorithm development:

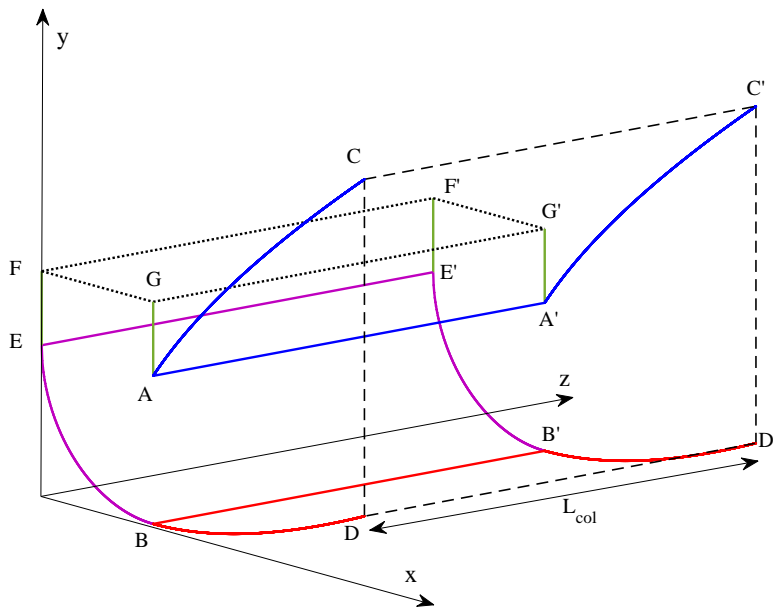


Figure 3.8: Final concentrator's design in 3D.

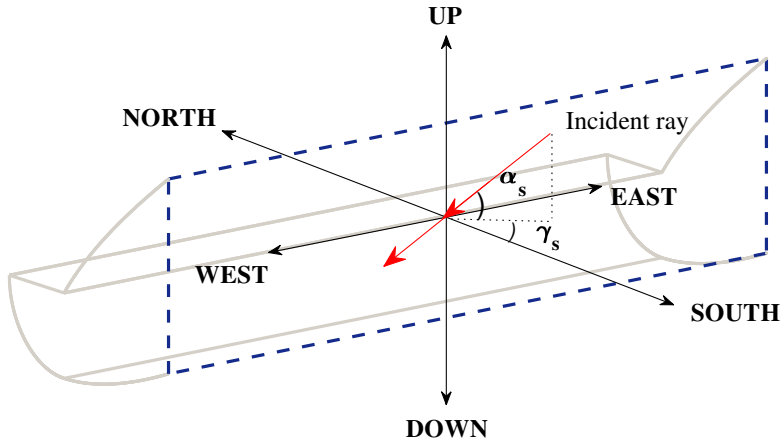


Figure 3.9: Concentrator's orientation in the space and one incoming ray going through the aperture.

- All reflectors are specular, i.e., the incident angle is equal to the reflected angle in relation to the normal at the intersection point;
- The reflector reflectance (ρ_{ref}) is 0.95 (95% of the rays energy is reflected at each reflection);
- The ends are assumed to be reflective and specular surfaces, where the reflectance



is also 0.95;

- 660 equally spaced solar rays (N_{rays}) initially placed at the aperture were used for the 2D model (2 rays/mm of aperture width) and 165,000 for the 3D model (2 rays/mm of aperture width and 5 rays/cm of aperture length). Each ray carries equal amounts of energy (e_i) regardless of the altitude and azimuth solar angles;
- A 4-mm thick low iron glass was employed with a refractive index of 1.526 and an extinction coefficient of 4 m^{-1} . The glazing transmittance (τ_{glaz}) was calculated by using equations described in Duffie and Beckman (2013). When the rays are perpendicular to the surface, the value of τ_{glaz} is approximately 0.90;
- The absorber absorptance is 0.85 (85% of the ray's energy reaching the absorber is absorbed);

It is important to remark three observations regarding both models:

1. In the 2D ray tracing modelling, the boundaries are the curves illustrated in Figure 3.7, where the rays go through the segment CD;
2. In the 3D ray tracing modelling, the boundaries are the surfaces and the concentrator's ends shown in Figure 3.8, where the rays go through the face CDC'D';
3. The 2D ray tracing is a particular case of the 3D one, but the azimuth angle is zero for all the simulations.

To help visualise the application of the ray tracing technique, Figures 3.10 and 3.11 show rays entering the concentrator and getting reflected until reaching the absorber, in 2D and 3D, respectively.

For the modelling, it is important to check whether the incoming rays are reaching the absorber. This can be done by defining the angular acceptance, which is the ratio of the number of accepted rays to the total number of rays at a particular altitude solar angle (α_s), according to Eq. (3.10).

$$\theta_{\text{acc}} = \frac{\sum_{i=1}^{N_{\text{rays}}} r_{\text{acc}}(i)}{N_{\text{rays}}} \quad (3.10)$$

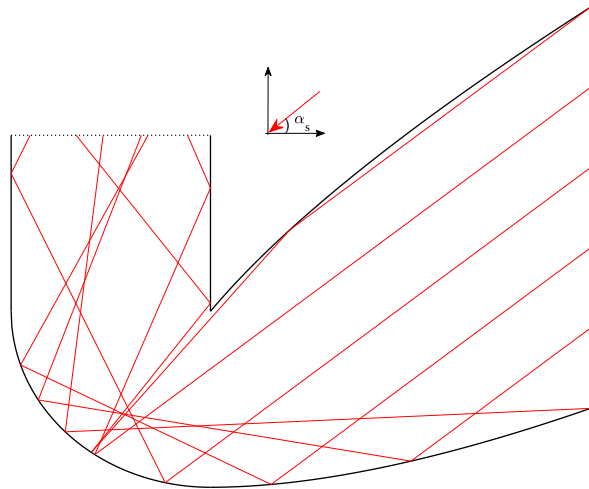


Figure 3.10: Visualisation in 2D of six rays coming through the aperture at an angle α_s .

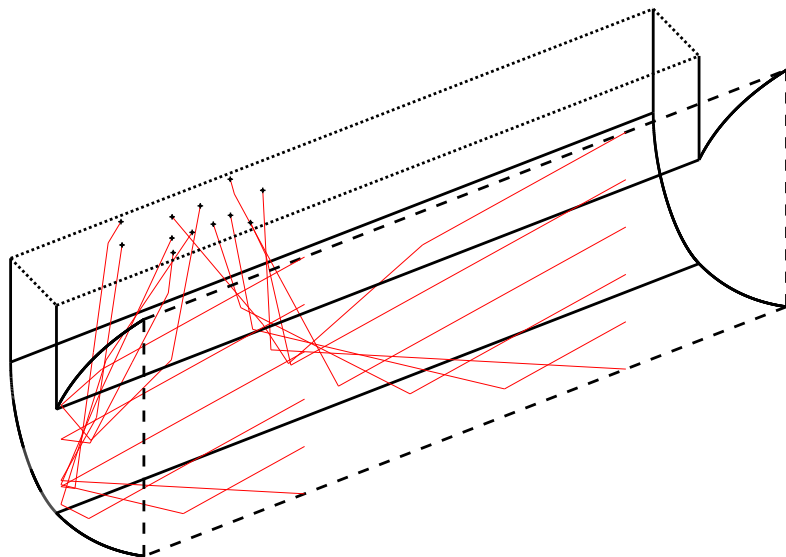


Figure 3.11: Visualisation in 3D of two sets of six rays coming through the aperture at a particular pair of angles α_s and γ_s .

where the ray acceptance $r_{\text{acc}}(i)$ for each ray i assumes only one of two possible values shown in Eq. (3.11):

$$r_{\text{acc}}(i) = \begin{cases} 1, & \text{if ray } i \text{ reaches the absorber} \\ 0, & \text{if ray } i \text{ does not reach the absorber} \end{cases} \quad (3.11)$$

The next step is to regard the reflective efficiency. This variable is defined as the

ratio between the energy reaching the absorber and the incoming energy, considering only the reflection losses. It is calculated by Eq. (3.12) and is a function of the system's shape and the concentration ratio (Sellami and Mallick, 2013):

$$\eta_R = \frac{\sum_{i=1}^{N_{\text{rays}}} e_i \rho^{r_i}}{\sum_{i=1}^{N_{\text{rays}}} e_i} \quad (3.12)$$

where r_i is the number of reflections of the solar ray i . It must be highlighted that each value of η_R is calculated for each pair of α_s and γ_s . Eq. 3.13 shows how to estimate the average reflective efficiency, which is the average of all η_R within the period of operation:

$$\bar{\eta}_R = \frac{\int_{n_1}^{n_2} \int_{\omega_{s1}}^{\omega_{s2}} \eta_R d\omega_s dn}{\int_{n_1}^{n_2} \int_{\omega_{s1}}^{\omega_{s2}} d\omega_s dn} \quad (3.13)$$

In an equivalent way, the average glazing transmittance as a function of β is calculated from different values of τ_{glaz} in Eq. (3.14).

$$\bar{\tau}_{\text{glaz}} = \frac{\int_{n_1}^{n_2} \int_{\omega_{s1}}^{\omega_{s2}} \tau_{\text{glaz}} d\omega_s dn}{\int_{n_1}^{n_2} \int_{\omega_{s1}}^{\omega_{s2}} d\omega_s dn} \quad (3.14)$$

where the transmittance τ_{glaz} depends on the incident angle θ_i , which is the angle between the incident solar ray and the normal to the glazing, is calculated by Eq. (3.15):

$$\theta_i = \cos^{-1} [\cos \alpha_s \cos(\gamma_s - \gamma_w) \sin \beta + \sin \alpha_s \cos \beta] \quad (3.15)$$

where $\gamma_s = 0$ in the 2D analysis, and the concentrator azimuth angle γ_w is zero as the system is south facing oriented.

Lastly, the optical efficiency η_o can be calculated by Eq. (3.16), which is the fraction of the incoming solar energy absorbed by the absorber.

$$\eta_o = \eta_R \tau_{\text{glaz}} \alpha_{\text{abs}} \quad (3.16)$$

Considering the operation period, Eq. (3.17) expresses the calculation of the average optical efficiency:

$$\bar{\eta}_o = \frac{\int_{n_1}^{n_2} \int_{\omega_{s1}}^{\omega_{s2}} \eta_o d\omega_s dn}{\int_{n_1}^{n_2} \int_{\omega_{s1}}^{\omega_{s2}} d\omega_s dn} \quad (3.17)$$

3.4 Results and Discussion

The modelling and the design defined can help in the investigation of the concentrator's shape and its optical efficiency profile. Hence, this section was divided into: the effect of the parabolic shape and the tertiary section on the efficiency, the evaluation of the length and its impact on the reflector cost and weight; and the effect of the glazing inclination on the light transmittance.

3.4.1 Effect of the parabolic shape and tertiary section

In the operation period, the limits of altitude solar angle calculated by Eq. (3.2) are:

- 60° as the upper limit, when the Sun is at its highest altitude, in the summer solstice (21/06) at solar noon;
- 17° as the lower limit, when the Sun is at its lowest altitude in the equinox (21/09) at 8 am (9 am in summertime).

Hence, the collector must accept direct solar radiation with altitude solar angles between 17° and 60° . Once the limits are set, an initial design of the collector was sketched of which the angles of the axes of both parabolic reflectors are coincident to those limits

so that all direct radiation between 17° and 60° is accepted. Using SolidWorks, the sketch of the initial design was performed (shown in Figure 3.12) and from this, the absorber width was found with the aim of achieving the maximum concentration ratio. Hence, the absorber width (W_{abs}) is 145 mm with the concentration ratio is 2.28.

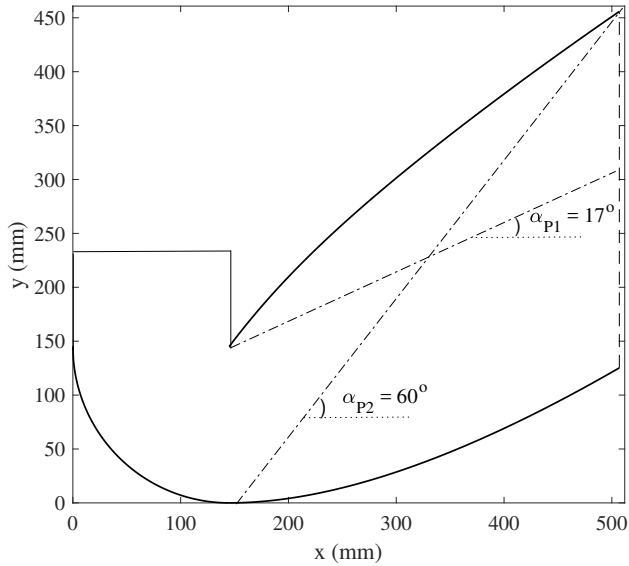


Figure 3.12: Concentrator's initial design.

As this concentrator is truncated, the range of angular acceptance may be broader than the limits previously defined. In order to check this hypothesis, a graph of θ_{acc} vs. α_s was plotted and shown in Figure 3.13.

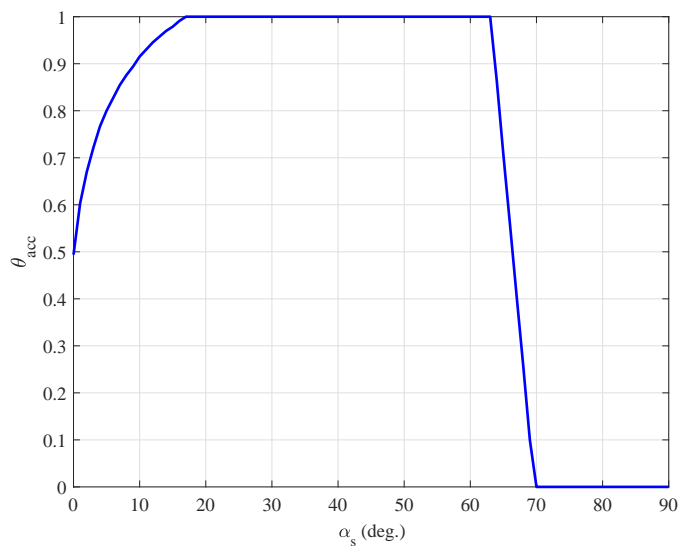


Figure 3.13: Angular acceptance vs. solar altitude angle for the initial design.

From Figure 3.13, the concentrator fully accepts direct radiation from 17° to 63° of α_s , which exceeds the range of the operation period. Therefore, the concentrator's optical performance can be enhanced by further modifications to the reflectors. In this particular case, it can be done by decreasing the lower parabola axis angle (α_{p2}). As this change in shape only affects the number of reflections, $\bar{\eta}_R$ was calculated at different values of α_{p2} and two graphs were plotted in Figure 3.14.

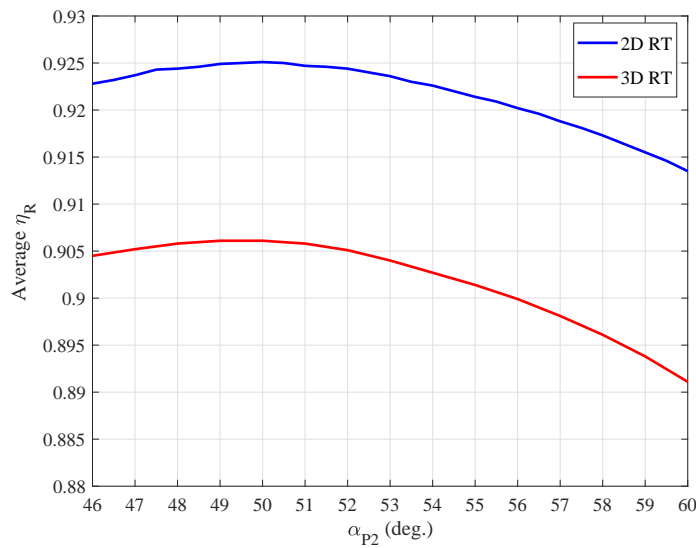


Figure 3.14: Average reflective efficiency *versus* lower parabola axis angle.

It can be seen in Figure 3.14 that the highest values of efficiency were achieved at $\alpha_{p2} = 50^\circ$, which is 0.9250 for the 2D model and 0.9060 for the 3D model. For both models, the reflective efficiency was increased by less than 2% compared to values obtained at $\alpha_{p2} = 60^\circ$. The difference between the two graphs is due to the higher number of reflections as the solar rays hit the ends of the concentrator. The variation of α_{p2} also influences the shape of the parabolic reflectors and, consequently changes the size of the solar collector at the primary section (as observed in Figure 3.15). As α_{p2} decreases, the full width of the collector is reduced and therefore the reduction of α_{p2} to 50° is positive in terms of optical efficiency and material cost savings.

To understand the effect of the tertiary section in the optical analysis, the average reflective efficiency calculated by Eq. (3.12) is shown in Figure 3.16 as function of the tertiary section height. For this analysis, α_{p2} was kept at 50° .

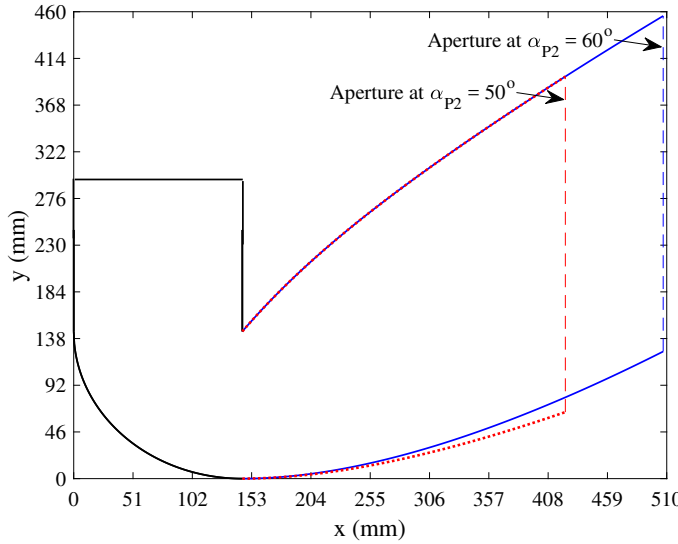


Figure 3.15: Comparison between concentrators at 60° of α_{P2} (blue) and at 50° of α_{P2} (red).

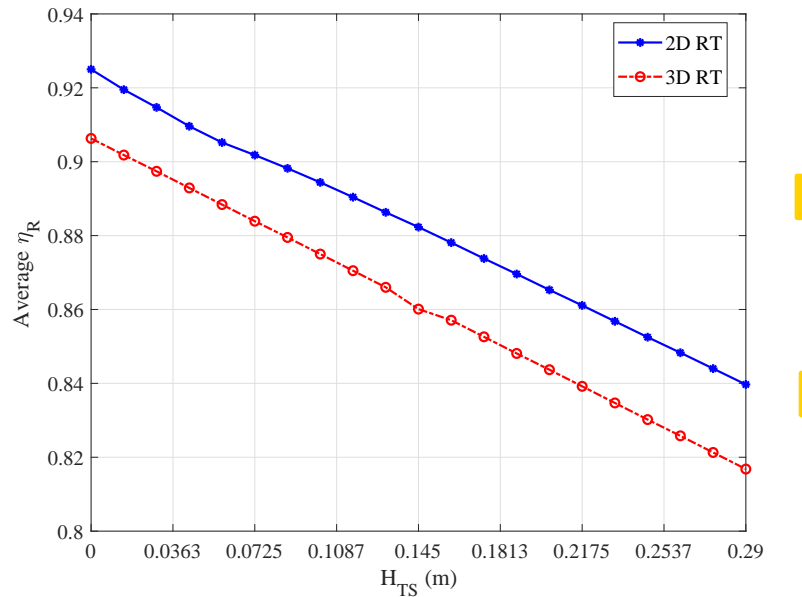


Figure 3.16: Average reflective efficiency *versus* tertiary section height for 2D and 3D models.

Both graphs of $\bar{\eta}_R$ have an approximate linear behaviour. The drop in efficiency as H_{TS} increases is due to the higher number of reflections. The difference between both graphs is approximately 2%, where the 3D model resulted in smaller values of $\bar{\eta}_R$ as the reflections at the ends are taken into account.

Although the optical efficiency is reduced by the increase of the tertiary section height, the cavity has a function of distributing the incoming energy uniformly along

the absorber surface. To apply this function, the results of the simulation α_s at 54° was selected and this can be seen in Figs. 3.17, 3.18 and 3.19.

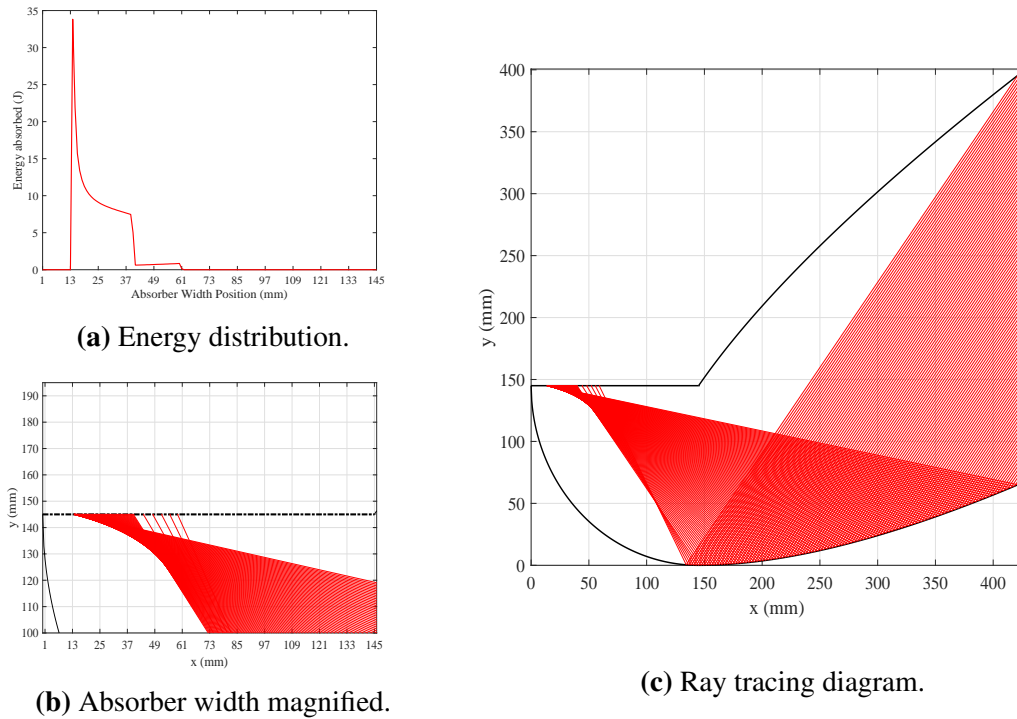


Figure 3.17: Ray tracing diagram in 2D and energy distribution over the absorber width with no tertiary section.

From Figure 3.17, a high energy peak concentrated in one millimetre of absorber width is observed and all the energy is concentrated in 45 millimetres. From Figs. 3.18 and 3.19, the energy is more distributed across the absorber surface. Hence, the tertiary section helps to distribute the solar energy more uniformly over the absorber area, which is desirable for further heat transfer even though the reflection losses are higher.

3.4.2 Evaluation of the length on the optical performance

For the length analysis, the average reflective efficiency η_{av} as calculated at different collector lengths and therefore Figure 3.20 shows the relationship between these two variables.

There is an increase in efficiency up to $L_{col} = 0.625$ m with only a slight increase above that, thus longer collectors are more efficient. This is due to a smaller number of reflections incident on the end plates, enhancing optical performance. This analysis is

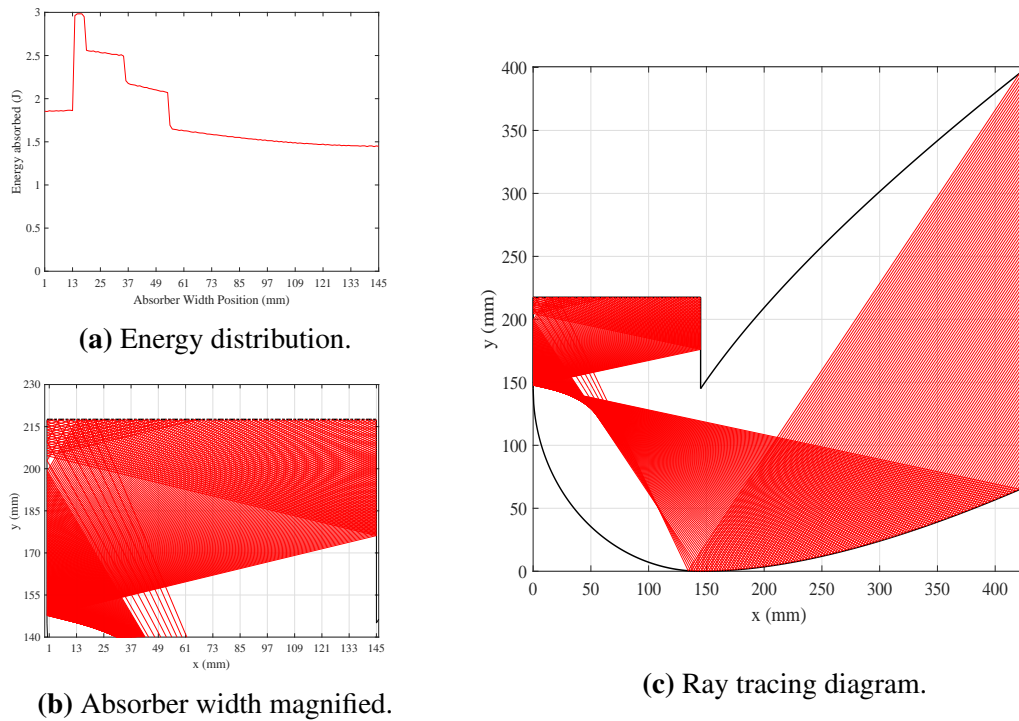


Figure 3.18: Ray tracing diagram in 2D and energy distribution over the absorber width at 72.5 mm of tertiary section.

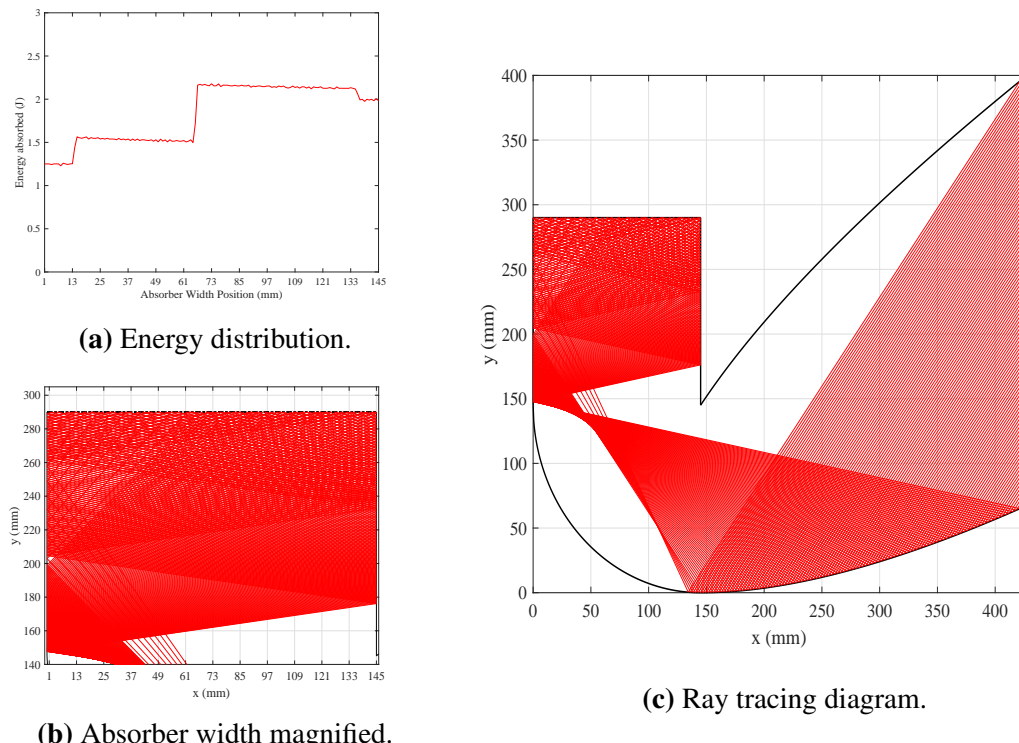


Figure 3.19: Ray tracing diagram in 2D and energy distribution over the absorber width at 145 mm of tertiary section.

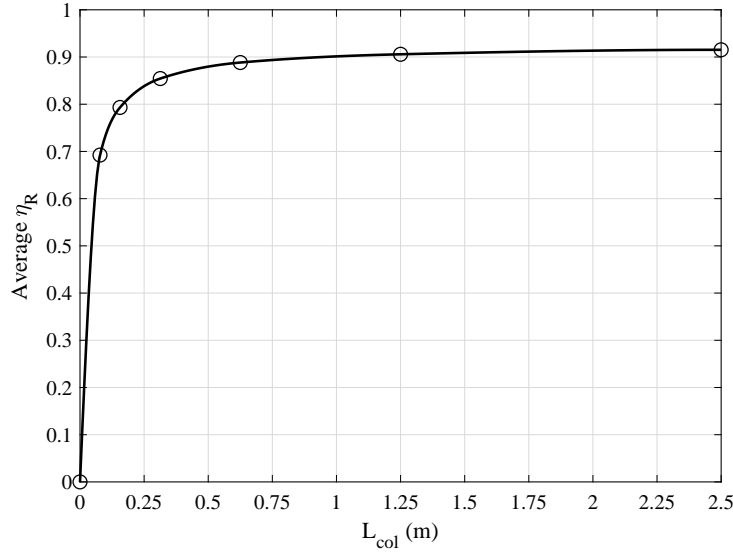


Figure 3.20: Average reflective efficiency vs. L_{col} .

important to decide how long a collector must be considering the amount of material for its fabrication. From the design, the reflector weight and cost were calculated as function of L_{col} and shown in Figure 3.21. It is important to remark that the end plates are included, and the cost was calculated based on 50 euro per m^2 of reflector sheet.

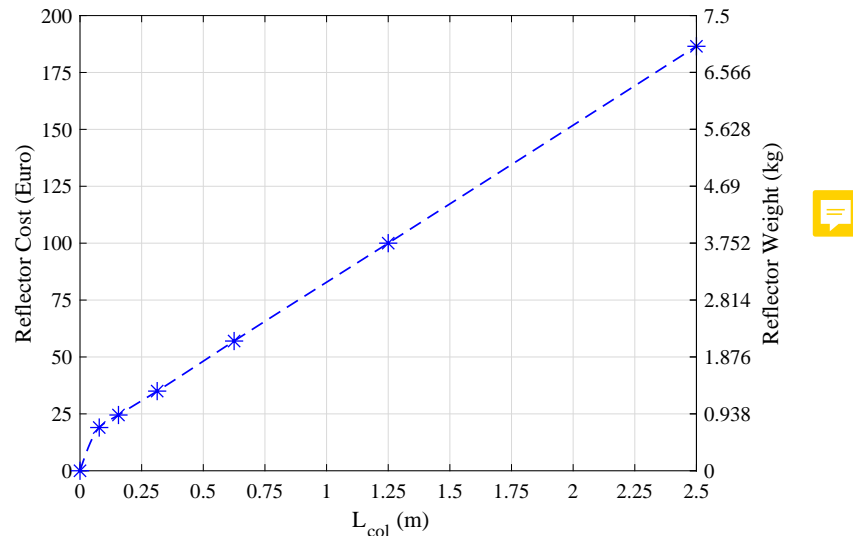


Figure 3.21: Cost and weight of reflector as function of the collector length.

The reflective efficiency at $L_{\text{col}} = 0.625 \text{ m}$ is 0.890 whereas the same efficiency at 1.25 m in length is 0.905. It is a gain in efficiency of 1.5%, but at the cost of 76% more material for the collector fabrication. The manufacturer may opt to fabricate two 0.625-m

long collectors instead of one with 1.25 m in length.

3.4.3 Effect of the glazing inclination on the light transmittance

In order to begin analysing the effect of the glazing inclination over the average glazing transmittance, it is important to understand how τ_{glaz} varies in relation to the incident angle θ_i . Such variation is represented by the graph shown in Figure 3.22.

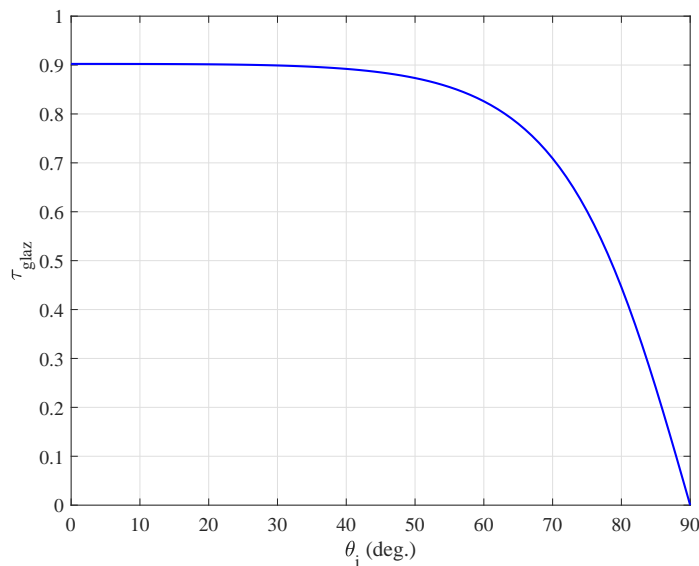


Figure 3.22: Average transmittance versus glazing inclination.

From the values of transmittance previously obtained, Eq. (3.14) was used and the results are shown in Figure 3.23.

From this result, it is possible to observe a maximum average transmittance at $\beta = 47^\circ$ for the 2D model and at $\beta = 33^\circ$ for the 3D model, whose values are 0.9022 and 0.8907, respectively. It is the glazing inclination of which the glazing losses are minimum overall. Compared to the transmittance with the glazing placed vertically, there is a gain of 2.5% in optical efficiency for the 2D model and 14% in the 3D model. The difference between the two models is due to the higher incident angles of the direct rays coming through the glazing when the azimuth solar angle is included in the modelling.

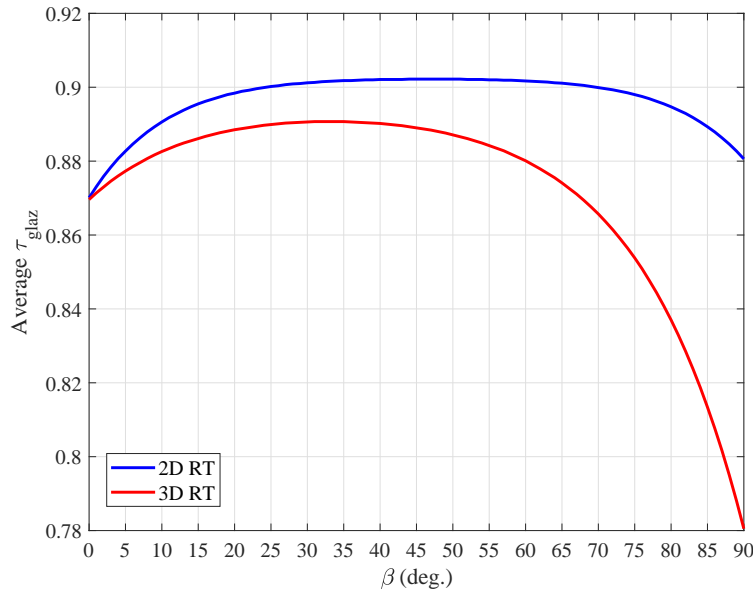


Figure 3.23: Average transmittance versus glazing inclination.

3.5 Chapter Summary

After the optical analysis, the concentrator's design has been defined as shown in Figure 3.24 and the main geometric parameters are summarised in Table 3.2. The glazing inclination has been set at $\beta = 62^\circ$ due to practical reasons related to its width.

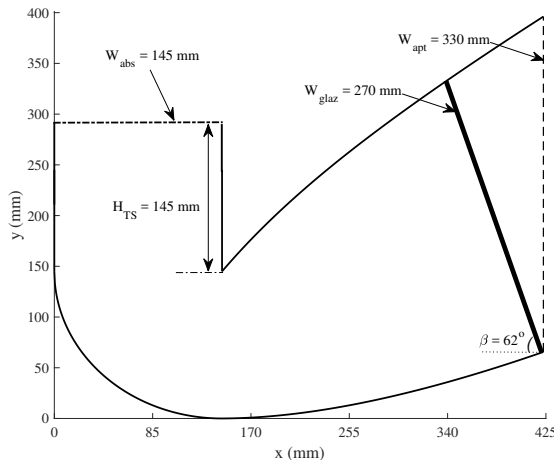


Figure 3.24: Cross section of the concentrator's final design.

The selection of an air heater concentrator with the absorber horizontally facing downwards aims to concentrate solar thermal energy inside the cavity and suppress heat losses. With the assistance of a ray tracing technique in 2D and 3D, an optical analysis

Table 3.2: Geometric parameters of the concentrator to be fabricated.

Symbol	Geometric parameter	Value
L_{col}	Concentrator length	1.25 m
H_{col}	Concentrator height	0.40 m
W_{col}	Concentrator width	0.43 m
W_{abs}	Absorber width	0.145 m
A_{abs}	Absorber area	0.18 m ²
W_{glaz}	Glazing width	0.27 m
A_{glaz}	Glazing area	0.34 m ²
β	Glazing inclination	62°
W_{apt}	Aperture width	0.33 m
A_{apt}	Aperture area	0.41 m ²
H_{TS}	Tertiary section height	0.145 m
CR	Concentration ratio	2.28

has been undertaken to evaluate its reflective efficiency, glazing transmittance and tertiary section. The results show that there is a maximum value of reflective efficiency for a particular parabolic reflector shape for both models and a maximum value of glazing transmittance for each model at different inclinations. It was also concluded that the energy distributed along the absorber area is more uniform with a tertiary section rather than without it even though the optical losses are higher. The effect of the tertiary section on the concentrator's performance needs to be further assessed, via thermal modelling and outdoor experiments.

CHAPTER 4

EXPERIMENTAL PERFORMANCE ANALYSIS

The aim of this chapter is to analyse the outdoor experimental performance of the solar air heater prototype fabricated using the concentrator designed in Chapter 3. This air heating system was fabricated and tested at Technological University Dublin, Ireland. The specific objectives are to:

- Present the materials and components for fabrication;
- Describe the data collection procedure and equipment used;
- Evaluate the thermal performance of the system in open loop configuration.

4.1 Materials for the prototype

4.1.1 Absorber surface selection

The function of the absorber surface in solar thermal systems is to retain thermal energy from incoming solar radiation. To do so, carbon fibre weave was selected as the solar absorber material for this prototype. Although such material is not conventionally used in solar air heating systems (Shams, 2013), its use reduces the system's weight: compared to an aluminium plate of same dimensions, the carbon fibre surface is 40% lighter (Clearwater Composites, 2016).

Carbon fibre weave's physical properties are presented in Table 4.1. Absorptivity,

thermal conductivity and specific heat were measured and reported by Wu et al. (2012) and Joven (2012).

Table 4.1: Carbon fibre weaver properties.

Property	Value
Thickness	0.26 mm (measured)
Density	1600 kg/m ³
Thermal Conductivity	1 W/m.K
Specific Heat	1000 J/kg.K
Absorptivity	0.85

Moreover, the material is already perforated and this porosity was calculated from data of morphology image (Figure 4.1) by Shams (2013). The average values of perforation area and porosity are 0.147 mm² and 4.2%, respectively. These values were used as parameters in the thermal modelling further depicted in Chapter 5.

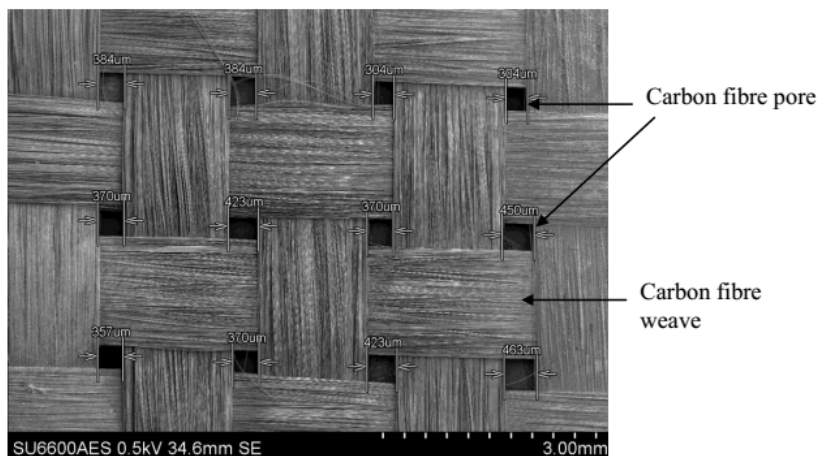


Figure 4.1: Morphology image of carbonfibre sample taken at magnification of 15x.

However, it is difficult to integrate the carbon fibre fabric without a proper frame and resin. Epoxy laminating resin was applied at the corners of the absorber surface to avoid any splitting in the weave and to keep the surface stretched. These corners were attached to a thin wooden frame of specific absorber dimensions (0.145 m x 1.25 m).

4.1.2 Glazing Cover selection

The glazing material for the system is a 4-mm thick tempered clear glass cover. This tempered property enables the glass to provide a safer and more endurable product

than ordinary glasses. It withstands 5 times more impact before shattering. If shattered, the fragments pose a reduced danger to the user, making it an ideal product for use in both commercial and domestic applications (First Glass, 2016). The glazing surface protects the reflector and absorber surfaces from weather conditions and reduces thermal losses from the interior of the concentrator. However, the solar radiation that is effectively transmitted to the air heating system is reduced due to absorption and reflection at the glazing cover. The glazing properties, such as absorptivity and transmittance, are shown in Table 4.2. From the concentrator's design, the glazing dimensions are 0.27 m x 1.25 m.

Table 4.2: Glazing cover properties.

Property	Value
Thickness	4 mm
Density	2500 kg/m ³
Absorptivity ¹	0.02
Transmittivity ¹	0.90 
Specific Heat	880 J/kg.K

4.1.3 Reflector sheet selection

The reflective material employed is called *MiroSun* from the German company Alanod, its only product used for solar applications. This reflective aluminium sheet is manufactured using continuous physical vapour deposition (PVD) process applied for a super reflective layer to coil anodized material and afterwards the surface is protected by a nano-composite in a coil-coating process. Table 4.3 shows optical and physical properties of this material. From the concentrator's design, the total area of reflector sheet used was 1.25 m x 1.20 m.

4.1.4 Prototype's structure

The materials used to fabricate the prototype's structure are listed as follows:

- 0.7 m² of a 2-mm thick aluminium sheet to form the ends;

¹Values at near normal incident light

Table 4.3: *MiroSun* reflector properties (Alanod, 2016).

Property	Value
Front Side Layer	PVD improved
Reverse Side Layer	Anodised
Thickness	0.5 mm
Density	2700 kg/m ³
Total Reflectivity	0.95

- 8 aluminium bars of 1.25 m in length to support and keep the reflectors in the desired position;
- 0.45 m² of 1-cm thick timber to form a cavity above the absorber surface in order to reduce heat losses; 
- two 2.5-in diameter aluminium pipe of 10 cm in length for the airflow inlet and outlet;
- 1.8 m² of a 0.6-mm thick aluminium sheet to box the whole structure.

Figure 4.2 shows photographs of the structure assembled. The space between the reflectors and the outer aluminium sheet was filled by fibre glass wool to prevent the system from losing heat. Afterwards the structure was wrapped with 6-cm thick polyurethane foam board. 

4.2 Instrumentation and experimental unit

Temperatures were measured at the inlet and outlet of air, absorber and glazing surfaces using type T (Cu-CuNi) PTFE insulated twist fine wire thermocouple sensor with accuracy of 0.5 °C. Figures 4.3 and 4.4 indicate the position of each thermocouples on the absorber and glazing surfaces, respectively. 18 thermocouples were used in total. As a matter of orientation, in both figures the side where the thermocouple 1 is placed is the closest to the outlet. 

These measurements were recorded at 1 minute intervals with a DL2e data logger connected directly to a computer where the temperature data were downloaded via USB port (Datalogic, 2018). All thermocouples were labelled, inserted in a plug and connected to the data logger.

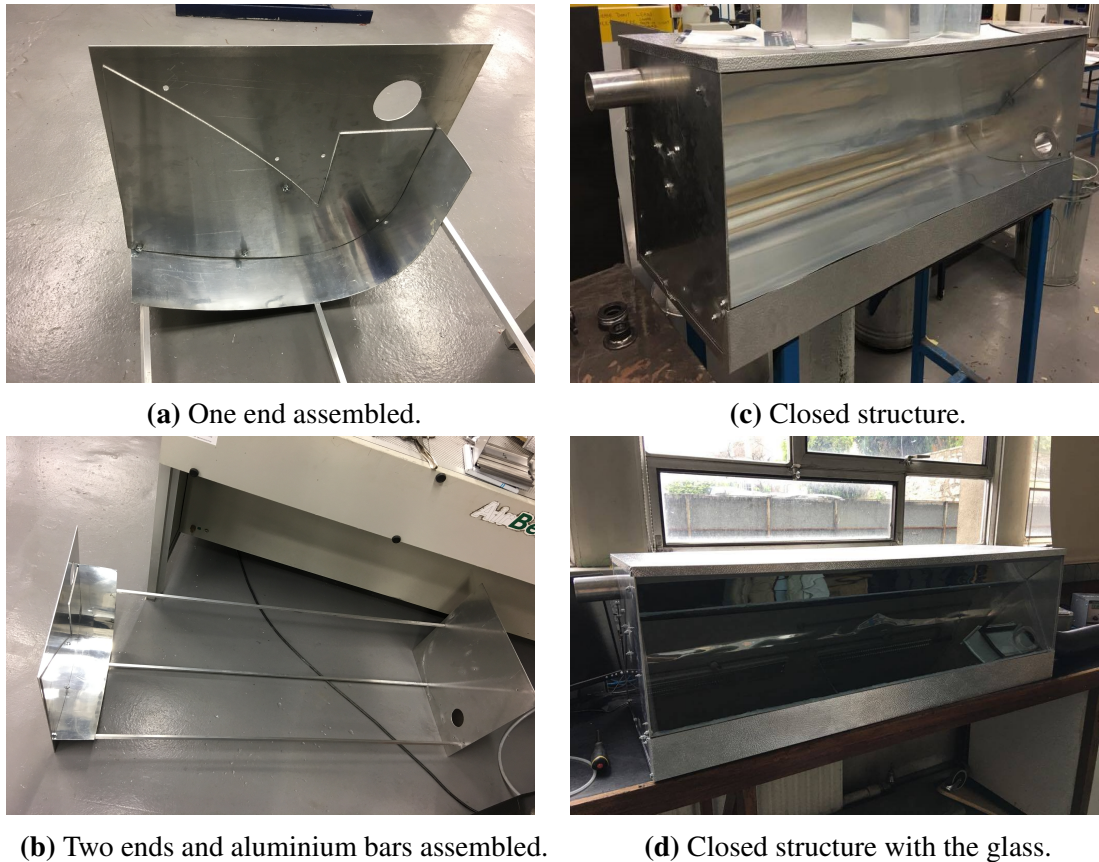


Figure 4.2: Parts of the prototype's structure and assembled

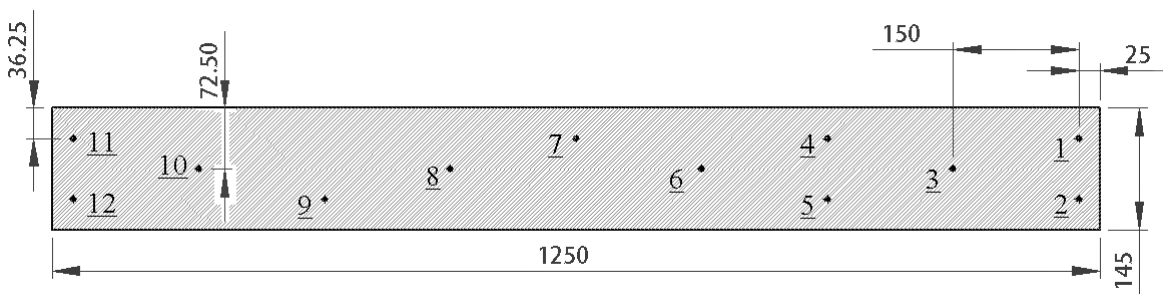


Figure 4.3: Positions of the 12 thermocouples placed on the absorber surface (dimensions in mm).

The airflow was blown by a 12-W fan, where the rate was varied by a voltage adaptor with five different voltage inputs. The airflow rate was calculated by measuring the air velocity at the air outlet (v_{out}) using a Testo 425 hot wire anemometer and expressed by Eq. (4.1).

$$G_{air} = \frac{v_{out} A_{out} d_{air}}{A_{abs}} \quad (4.1)$$

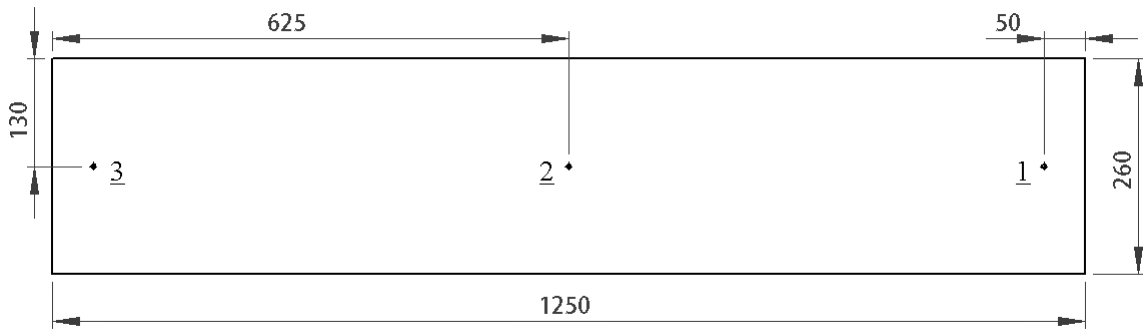


Figure 4.4: Position of the three thermocouples placed on the glazing surface (dimensions in mm).

where A_{out} is the cross section area of the outlet pipe and A_{abs} is the absorber area.

Table 4.4 shows those values of airflow rate as function of the voltage input (V_a) in terms of mass per absorber area (G_{air}), volume and a code corresponding to each level.

Table 4.4: Mass and volumetric flow rates calculated at each voltage input.

Voltage (V)	G_{air} (kg/s/m ² abs.)	Vol. flow rate (L/min)	Code
4.92	0.040	350	Low
5.82	0.055	500	Low-med
7.20	0.070	650	Medium
8.70	0.090	820	Med-high
11.30	0.115	1050	High

Hence, a 2nd degree polynomial was fit from the previous data, as shown in Eq. (4.2):

$$G_{air} = -6.3 \cdot 10^{-4} V_a^2 + 0.022 V_a - 0.054 \quad (4.2)$$

Next, a schematic diagram of the open loop experimental system is shown in Figure 4.5. A flexible duct was connected to the inlet of prototype. Air flowed through the air duct to the collector by the fan. The power supply unit provided voltage to the fan and energy to the data logger.

Figure 4.6 presents the prototype's front view. It was fixed to the ground to prevent it from moving due to severe wind conditions. The fan was enclosed and protected from the

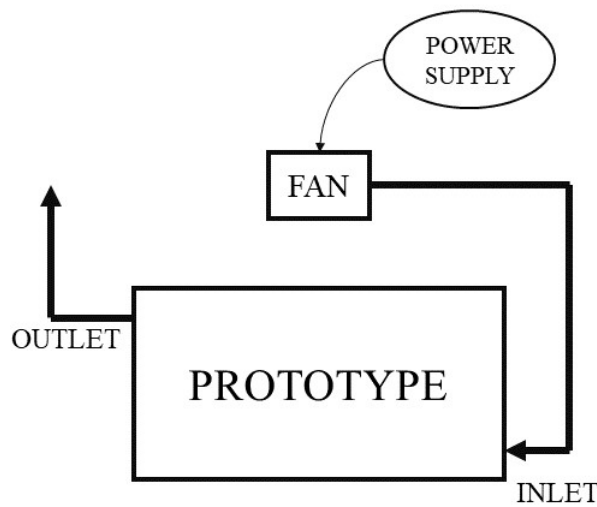


Figure 4.5: Schematic diagram of the experimental unit.

environment during the experiments and the data logger was placed behind the prototype.

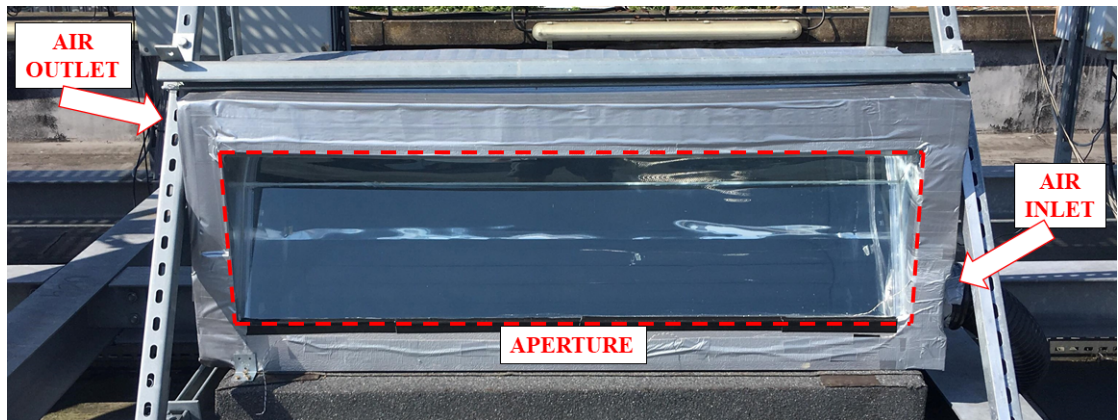


Figure 4.6: Open loop outdoor experimental unit.

4.3 Experimental results from the air heating prototype

This section approaches the experimental results from tests conducted at the five airflow rates and also the ones with no flow. The thermal performance of the prototype focused on evaluating the useful energy rate (or energy delivered), collector thermal efficiency and outlet air temperature. The useful heat rate transferred to the airflow is estimated by Eq. (4.3) (Kalogirou, 2004) using temperature measurements from the inlet and outlet:

$$Q_u = G_{air} A_{abs} C_{p,air} (T_{out} - T_{in}) \quad (4.3)$$

The thermal efficiency, which is the ratio of useful heat rate to the incoming total solar radiation on the aperture, is calculated by Eq. (4.4). Such efficiency can be evaluated either instantaneously or as an average over a certain period of time (Goswami, 2015):

$$\eta_{\text{th}} = \frac{Q_u}{I_t A_{\text{apt}}} \quad (4.4)$$

where I_t is the total incoming solar radiation. The solar data used in the calculations were downloaded from the Met Eireann website (MetEireann, 2018). Such data were measured by a solar pyranometer placed at the horizontal.

4.3.1 Experimental results at transient state

This topic presents the experimental results of measured temperatures and solar radiation, and calculation of energies and thermal efficiency on hourly basis. One day of each level of airflow rate was taken for data treatment and discussion, from 9:00 to 17:00.

Experimental results at zero airflow

The equilibrium temperature that the absorber approaches when no energy is removed from the collector is called stagnation temperature (Rabl, 1985). In order to verify this condition, the inlet and outlet of the system were closed and two tests at clear sky days were performed on 2nd and 3rd July as shown in Figure 4.7. The maximum stagnation absorber temperature reached 77 °C in both tests at an average I_t of 820 W/m² and T_{amb} of 22 °C.

Experimental results at low airflow rate

Figure 4.8 shows the results for the low airflow rate (0.04 kg/m².s) test on 9th June, in clear sky condition. The highest T_{out} was found to be 52 °C when T_{in} was 25 °C and T_{amb} was 22 °C. Therefore the maximum airflow temperature rise was 25 °C and observed at the region of solar noon (13h – 14h). The thermal efficiency (η_{th}) on this same region was averaged at 53%.

The graphs of hourly performance results is shown in Figure 4.9. The total incident

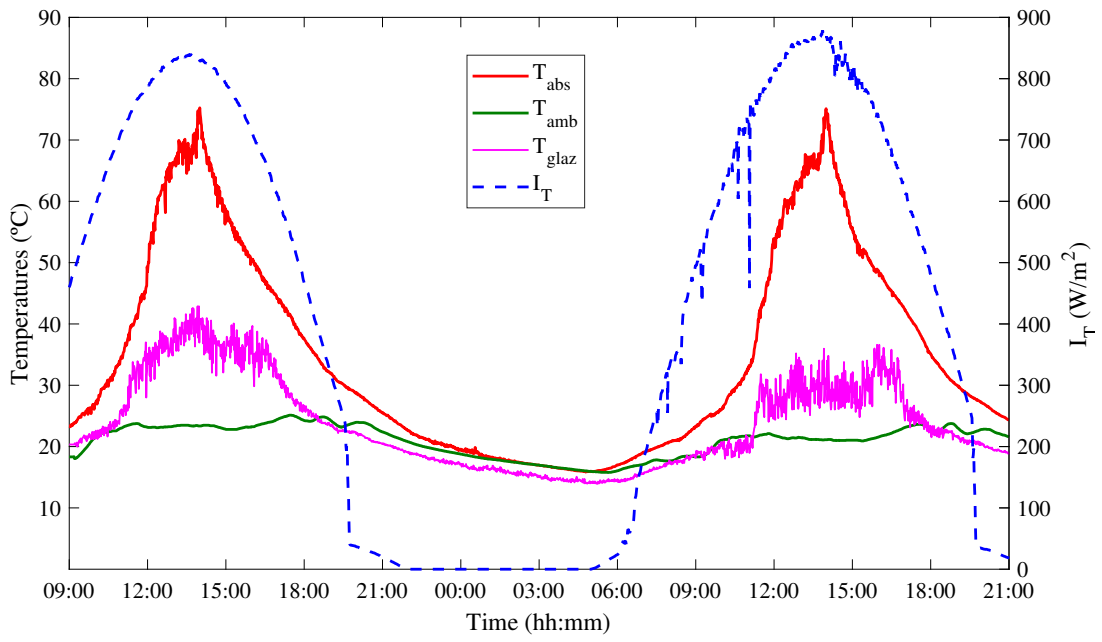


Figure 4.7: Experimental results from 2nd and 3rd July at zero airflow.

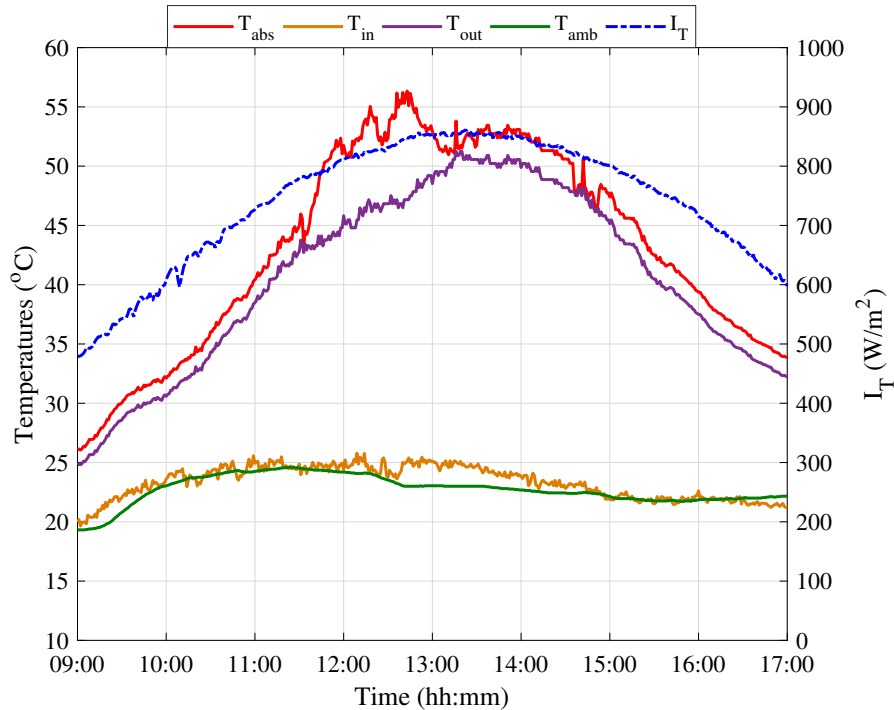


Figure 4.8: Experimental results from 9th June at 0.040 kg/m².s.

solar energy available on this clear sky day from 9 am to 5 pm was 20.46 MJ/m² of aperture; the total useful energy collected was 7.64 MJ/m² of aperture; and the average thermal efficiency obtained for the whole day was 35%. In the hour of highest solar radiation, the airflow collected 1.6 MJ/m² of energy at an average T_{out} of 50 °C.

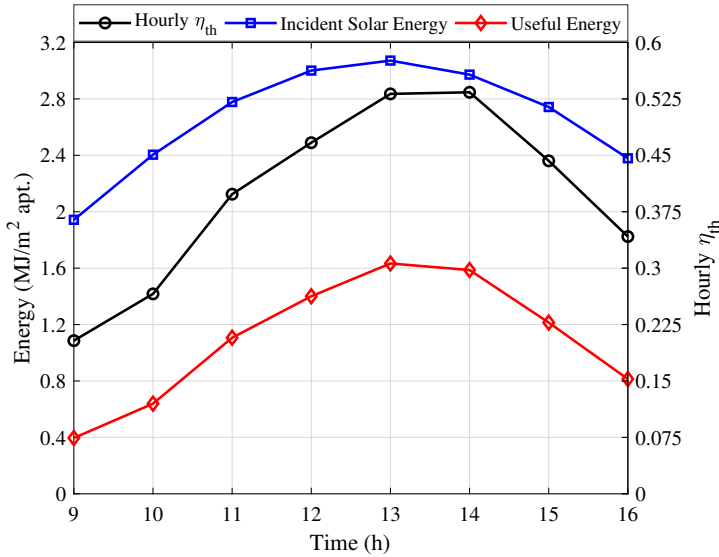


Figure 4.9: Hourly performance from 9th June at 0.040 kg/m².s.

Experimental results at low-med airflow rate

The experimental results of this test operating at low-med airflow (0.055 kg/m².s) are shown in Figure 4.10 under relatively clear sky condition. The highest T_{out} measured was 43 °C when $T_{in} = 23$ °C and $T_{amb} = 21$ °C. The maximum airflow temperature rise was 20 °C observed between 13:00 and 14:00. The thermal efficiency (η_{th}) on this same region was 55%.

The hourly performance is shown in Figure 4.11. The total solar energy available on 22nd June was 21.29 MJ/m²; the total useful energy collected was 9.56 MJ/m²; and the thermal efficiency for this day obtained was 43%. In the hour of solar noon (13h – 14h), the airflow collected 1.7 MJ/m² of energy at an average T_{out} of 43 °C.

Experimental results at medium airflow rate

The experimental results of the test operating at medium airflow (0.07 kg/m².s) is shown in Figure 4.12 on 29th May, in relatively clear sky condition. The highest T_{out} was measured to be 40 °C when T_{in} was 25 °C and T_{amb} was 20 °C. The maximum airflow temperature rise was 15 °C observed between 13h and 14h. The thermal efficiency (η_{th}) on this same region was 58%.

The hourly performance is shown in Figure 4.13. The total incident solar energy

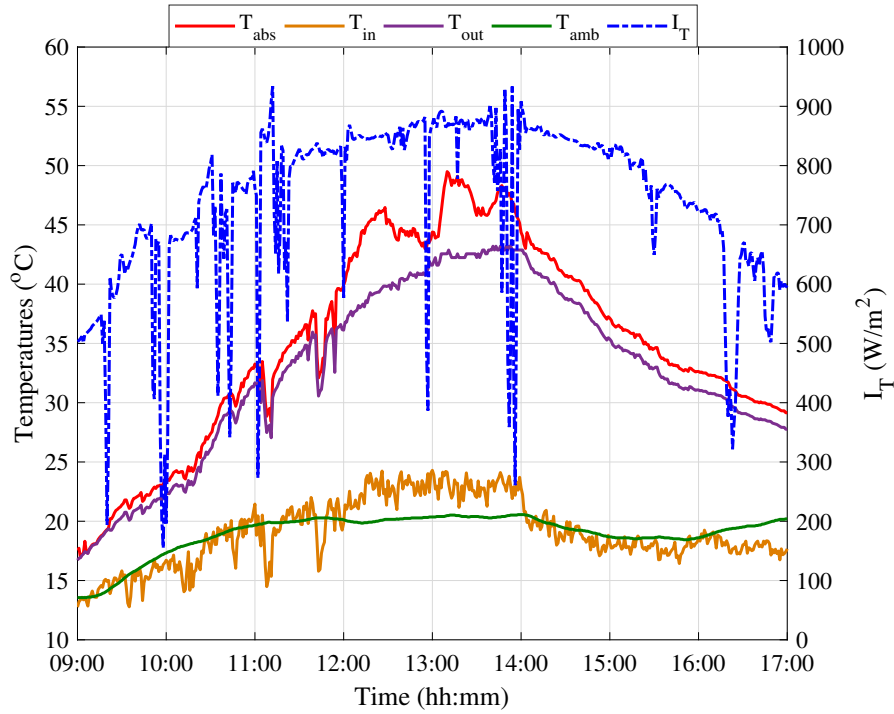


Figure 4.10: Experimental results from 22nd June at 0.055 kg/m².s.

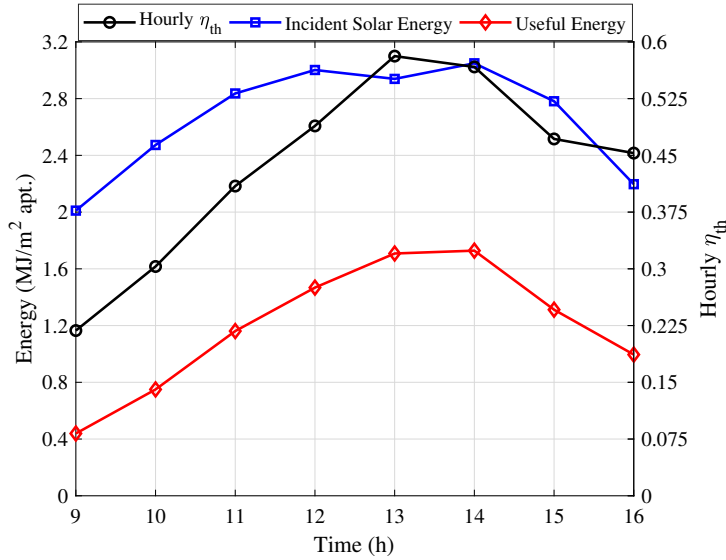


Figure 4.11: Hourly performance from 22nd June at 0.055 kg/m².s.

available on this day was 21.4 MJ/m²; the total useful energy collected was 10.03 MJ/m²; and the average thermal efficiency obtained was 46%. In the hour of highest solar radiation, the airflow collected 1.7 MJ/m² of energy at an average T_{out} of 40 °C.

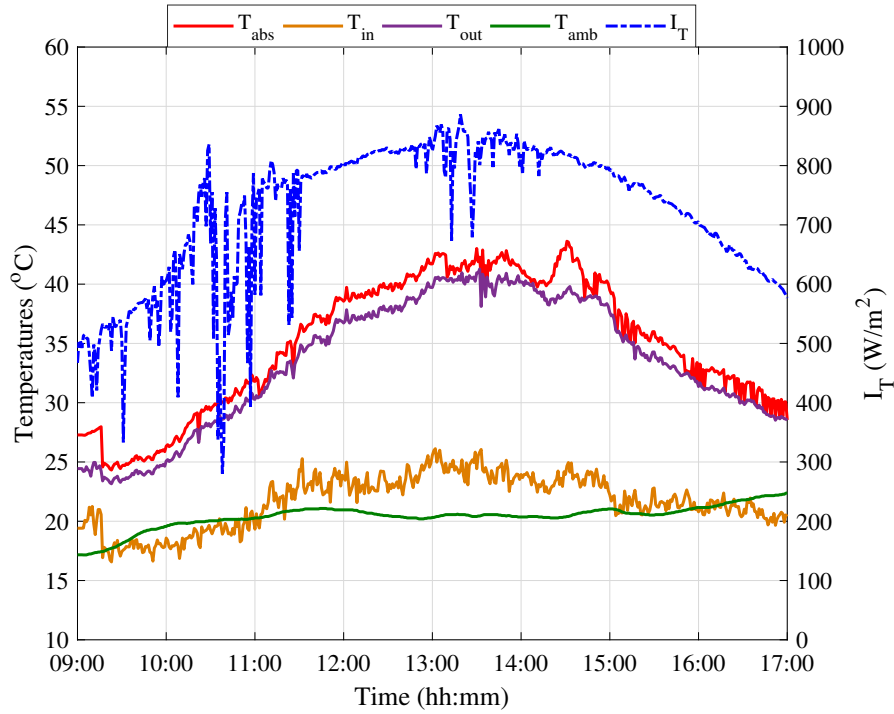


Figure 4.12: Experimental results from 29th May at 0.070 kg/m².s.

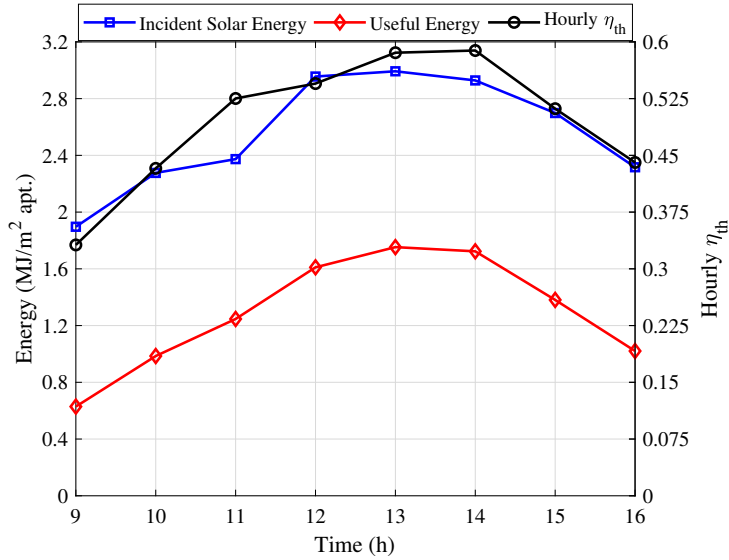


Figure 4.13: Hourly performance from 29th May at 0.070 kg/m².s.

Experimental results at med-high airflow rate

The results of the test at med-high airflow (0.09 kg/m².s) is shown in Figure 4.14 on 31st May. Although the solar data is very transient on this day, T_{out} kept constant around 39 °C when T_{in} was 27 °C and T_{amb} was 23 °C from 13:00 to 14:00. The maximum airflow temperature rise was 13 °C observed at solar noon. The thermal efficiency on this

same region was 59%.

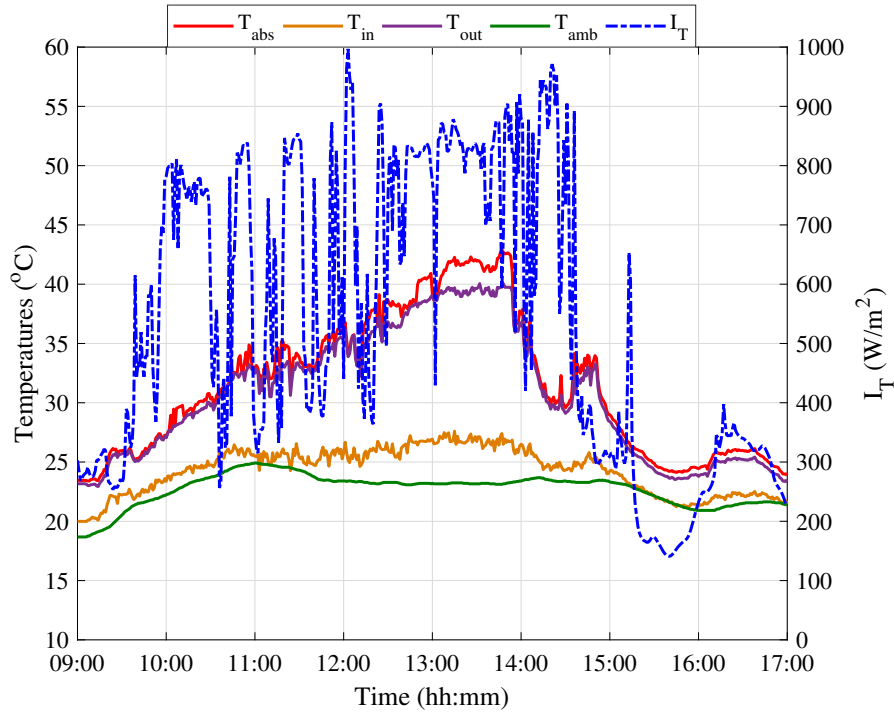


Figure 4.14: Experimental results from 31st May at $0.090 \text{ kg/m}^2 \cdot \text{s}$.

The hourly performance is shown in Figure 4.15. The total solar energy available was 15.6 MJ/m^2 ; the total useful energy collected was 7.18 MJ/m^2 ; and the average thermal efficiency obtained was 46%. In the hour of highest solar radiation, the airflow collected 1.6 MJ/m^2 of energy at an average T_{out} of 39°C .

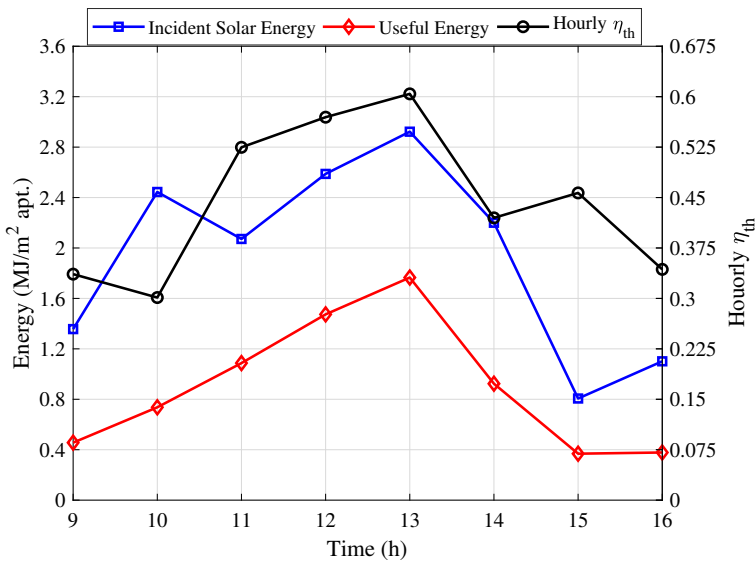


Figure 4.15: Hourly performance from 31st May at $0.090 \text{ kg/m}^2 \cdot \text{s}$.

Experimental results at high airflow rate

The experimental results of the test operating at high airflow rate ($0.115 \text{ kg/m}^2\cdot\text{s}$) is shown in Figure 4.16. The highest T_{out} was 40°C when T_{in} was 30°C and T_{amb} was 26°C . The maximum airflow temperature rise was 10°C and the maximum η_{th} observed was 60%.

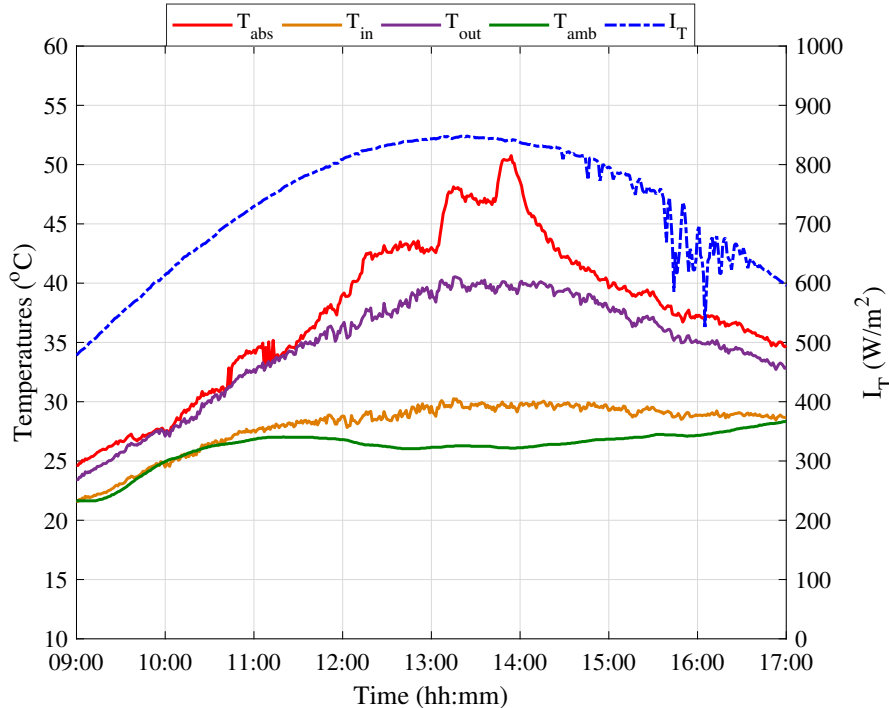


Figure 4.16: Experimental results from 28th June at $0.115 \text{ kg/m}^2\cdot\text{s}$.

The hourly performance is shown in Figure 4.17. The total incident solar energy available was 21.07 MJ/m^2 ; the total useful energy collected was 9.80 MJ/m^2 ; and the overall thermal efficiency obtained was 47%. In the hour of highest solar radiation, this airflow collected 1.8 MJ/m^2 of energy at an average T_{out} of 40°C .

4.3.2 Experimental results at nearly steady state

The thermal characterisation of a solar air heating system can be done by evaluating the thermal efficiency under steady state according to the Hottel-Whillier-Bliss equation,

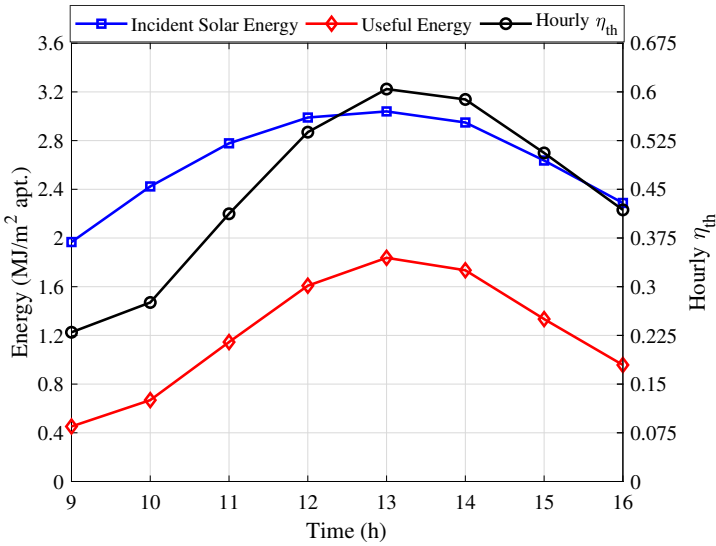


Figure 4.17: Hourly performance from 28th June at 0.115 kg/m².s.

expressed by Eq. (4.5).

$$\eta_{\text{th}} = F_R \eta_0 - F_R U_L \frac{(T_{\text{out}} - T_{\text{amb}})}{I_T} \quad (4.5)$$

where U_L is the system's overall heat loss coefficient and F_R is the heat removal factor. From this equation, η_{th} can be plotted against $(T_{\text{out}} - T_{\text{amb}})/I_T$, resulting in a linear curve, with $F_R \eta_0$ and $-F_R U_L$ as the linear coefficient and the slope, respectively (Goswami, 2015).

The experimental data collected for this analysis were during 10 minutes of tests around the solar noon period of clear days (nearly steady state condition), including all the five airflow rates. This is the period where the direct radiation range is at maximum, which was 800 – 900 W/m². To minimise the effects of the system's heat capacity, the data were taken in nearly symmetrical pairs, one before and one after noon, thus resulting in five averaged pairs for each day of experimental tests (Duffie and Beckman, 2013). Thermal efficiency was calculated by Eq. (4.4). With all the data collected, the thermal efficiency curve was plotted in Figure 4.18.

From these results, the parameters of Eq. (4.5) were calculated: $F_R \eta_0$ and $F_R U_L$ are 0.65 and -3.39 respectively, and the coefficient of correlation is 0.8. It is important to state that U_L is assumed to be weakly dependent on the absorber temperature in this operational range, where $(T_{\text{out}} - T_{\text{amb}})/I_T$ is between 0.015 and 0.07 m².°C/W, so that

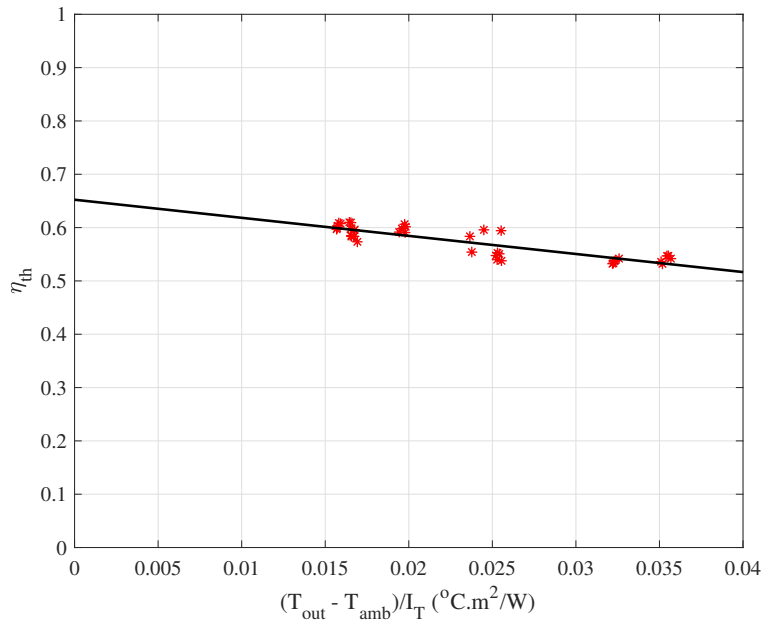


Figure 4.18: Thermal efficiency curve.

the heat loss coefficient is constant (Rabl, 1985). Comparing to other work, Shams et al. (2016) characterised experimentally a solar air heating system with a similar geometry. For this, they calculated the instantaneous thermal efficiency when the solar radiation varied between 937.6 and 1,085.4 W/m². This resulted in a linear coefficient ($F_R\eta_0$) of 0.73 and slope ($F_R U_L$) of -3.25 W/m².°C.

Next, Figure 4.19 shows thermal efficiency and outlet air temperature as functions of the mass airflow rate. From the thermal efficiency graph, it is possible to view a smooth increase in η_{th} when G_{air} becomes higher. The opposite behaviour is observed in the airflow temperature rise ($T_{out} - T_{in}$), where this variable drops dramatically when G_{air} varies from 0.04 to 0.09 kg/m².s and then falls smoothly by 2 °C.



4.4 Chapter summary

The fabrication of a solar air heating prototype for outdoor experimental tests has been detailed in this chapter. This chapter outlined the selection of materials, fabrication process of the system and the data collection apparatus. Carbon fibre weave with 85% in absorptivity was selected as the absorber material for the collector considering its properties of the material and the inherent perforation. High reflectance (95% reflectivity)

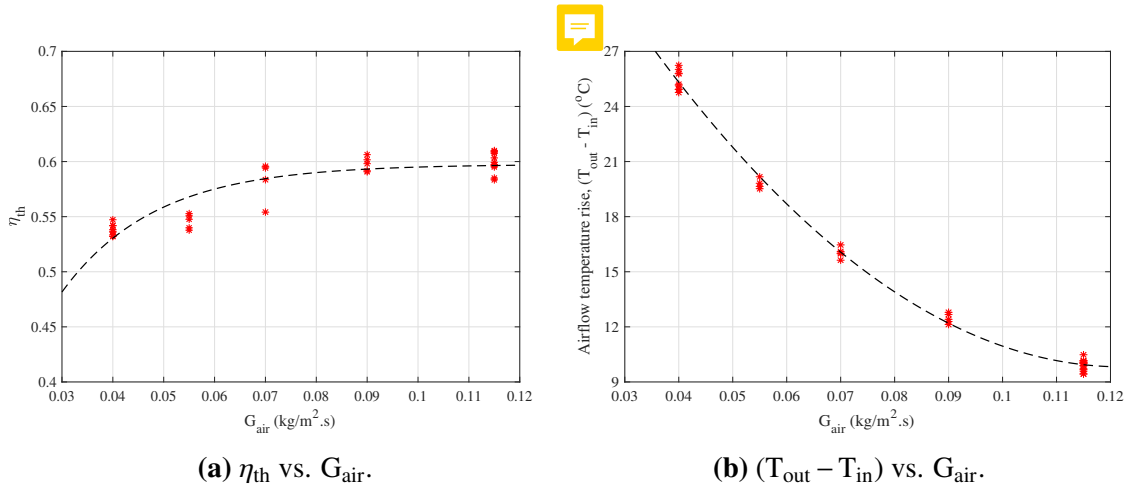


Figure 4.19: Graphs of thermal efficiency (a), and airflow temperature rise (b) at different airflow rates at nearly steady state condition.

Mirosun reflector sheet from the company Alanod was selected as the reflector material. Tempered clear glass of 4 mm in thickness with 90% transmittance was selected as the glazing cover.

The experiments were carried out in open loop configuration, where the air was blown by a 12-W with a voltage adaptor to vary the airflow rate. Experimental results were analysed for different airflow rates ranging between 0.04 and 0.115 $\text{kg/m}^2\cdot\text{s}$. Results show that the maximum outlet air temperatures at solar noon (13:00 to 14:00) varied from 40 $^{\circ}\text{C}$ at the highest airflow to 52 $^{\circ}\text{C}$ at the lowest and the thermal efficiency varied from 52% to 62%.

Results were also evaluated at nearly steady state condition, period where the direct radiation range is at maximum at solar noon, which was 800 – 900 W/m^2 . It was possible to plot the thermal efficiency curve in order to characterise the system. The parameters of the Hottel-Whillier-Bliss equation were calculated, where $F_R \eta_0$ and $F_R U_L$ are 0.65 and -3.39 respectively. The air temperature rise varied from 10 $^{\circ}\text{C}$ at the highest airflow rate to 26 $^{\circ}\text{C}$ at the lowest.



CHAPTER 5

HEAT TRANSFER MODELLING AND SIMULATION

Modelling and simulation are important tools used for predicting a solar heating system's performance. In a new solar energy application, it would be desirable to analyse theoretically any given system before the prototype fabrication (Tchinda, 2008). A thermal energy modelling specification for simulation of the proposed solar air heater under different weather conditions is important to predict its long-term performance (Shams, 2013). Therefore, this chapter aims to:

1. develop a heat transfer modelling to characterise and simulate the thermal performance of the proposed solar air heater in operation;
2. validate the model against experimental data from the tests described in Chapter 4.
3. learn how to operate and control based on model;

Consequently, the specific objectives are to:

- simulate different solar radiation levels and airflow rates;
- estimate the outlet airflow temperature;
- evaluate the system's thermal efficiency;
- determine the useful energy delivered to the airflow;

This modelling also contributes to give more understanding of the interaction between system inputs and parameters, and system outputs, indicated in Figure 5.1. The



algorithm implemented for modelling and simulation was build to run under transient state conditions.

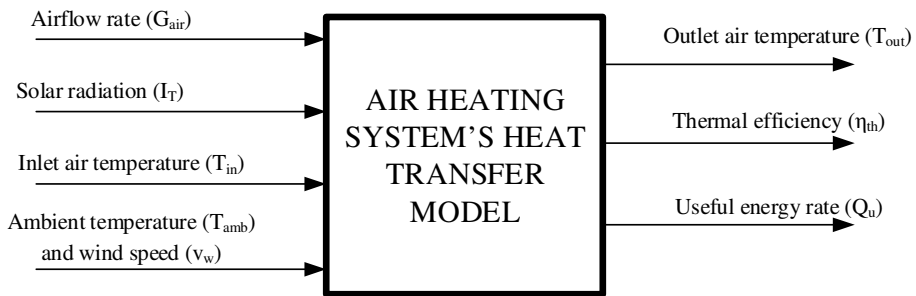


Figure 5.1: Block diagram of the heat transfer model.

5.1 Air heating system's heat transfer modelling

The first step for modelling this air heating system is to establish what are the collector's components to be modelled for simulation. In this case there are two: the first one is the absorber surface, which is where the useful heat is transferred to the airflow, and the second one is the glazing cover because it acts as a heat trap against thermal energy losses.



The next step is to state assumptions in order to simplify the model, which are listed as follows:

- Solar radiation is incident uniformly over the components' surfaces;
- Absorber and glazing temperatures are uniform;
- Thermal and physical properties of the components are independent of temperature;
- Heat transfer at the reflectors and wooden cavity, and conduction losses are neglected;
- Airflow rate is uniform through all the absorber holes;
- There is no interaction between the airflow and the air below the absorber;



The following step of the modelling depicts how the energy balance in the components are evaluated according to the following statements:



$$\begin{pmatrix} \text{Rate of internal energy in the absorber} \end{pmatrix} = \begin{pmatrix} \text{Absorbed solar radiation in the absorber} \end{pmatrix} - \begin{pmatrix} \text{Heat losses from absorber} \end{pmatrix} - \begin{pmatrix} \text{Useful heat rate to airflow} \end{pmatrix}$$

$$\begin{pmatrix} \text{Rate of internal energy in the glazing} \end{pmatrix} = \begin{pmatrix} \text{Absorbed solar radiation in the glazing} \end{pmatrix} + \begin{pmatrix} \text{Heat losses from absorber} \end{pmatrix} - \begin{pmatrix} \text{Heat losses from glazing} \end{pmatrix}$$

where the heat losses are convective and radiative. Translating the previous expressions into variables, Eqs. (5.1) and (5.2) are obtained:

$$\frac{dU_{abs}}{dt} = S_{abs} - Q_{L,1} - Q_u \quad (5.1)$$

$$\frac{dU_{glaz}}{dt} = S_{glaz} + Q_{L,1} - Q_{L,2} \quad (5.2)$$

In order to visualise how these heat rates are placed, Figure 5.2 presents the system's thermal network as an analogy to electric circuits, where absorber and glazing are nodes indicated as ① and ②, respectively. The energy input here is the total solar radiation I_T , and mathematical expressions above each resistor were used to calculate the thermal resistances.

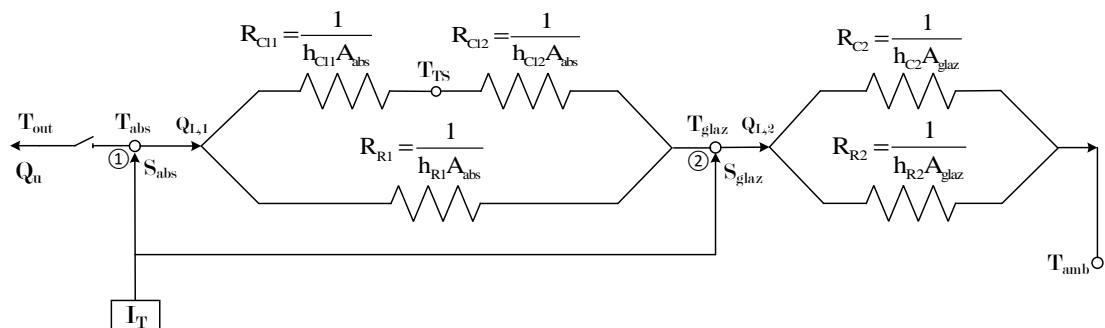


Figure 5.2: Thermal network to illustrate heat flows in the air heater, where the subscripts C and R refer to convection and radiation, respectively.

From the absorber node, the circuit path to the left indicates the flow Q_u whereas the one to the right is the path of convective (upper path) and radiative (lower path) heat losses. At the upper path there are two convective thermal resistances and one additional

node in between. This is because there is a type of convective heat transfer from the absorber to the tertiary section bottom (of temperature T_{TS}) and other from that to the glazing. These convective heat transfer types will be addressed later.

Considering that internal energy can be written in terms of temperature and applying the concept of heat loss rate as the ratio of temperature difference to the corresponding thermal resistance:



$$M_{abs}C_{p,abs}\frac{dT_{abs}}{dt} = S_{abs} - \left(\frac{T_{abs} - T_{TS}}{R_{C11}} + \frac{T_{abs} - T_{glaz}}{R_{R1}} \right) - Q_u \quad (5.3)$$

$$M_{glaz}C_{p,glaz}\frac{dT_{glaz}}{dt} = S_{glaz} + \left(\frac{T_{TS} - T_{glaz}}{R_{C12}} + \frac{T_{abs} - T_{glaz}}{R_{R1}} \right) - \frac{T_{glaz} - T_{amb}}{\left(\frac{1}{R_{C2}} + \frac{1}{R_{R2}} \right)^{-1}} \quad (5.4)$$

Substituting the thermal resistances by the mathematical expressions above each resistor in Figure 5.2 and isolating the derivative terms, Eqs. (5.5) and Eq. (5.6) are obtained.

$$\frac{dT_{abs}}{dt} = \frac{1}{M_{abs}C_{p,abs}} \left[S_{abs} - (h_{R1} + h_{C1})A_{abs}(T_{abs} - T_{glaz}) - Q_u \right] \quad (5.5)$$

$$\frac{dT_{glaz}}{dt} = \frac{1}{M_{glaz}C_{p,glaz}} \left[S_{glaz} + (h_{R1} + h_{C1})A_{abs}(T_{abs} - T_{glaz}) - (h_{R2} + h_{C2})A_{glaz}(T_{glaz} - T_{amb}) \right] \quad (5.6)$$

The next subsections describe how the absorbed solar radiation terms, convective and radiative heat transfer coefficients, useful energy rate and outlet air temperature from the thermal model were determined.

5.1.1 Absorbed solar radiation terms

The total solar radiation (I_T) incident on the concentrator's aperture is the sum of the beam (I_B) and diffuse (I_D) components. However, since only part of the diffuse radiation is exploitable by concentrators, the factor ξ must be defined, as being the fraction of total solar radiation accepted. Assuming that the diffuse distribution is isotropic, this factor can

be estimated as (Prapas et al., 1987):

$$\xi = \frac{\left(I_B + \frac{I_D}{C} \right)}{I_T} \quad (5.7)$$

 and therefore the incoming solar radiation available to reach the absorber surface is assumed to be $I_T \xi$. This portion of total solar radiation undergoes optical losses before it reaches the absorber – expressed in terms of η_0 and previously discussed in Chapter 3. Hence, S_{abs} is given by Eq. (5.8).

$$S_{\text{abs}} = I_T \xi A_{\text{apt}} \eta_0 \quad (5.8)$$

Lastly, the absorbed solar radiation by the glazing, which is based on the capacity of this component to retain the incoming radiation incident on the aperture, can be expressed as:

$$S_{\text{glaz}} = I_T A_{\text{apt}} \alpha_{\text{glaz}} \quad (5.9)$$

 where the glazing absorptivity α_{glaz} was also estimated in Chapter 3.

5.1.2 Radiative heat transfer coefficients

The radiative heat transfer coefficient from the absorber to the glazing h_{R1} can be evaluated by Eq. (5.10):

$$h_{R1} = \varepsilon_{\text{eff}} \sigma (T_{\text{abs}}^2 + T_{\text{glaz}}^2) (T_{\text{abs}} + T_{\text{glaz}}) \quad (5.10)$$

 where ε_{eff} is the effective emissivity, a radiative property developed by Rabl (1976b) for a CPC comprised by specular reflectors. Although the solar air heater to be modelled here is not a CPC, such methodology of assessing h_{R1} was used, given the similarity of both geometries. The calculation of ε_{eff} takes into account: the radiative properties of the absorber, reflector and glazing, such as emissivity and reflectivity, and the concentrator's geometric concentration ratio.

The radiative heat transfer coefficient from the glazing to the ambient h_{R2} was evaluated by Eq. (5.11):

$$h_{R2} = \varepsilon_{\text{glaz}} \sigma (T_{\text{glaz}}^2 + T_{\text{amb}}^2) (T_{\text{glaz}} + T_{\text{amb}}) \quad (5.11)$$

where the glazing is considered to emit radiation to the ambient only, which absorbs all the emitted energy from that, thus acting as a blackbody (Duffie and Beckman, 2013).

5.1.3 Convective heat transfer coefficients

The estimation of h_{C1} takes two stages of heat transfer: the first is from the absorber to the bottom of the tertiary section and the second is from there to the glazing cover. In the first stage, as the hotter surface is at the top inside the cavity, no convective current will be developed naturally, since the lighter mass of air is always above the heavier. Such type of heat transfer is called pure conduction downwards and then the Nusselt number is a unity (Cengel and Turner, 2004). Due to this phenomenon, air layers are formed below the absorber surface inside the cavity (indicated in Figure 5.3). The convective heat transfer coefficient for this stage is given by:



$$h_{C11} = \frac{k_{\text{air}}}{H_{\text{TS}}} Nu_{C11} = \frac{k_{\text{air}}}{H_{\text{TS}}} \quad (5.12)$$

where the air thermal conductivity k_{air} is calculated as (Rabl, 1976b):

$$k_{\text{air}} = 4.86 \cdot 10^{-4} T^{0.7} \quad (5.13)$$

with k_{air} evaluated at the average temperature between T_{abs} and T_{TS} .

The second stage involves the heat transfer from the air at the surroundings of the glazing to this component by natural convection. Hence, the convective heat transfer coefficient h_{C12} is calculated as:



$$h_{C12} = \frac{k_{\text{air}}}{W_{\text{glaz}}} Nu_{C12} = a(Ra)^b \quad (5.14)$$

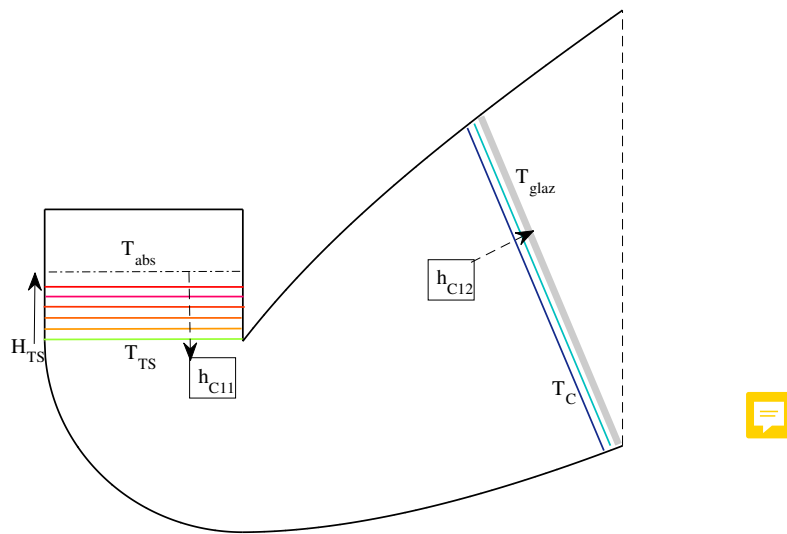


Figure 5.3: Convective heat transfer taking place within the tertiary section and at the surroundings of the glazing (whose coefficients are h_{C11} and h_{C12} , respectively).

where the parameters a and b depend on the geometry and the flow regime (Cengel and Turner, 2004). Assuming laminar flow and an average glazing inclination, $a = 0.56$ and $b = 1/4$ (Rabl, 1976b). The Rayleigh number is defined by Eq.(5.15):

$$Ra = \frac{g\beta_{th}\bar{W}_{glaz}(T_c - T_{glaz})Pr}{\nu_{air}^2} \quad (5.15)$$

where: T_c is the temperature near the glazing assumed to be the average between T_{TS} and T_{glaz} (shown in Figure 5.3); the volume expansion coefficient β_{th} is $1/T_c$ as the air is considered an ideal gas; the Prandtl number Pr is assumed to be a constant value and \bar{W}_{glaz} and ν_{air} are the glazing characteristic length and the air kinematic viscosity, respectively, which are calculated as follows:

$$\bar{W}_{glaz} = \frac{L_{col}W_{glaz}}{2(L_{col} + W_{glaz})} \quad (5.16)$$

$$\nu_{air} = 9.76 \cdot 10^{-10} T^{1.7} \quad (5.17)$$

where, in this stage, k_{air} and ν_{air} is evaluated at T_c . Substituting Eqs. (5.13), (5.17) and (5.15) in Eq. (5.14) and thus making arrangements, h_{C12} can be obtained after the above

considerations:

$$h_{C12} = 14.2 \left(\frac{T_c - T_{glaz}}{W_{glaz}} \right)^{0.25} T_c^{-0.4} \quad (5.18)$$

In order to find T_{TS} and then calculate h_{C11} and h_{C12} , an auxiliary equation must be proposed. From the thermal network, it is possible to state that the convective heat loss rate from the absorber to the tertiary section bottom is equivalent to the rate from that position to the glazing, which is presented by Eq. (5.19):

$$h_{C11} A_{abs} (T_{abs} - T_{TS}) = h_{C12} A_{glaz} (T_{TS} - T_{glaz}) \quad (5.19)$$

This non-linear equation has only T_{TS} as unknown variable, requiring then an iterative procedure to solve it. In this case, the Newton's Method was applied (Hoffman, 2001). After finding T_{TS} , the values of h_{C11} and h_{C12} are calculated and, finally, the convective heat transfer coefficient h_{C1} is obtained:

$$h_{C1} = \frac{1}{\frac{1}{h_{C11}} + \frac{1}{h_{C12}}} \quad (5.20)$$

It is important to highlight that when $H_{TS} = 0$, it would not be possible to calculate h_{C11} . However, this issue can be overcome by making $h_{C11} = 0$, replacing T_{TS} by T_{abs} and proceeding to calculate h_{C12} with no need to apply any iterative method. In this case, h_{C1} will be equivalent to h_{C12} .

In order to calculate the heat transfer coefficient from glazing to ambient h_{C2} , it is assumed that the convection loss is forced by the wind. Therefore, the estimation of it is given by Eq. (5.21) (Incropera et al., 2006):

$$h_{C2} = \frac{k_{air}}{W_{glaz}} Nu_{C2} = \frac{k_{air}}{W_{glaz}} (0.664 Re_w^{1/2} Pr^{1/3}) \quad (5.21)$$

where it is assumed that k_{air} and Re_w are evaluated at T_{amb} , and the Reynolds number

based on the wind speed is:

$$Re_w = \frac{v_w W_{glaz}}{\nu_{air}} \quad (5.22)$$

with ν_{air} also evaluated at T_{amb} .

5.1.4 Useful energy rate and outlet air temperature

The estimation of the useful energy rate was given in Eq. (4.3). It should be noted that the outlet air temperature is unknown in the modelling. Therefore, the understanding of the heat transfer from the absorber to the airflow becomes necessary to estimate T_{out} . To do so, another way of assessing Q_u is by using fundamentals of heat exchange (Incropera et al., 2006), which is proposed by means of Eq. (5.23):

$$Q_u = h_{HX} A'_{abs} \Delta T_m \quad (5.23)$$

where A'_{abs} is the absorber surface area excluding holes:

$$A'_{abs} = A_{abs}(1 - \varphi_p) \quad (5.24)$$

and ΔT_m is called logarithmic mean temperature difference, which needs to take into account the absorber, inlet and outlet air temperatures, calculated as:

$$\Delta T_m = \frac{(T_{abs} - T_{out}) - (T_{abs} - T_{in})}{\ln\left(\frac{T_{abs} - T_{out}}{T_{abs} - T_{in}}\right)} \quad (5.25)$$

Combining Eqs. (4.3) and (5.23), and then isolating T_{out} , Eq. (5.26) is obtained.

$$T_{out} = T_{abs} - (T_{abs} - T_{in}) \left[1 - \exp\left(-\frac{h_{HX}(1 - \varphi_p)}{G_{air}C_{p,air}}\right) \right] \quad (5.26)$$

The convective heat transfer coefficient for the air flowing through a perforated plate

(h_{HX}) is calculated by the correlation developed by Kutscher (1994) for a normal flow:

$$h_{HX} = \frac{k_{air}}{\varphi_h} Nu_h = \frac{k_{air}}{\varphi_h} \left[2.75 \left(\frac{\ell}{\varphi_h} \right)^{-1.2} Re_h^{0.43} \right] \quad \blacksquare \quad (5.27)$$

where the hole pitch and the hole diameter at the absorber are calculated based on the hole area A_h in Eqs. (5.28) and (5.29), respectively, whereas Figure 5.4 illustrates a drawing of carbon fibre fabric to indicate the geometry parameters used in the modelling.

$$\ell = \sqrt{\frac{A_h}{\varphi_p}} \quad \blacksquare \quad (5.28)$$

$$\varphi_h = \sqrt{A_h} \quad (5.29)$$

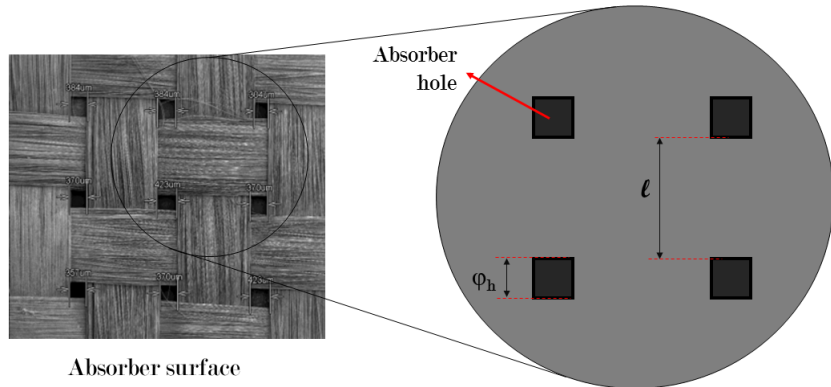


Figure 5.4: Carbon fibre magnified image and drawing for indication of geometric parameters.

Furthermore, the Reynolds number in the holes is:

$$Re_h = \frac{v_h \varphi_h}{\nu_{air}} \quad (5.30)$$

with the average air velocity in the holes as:

$$v_h = \frac{G_{air}}{d_{air} \varphi_p} \quad (5.31)$$

The air physical properties d_{air} , k_{air} and ν_{air} are evaluated at a temperature a_{med} to be the average between T_{in} and T_{out} so the value of h_{HX} can be estimated. Therefore, the calculation of T_{out} from Eq. (5.26) is a function of the same temperature, which requires

an iterative method to solve it. In this case, the Fixed Point Iteration Method was then applied (Hoffman, 2001).

5.2 Simulation results and discussion

5.2.1 Simulation settings

After describing all the variables and parameters, the method for solving the system of two ordinary differential equations (ODEs) must be defined, which is the explicit Euler method for initial condition. It derives from the Taylor series truncated at the second term where the solution of the model is fairly accurate for small values of time step (Hoffman, 2001). The ODEs system is then shown in Eq. (5.32):

$$\begin{cases} T_{\text{abs}}(t_{m+1}) = T_{\text{abs}}(t_m) + \Delta t \cdot F_3(T_{\text{abs}}(t_m), T_{\text{glaz}}(t_m)) \\ T_{\text{glaz}}(t_{m+1}) = T_{\text{glaz}}(t_m) + \Delta t \cdot F_4(T_{\text{abs}}(t_m), T_{\text{glaz}}(t_m)) \end{cases} \quad (5.32)$$

where the functions F_3 and F_4 are the right hand sides of Eqs. (5.5) and (5.6), respectively. The initial conditions are the data collected at 9 am of each day of experiment and the time step Δt was set as 1 s. The algorithm used for modelling and simulation was implemented in Matlab® and it followed the steps depicted as follows:

Step 1: Input geometric parameters, optical efficiency data (η_0) and the components' physical properties;

Step 2: Input solar radiation (I_T), ambient temperature (T_{amb}), inlet air temperature (T_{in}) and wind speed (v_w) data;

Step 3: Set time step (Δt), simulation time ($t_s = 8\text{h}$), initial conditions and initiate time index $m = 1$;

Step 4: Run current time (t_m);

Step 5: Calculate the terms S_{abs} , S_{glaz} , h_{R1} , h_{R2} and h_{C2} ;

Step 6: Apply Newton's method to calculate T_{TS} ;

Step 7: Use T_{TS} to calculate h_{C1} ;

Step 8: Apply Fixed Point Iteration to calculate T_{out} ;

Step 9: Use $T_{out}(t_m)$ to calculate $Q_u(t_m)$ and $\eta_{th}(t_m)$;

Step 10: Calculate $Q_{L,1}(t_m)$, $T_{abs}(t_{m+1})$ and $T_{glaz}(t_{m+1})$;

Step 11: Check if t_{m+1} is the final time. If so, end the simulation. If not, do $m = m + 1$ and go back to step 4.

Table 5.1: Model parameters values used in the heat transfer modelling.

Symbol	Model parameter	Value
$C_{p,abs}$	Absorber heat capacity	1000 J/kg.K
M_{abs}	Absorber mass	0.075 kg
A'_{abs}	Absorber area without holes	0.17 m ²
φ_p	Carbon fibre porosity	4.19%
A_h	Hole area	0.147 mm ²
ℓ	Hole pitch	1.87 mm
φ_h	Hole diameter	0.383 mm
$C_{p,glaz}$	Glazing heat capacity	880 J/kg.K
M_{glaz}	Glazing mass	3.7 kg
n_{glaz}	Glazing refraction index	1.526
K_{ext}	Glaz. extinction coefficient	4 m ⁻¹
\overline{W}_{glaz}	Glaz. characteristic length	0.11 m
ε_{eff}	Effective emissivity	0.68
$C_{p,air}$	Air heat capacity	1000 J/kg.K
Pr	Prandtl number	0.72
ξ	Intercept factor	0.93
Δt	Time step	1 s

Experimental data from Chapter 4 were used to validate the heat transfer model.

The purpose of validation is to determine if the model is an accurate representation of this air heating system (Banks and Carson, 1987). In order to measure the model accuracy in predicting experimental data, an error estimator was used: the mean absolute error (MAE), defined as the percentage mean of absolute errors relative to individual observations. Such estimator is calculated by Eq. (5.33)(Pujol-Nadal et al., 2015):

$$MAE(\%) = \frac{100}{N_{obs}} \sum_{i=1}^{N_{obs}} \left| \frac{X_{exp,i} - X_{sim,i}}{X_{exp,i}} \right| \quad (5.33)$$

where $X_{exp,i}$ is the experimental (observed) value and $X_{sim,i}$ is the simulated (estimated) value of the same variable. Another way to measure accuracy is to assess the frequency

and magnitude of residues (difference between experimental and simulated values) generated by the mathematical model. A positive residue indicates model underestimation while a negative one indicates overestimation.

5.2.2 Model validation

The model validation consisted of comparing the simulated variables T_{out} and Q_u to the experimental ones under the same conditions of the experimental results presented in Chapter 4.

Validation of experimental results at low airflow rate

Figure 5.5(a) shows the graphs of solar radiation data, experimental and simulated results of the test on 9th June ($G_{air} = 0.04 \text{ kg/m}^2.\text{s}$), whereas Figures 5.5(b) and 5.5(c) present the residue plot in relation to the simulated values. On this clear sky day the calculated MAE for T_{out} and Q_u are 1.9% and 5.3%, respectively. During the hour of highest solar radiation (13:00 – 14:00) the residues are mostly between $\pm 1^\circ\text{C}$ and $\pm 20 \text{ W/m}^2$. It was found that 70% of the residues have magnitude of $\pm 1^\circ\text{C}$; 80% are between $\pm 20 \text{ W/m}^2$ and 60% of the predictions are underestimated (positive residues).

Validation of experimental results at low-med airflow rate

Figure 5.6(a) shows solar radiation, experimental and simulated data of the test on 22nd June ($G_{air} = 0.055 \text{ kg/m}^2.\text{s}$). On this clear sky day with intermittent clouds, the calculated MAE regarding T_{out} and Q_u are 2.2% and 6.0%, respectively. Although it was a day with sudden variation in solar radiation at different moments, the model predicted the outputs which most of the residues are between -0.5 and 1 $^\circ\text{C}$, and -10 and 30 W/m^2 , except in two periods: after 16:00, when the decay of I_T lasted 10 minutes before rising to the natural trend; and shortly before 14:00, when I_T became highly unstable. These events might explain why the model underestimated the outputs by more than 1.5 $^\circ\text{C}$ and 30 W/m^2 . From Figures 5.6(b) and 5.6(c), 85% of the residues have magnitude of $\pm 1^\circ\text{C}$; 90% of the residues are between $\pm 30 \text{ W/m}^2$ and 88% of the predictions are

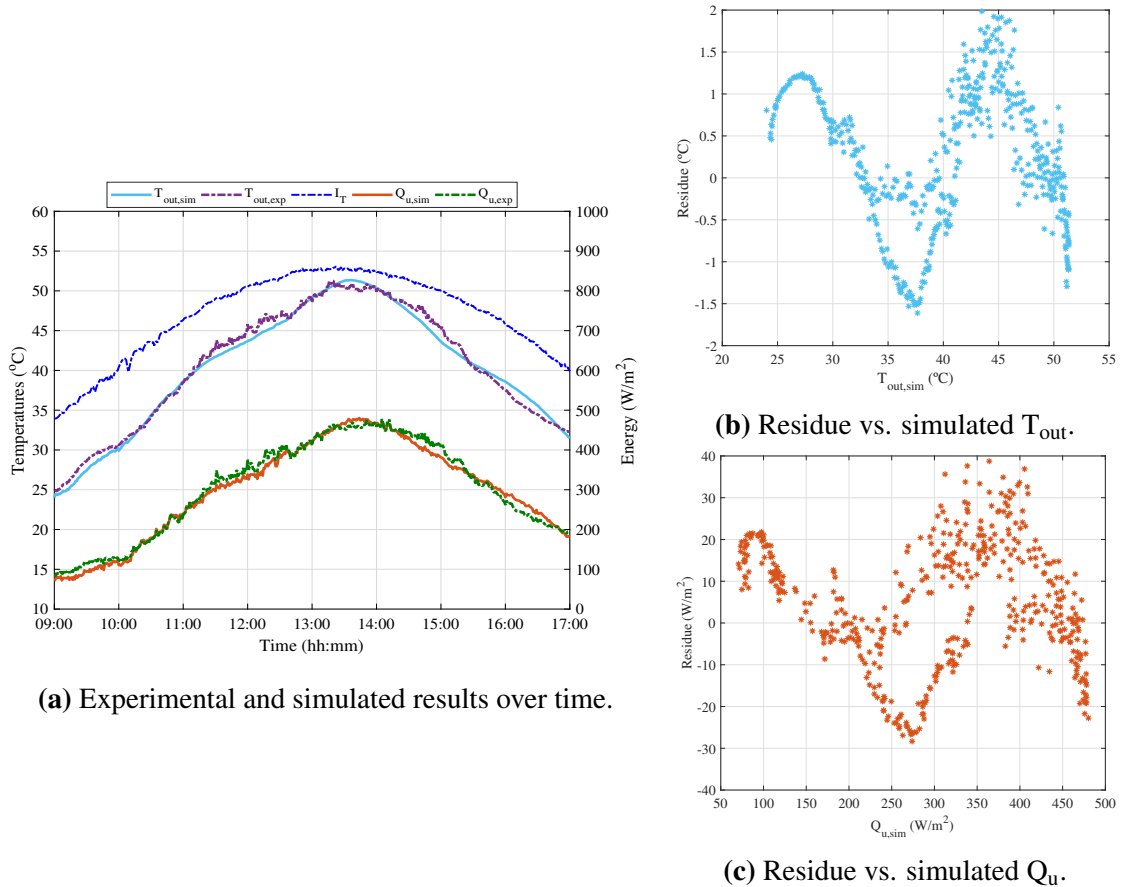


Figure 5.5: (a) Experimental and simulated results, (b) residues of T_{out} , and (c) residues of Q_u from 09th June at 0.04 kg/m².s.

underestimated.

Validation of experimental results at medium airflow rate

Figure 5.7(a) shows the graphs of solar radiation data, experimental and simulated results of the test on 29th May ($G_{air} = 0.07 \text{ kg/m}^2.\text{s}$), whereas Figures 5.7(b) and 5.7(c) present the residue plot in relation to the simulated values. On this clear sky day with intermittent clouds mainly before 12:00, the calculated MAE for T_{out} and Q_u are 1.6% and 4.9%, respectively. The outputs also did not fall substantially due to the solar radiation's sudden variation. In this case, the model underestimated 88% of the predictions, where 95% of the residues are between ± 1 °C and 93% are between ± 30 W/m². It is also noted that the maximum residue is less than 1.2 °C and less than 40 W/m².

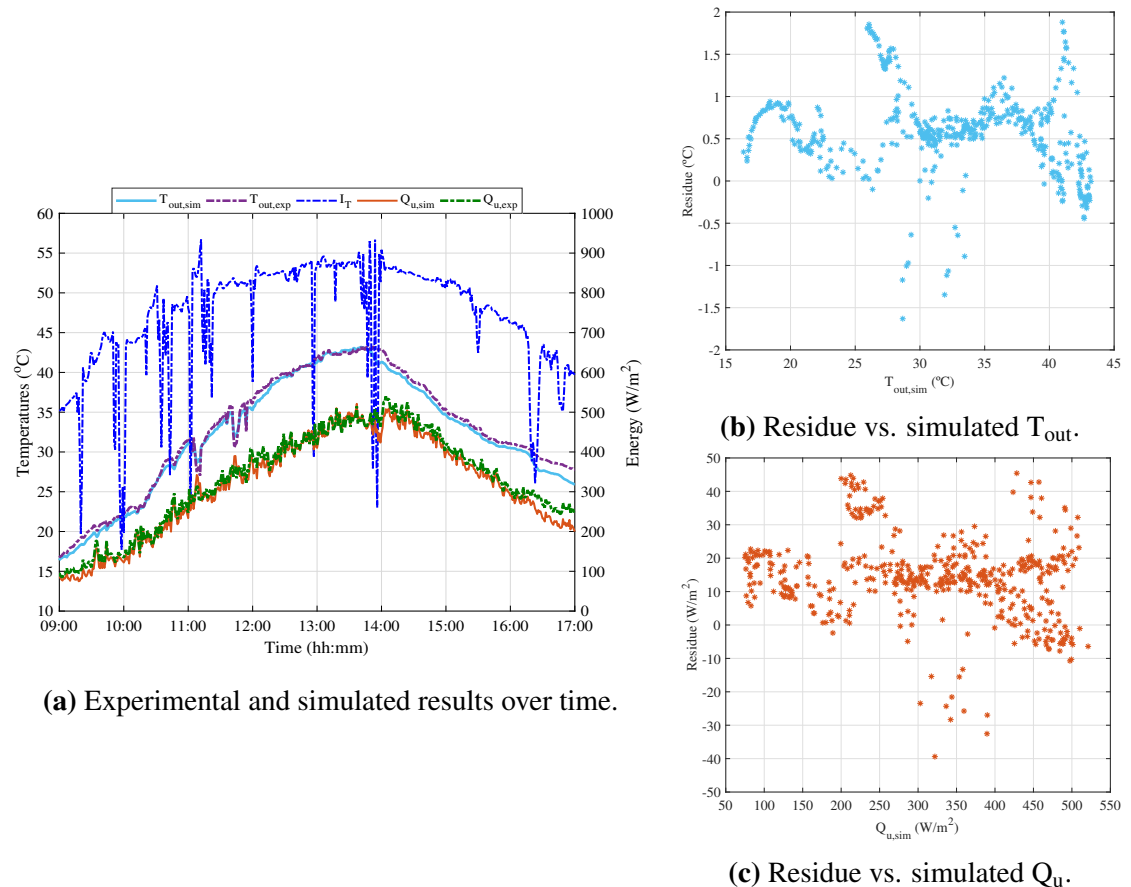


Figure 5.6: (a) Experimental and simulated results, (b) residues of T_{out} , and (c) residues of Q_u from 22nd June at $0.055 \text{ kg/m}^2\cdot\text{s}$.

Validation of experimental results at med-high airflow rate

Figure 5.8(a) shows solar radiation, experimental and simulated data of the test on 29th May ($G_{air} = 0.09 \text{ kg/m}^2\cdot\text{s}$). The calculated MAE for T_{out} and Q_u are 2.5% and 13.7%, respectively. The model prediction is the least accurate in this case due to high variations in I_T throughout the day. From 14:00 to 15:00 the model overestimated the experimental data by more than 2 °C and more than 56 W/m² and up to 130 W/m². This large difference can be due to any unknown experimental fluctuation during the test. From Figures 5.8(b) and 5.8(c), the simulated outputs were also underestimated compared to the experimental results in 79% of the cases. It was found that 70% of the residues have magnitude of ± 1 °C and 75% are between ± 40 W/m².

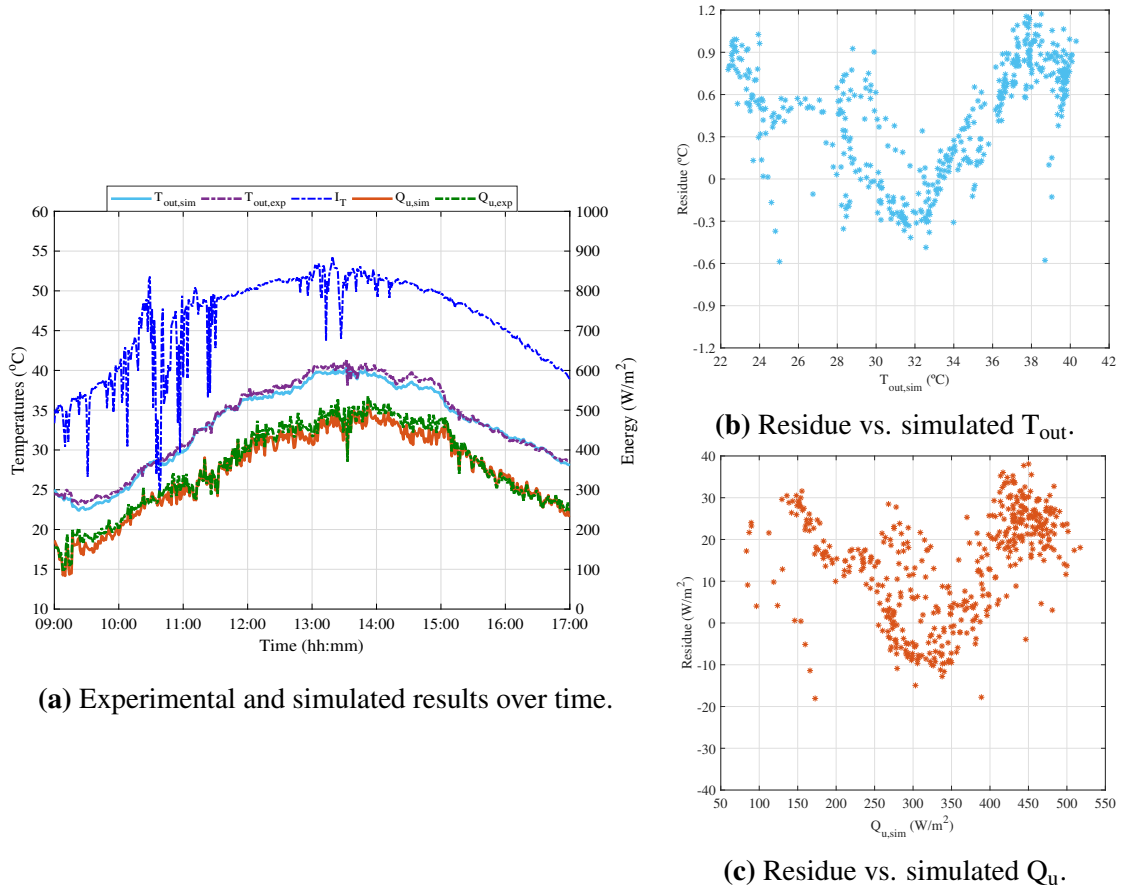


Figure 5.7: (a) Experimental and simulated results, (b) residues of T_{out} , and (c) residues of Q_{u} from 29th May at $0.07 \text{ kg/m}^2 \cdot \text{s}$.

Validation of experimental results at high airflow rate

Figure 5.9(a) shows the graphs of solar radiation data, experimental and simulated results of the test on 28th June ($G_{\text{air}} = 0.115 \text{ kg/m}^2 \cdot \text{s}$), whereas Figures 5.9(b) and 5.9(c) present the residue plot in relation to the simulated values. On this clear sky day the calculated MAE for T_{out} and Q_{u} are 1.1% and 7.0%, respectively. In this case, the model underestimated 78% of the predictions, where 83% of the residues are between $\pm 0.6 \text{ }^{\circ}\text{C}$ and 83% are between $\pm 30 \text{ W/m}^2$. After 14:00 the model mostly underestimated Q_{u} by 20 to 40 W/m^2 . It is also noticed that the maximum residue is less than $1.0 \text{ }^{\circ}\text{C}$ and less than 40 W/m^2 .

Hence, from the calculated MAE and residue plots, there was no effect of the airflow rate and time of operation on the model prediction. To check if solar radiation has influence on the model prediction, all residues were plotted against I_T and shown in Fig-

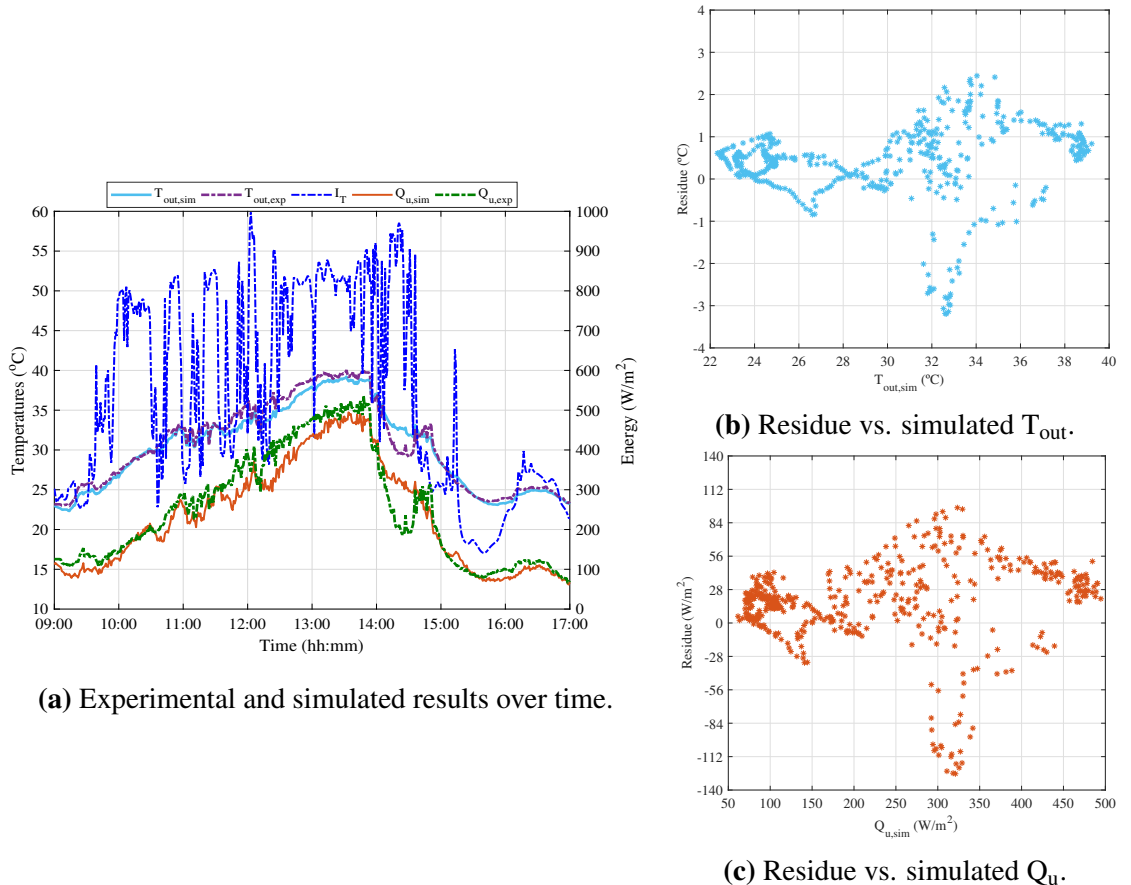


Figure 5.8: Experimental and simulated results from 31st May at $0.09 \text{ kg/m}^2 \cdot \text{s}$.

ure 5.10. It can be seen that the residues are concentrated on the region of I_T above 600 W/m^2 and most of them are between $\pm 2.0 \text{ }^\circ\text{C}$ and $\pm 50 \text{ W/m}^2$. The highest residues were observed for days with high intermittent clouds.

Another way to analyse these residue data is by plotting the cumulative frequency distribution of each simulated output, as shown in Figure 5.11. From the cumulative distributions, 95% of the data predicted have residues between $\pm 2 \text{ }^\circ\text{C}$ and $\pm 50 \text{ W/m}^2$. It was also found that 65% of the predictions are underestimated, which highlights the underestimation of the simulation results at most of the time.

5.2.3 Thermal characterisation from simulation results

After validation, the heat transfer model was used to characterise the system's thermal performance under the conditions of clear sky days at transient state. The inputs ranges, of which this system can be modelled, are depicted as follows:

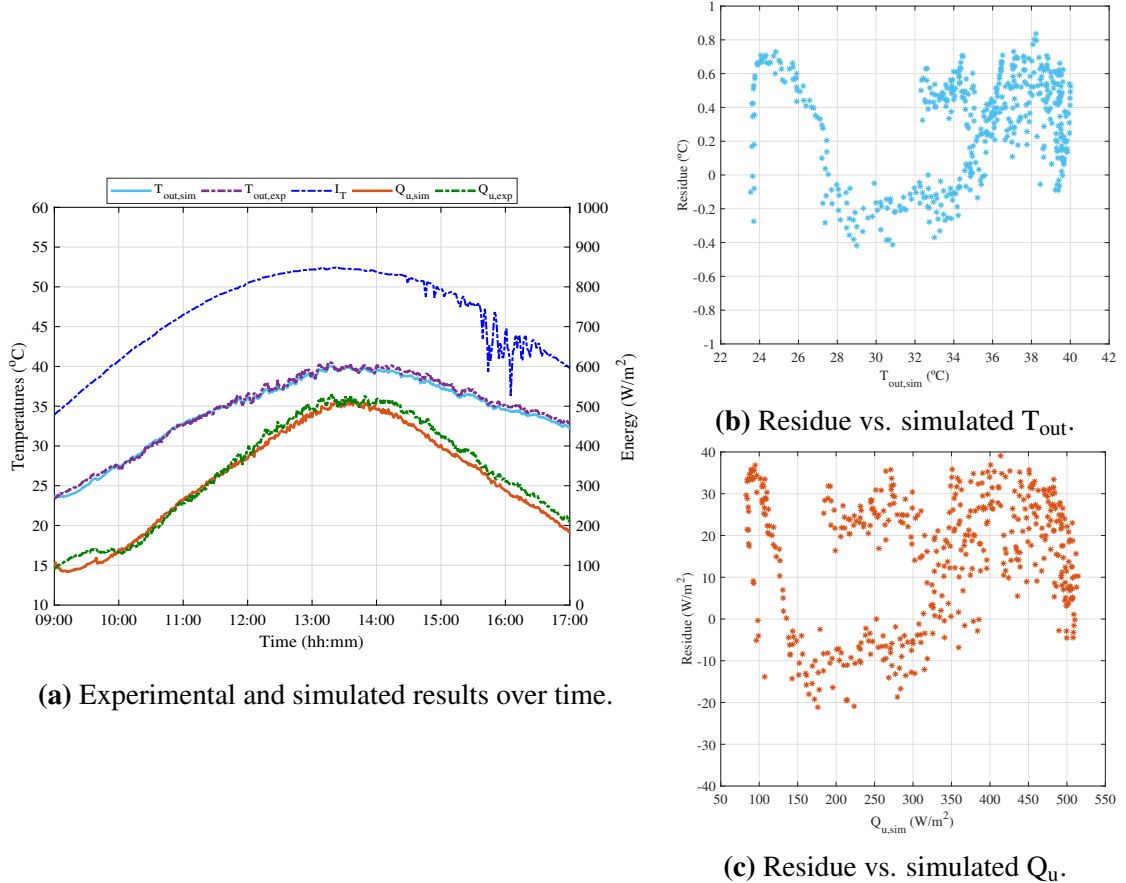


Figure 5.9: (a) Experimental and simulated results, (b) residues of T_{out} , and (c) residues of Q_u from 28th June at $0.115 \text{ kg/m}^2 \cdot \text{s}$.

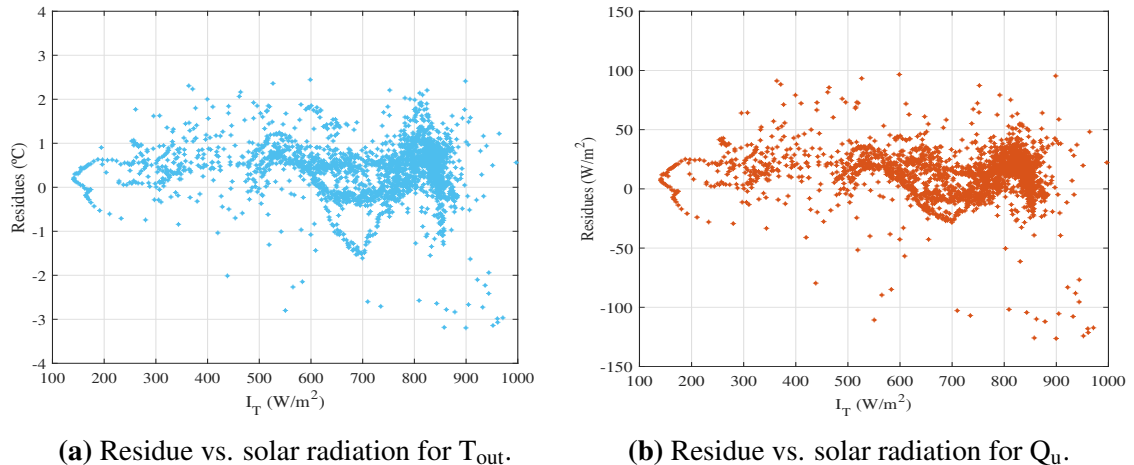
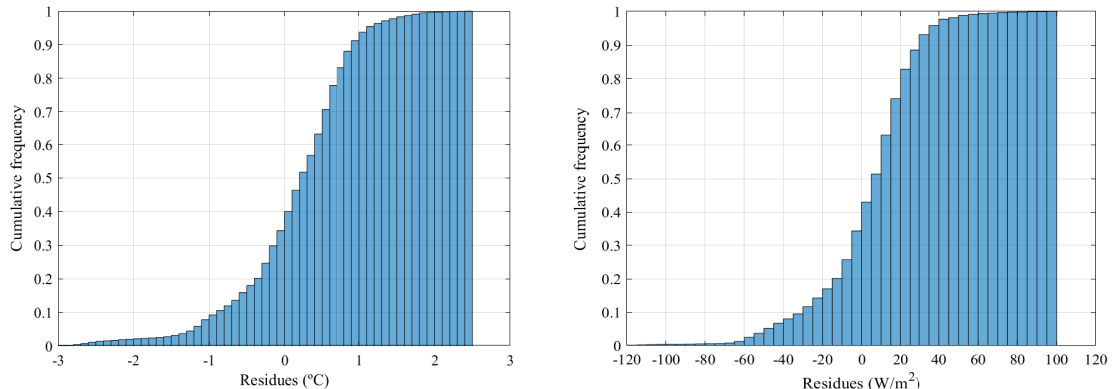


Figure 5.10: Residues vs. solar radiation for (a) T_{out} , and (b) Q_u .

Solar radiation: $500 - 1000 \text{ W/m}^2$, where the lowest limit corresponds to the airflow temperature increase at the beginning of the operation;

Mass airflow rate: $0.04 - 0.12 \text{ kg/(m}^2 \cdot \text{s)}$, where the limits are coincident to the ones of the tests;



(a) Cumulative frequency of residues from T_{out} . (b) Cumulative frequency of residues from Q_u .

Figure 5.11: Residual cumulative frequency distribution of (a) T_{out} , and (b) Q_u .

Ambient and inlet air temperature: $20 - 30 \text{ }^{\circ}\text{C}$, which includes all the measured data on clear sky days;

Wind speed: $0 - 10 \text{ m/s}$, to include all the data taken from Met Eireann website.

To characterise this air heating system with one concentrator, a particular clear sky day (30th June) was taken to represent the results. The simulation was performed at the five different airflow rates and the correspondent graphs of T_{out} were plotted in Figure 5.12. All the temperature profiles reached their maximum levels in the hour of highest solar radiation ($I_T = 860 \text{ W/m}^2$).

With the simulation data obtained, Figure 5.13 presents the surface and contour plot to fit the air temperature rise (ΔT) as function of the solar radiation and airflow rate. In overall, the air temperature rise is observed from I_T above 500 W/m^2 and increases in a nearly linear was as more energy is coming into the system. The opposite effect is noticed as the airflow is increased because ΔT is inversely proportional to G_{air} . Temperature rises above $27 \text{ }^{\circ}\text{C}$ can be obtained at airflow rate of $0.04 \text{ kg/(m}^2\text{.s)}$ when I_T is above 860 W/m^2 .

To express these results in terms of useful energy, Figure 5.14 shows surface and contour plot of this output against air temperature rise and airflow rate. Q_u increases as G_{air} and ΔT become higher as it is directly proportional to both inputs. The temperature increases more at lower airflow rates but at the cost of delivering low useful energy rate, which highlights the trade-off between energy collected and outlet air temperature.

Figure 5.15 shows simulated data takes under the same conditions depicted in Chap-

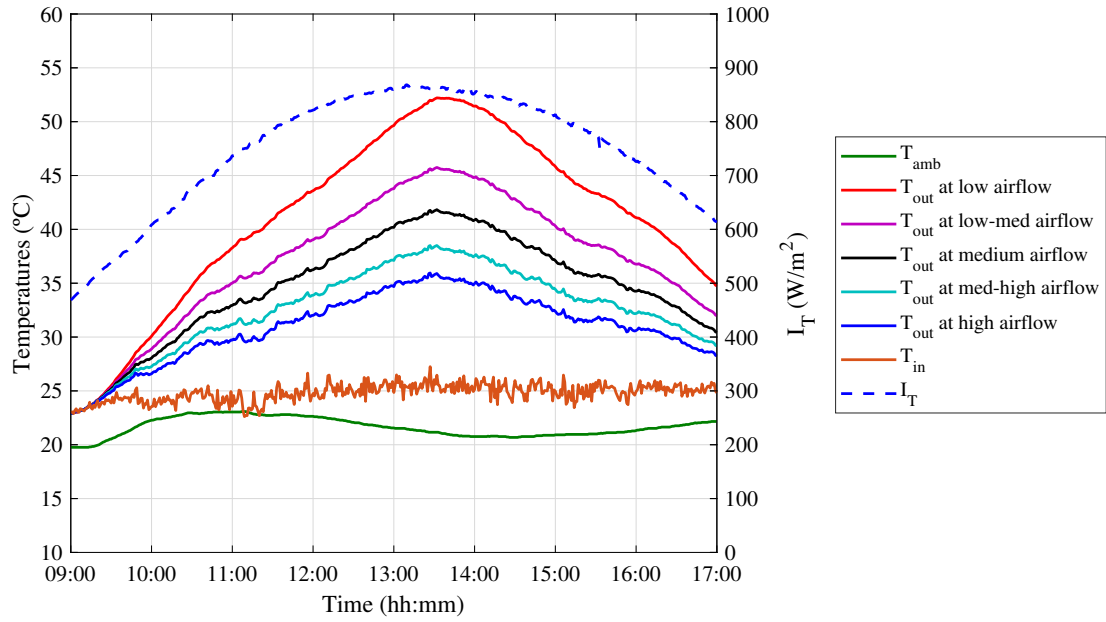


Figure 5.12: Simulated T_{out} at the five different airflow rates used in the tests, under conditions of 30th June.

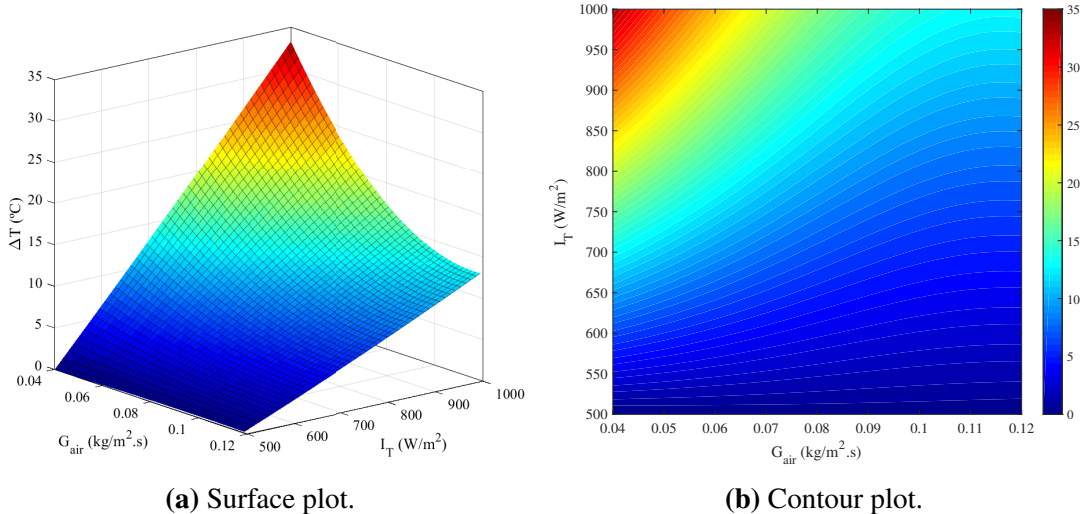


Figure 5.13: (a) Surface and (b) contour plot of air temperature rise vs. solar radiation and airflow rate.

ter 4 at nearly steady state. Comparing the parameters of the Hottel-Whillier-Bliss equation, $F_R \eta_0$ and $F_R U_L$ calculated by the thermal model are 0.64 and -3.02, respectively, with relative difference of 2% and 10% in relation to the parameters of the experimental data. The coefficient of correlation of the simulated curve is 0.9.

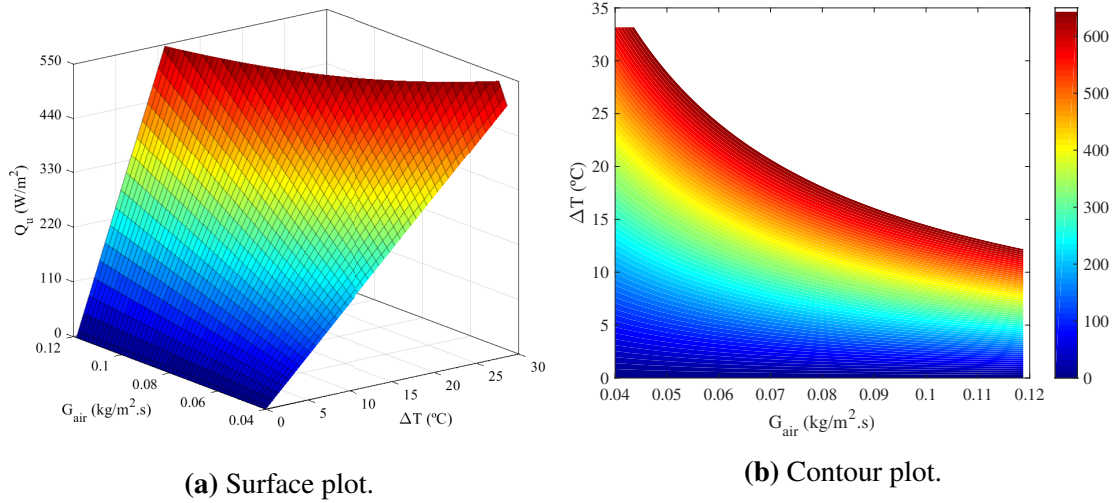


Figure 5.14: (a) Surface and (b) contour plot of useful energy vs. air temperature rise and airflow rate.

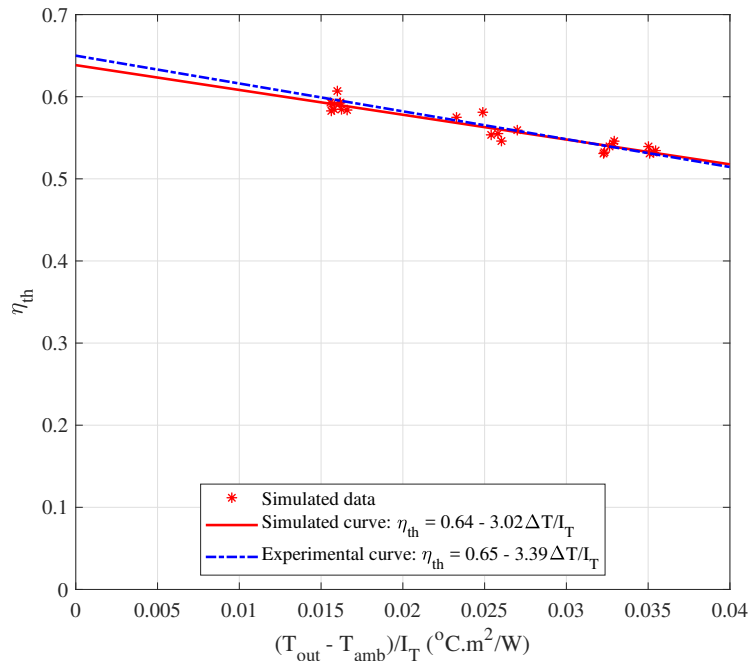


Figure 5.15: Thermal efficiency curves for experimental and simulated data.

5.3 Chapter Summary

A thermal modelling and simulation of the proposed solar air heating system was developed and it was validated against experimental data. Results show that, in general, the heat transfer model underestimates 65% of the data and 95% of the residues generated are between ± 2 °C and ± 50 W/m². In overall, the mean absolute error in terms of temperature was found to be 2% and in terms of useful energy was 8%. After validation,

the system has been characterised within a certain range of inputs.

The model was also used to simulate results at nearly steady state condition. The thermal efficiency curve was plotted and compare it to the experimental one. The parameters of the Hottel-Whillier-Bliss equation $F_R \eta_0$ and $F_R U_L$ calculated by the thermal model are 0.64 and -3.02, with relative difference of 2% and 10%, respectively, in relation to the parameters of the experimental data.

CHAPTER 6

REMAINING WORK

The remaining work to complete the PhD is listed as follows:

- Complete Chapter 2 literature review. Topics in building integration, thermal modelling and thermal modelling for other types of solar collectors will be included;
- Add the topic of optical and design analysis for building integrated systems considering different shapes of concentrators and truncation levels (Chapter 3);
- Run experiments on the prototype where the inlet air temperature ranges between 30 to 40 °C by using an electric air heater (Chapter 4). From the results, validate the heat transfer model (Chapter 5);
- Perform a Computational Fluid Dynamics (CFD) modelling to better understand the heat transfer within the concentrator. Simulations will be undertaken to investigate the effect of the tertiary section height and the collector's size (Chapter 5);
- Manuscript writing under the title "Optical performance of building integrated asymmetric compound parabolic concentrators for air heating";
- Manuscript writing related to the experimental results with the pre-heater and further thermal modelling validation;
- Manuscript writing related to CFD modelling and simulation results.

REFERENCES

- Abdullahi, B., R.K. AL-Dadah, S. Mahmoud, and R. Hood (2015). “Optical and thermal performance of double receiver compound parabolic concentrator”. In: *Applied Energy* 159, pp. 1–10. doi: [10.1016/j.apenergy.2015.08.063](https://doi.org/10.1016/j.apenergy.2015.08.063).
- Abu-Bakar, Siti Hawa, Firdaus Muhammad-Sukki, Roberto Ramirez-Iniguez, Tapas Kumar Mallick, Abu Bakar Munir, Siti Hajar Mohd Yasin, and Ruzairi Abdul Rahim (2014). “Rotationally asymmetrical compound parabolic concentrator for concentrating photovoltaic applications”. In: *Applied Energy* 136, pp. 363–372. doi: [10.1016/j.apenergy.2014.09.053](https://doi.org/10.1016/j.apenergy.2014.09.053).
- Alanod (2016). *MIRO-SUN*. URL: <https://www.alanod.com/en/reflection/miro-sun/>.
- Ali, Imhamed M. Saleh, Tadhg S. O’Donovan, K.S. Reddy, and Tapas K. Mallick (2013). “An optical analysis of a static 3-D solar concentrator”. In: *Solar Energy* 88, pp. 57–70. doi: [10.1016/j.solener.2012.11.004](https://doi.org/10.1016/j.solener.2012.11.004).
- Ali, Imhamed M. Saleh, T. Srihari Vikram, Tadhg S. O’Donovan, K.S. Reddy, and Tapas K. Mallick (2014). “Design and experimental analysis of a static 3-D elliptical hyperboloid concentrator for process heat applications”. In: *Solar Energy* 102, pp. 257–266. doi: [10.1016/j.solener.2014.01.031](https://doi.org/10.1016/j.solener.2014.01.031).
- Alta, Deniz, Emin Bilgili, C. Ertekin, and Osman Yaldiz (2010). “Experimental investigation of three different solar air heaters: Energy and exergy analyses”. In: *Applied Energy* 87.10, pp. 2953–2973. doi: [10.1016/j.apenergy.2010.04.016](https://doi.org/10.1016/j.apenergy.2010.04.016).

- Banks, J. and J. S. Carson (1987). "Applying the simulation process". In: *Proceedings of the 19th Conference on Winter Simulation*. ACM Press. doi: 10.1145/318371.318386.
- Bellos, E., D. Korres, C. Tzivanidis, and K.A. Antonopoulos (2016). "Design, simulation and optimization of a compound parabolic collector". In: *Sustainable Energy Technologies and Assessments* 16, pp. 53–63. doi: 10.1016/j.seta.2016.04.005.
- Benrejeb, Raouf, Olfa Helal, and Bechir Chaouachi (2015). "Optical and thermal performances improvement of an ICS solar water heater system". In: *Solar Energy* 112, pp. 108–119. doi: 10.1016/j.solener.2014.11.011.
- (2016). "Study of the effect of truncation on the optical and thermal performances of an ICS solar water heater system". In: *Solar Energy* 132, pp. 84–95. doi: 10.1016/j.solener.2016.02.057.
- Carvalho, M.J., M. Collares-Pereira, J.M. Gordon, and A. Rabl (1985). "Truncation of CPC solar collectors and its effect on energy collection". In: *Solar Energy* 35.5, pp. 393–399. doi: 10.1016/0038-092x(85)90127-6.
- Cengel, Yunus A. and Robert H. Turner (2004). *Fundamentals of Thermal-Fluid Sciences*. 2nd ed. McGraw-Hill. ISBN: 0-07-245426-1.
- Clearwater Composites, LLC (2016). *Properties of Carbon Fiber*. URL: <https://www.clearwatercomposites.com/resources/properties-of-carbon-fiber>.
- Dev, Rahul, Sabah A. Abdul-Wahab, and G.N. Tiwari (2011). "Performance study of the inverted absorber solar still with water depth and total dissolved solid". In: *Applied Energy* 88.1, pp. 252–264. doi: 10.1016/j.apenergy.2010.08.001.
- Devices, Delta-T (2018). *DL2e Data Logger*. URL: <https://www.delta-t.co.uk/product/dl2e/>.
- Duffie, John A. and William A. Beckman (2013). *Solar Engineering of Thermal Processes*. 4th ed. John Wiley & Sons, Inc. ISBN: 978-0-470-87366-3.
- Duffy, Dean G. (2016). *Advanced Engineering Mathematics with MATLAB*. 4th ed. Chapman and Hall/CRC. ISBN: 9781498739641.

- Eames, P. C., B. Norton, and A. F. Kothdiwala (1996). “The state of the art in modelling line-axis concentrating solar energy collectors”. In: *Renewable Energy* 9.1-4, pp. 562–567. doi: [10.1016/0960-1481\(96\)88352-2](https://doi.org/10.1016/0960-1481(96)88352-2).
- Eames, P.C. and B. Norton (1993). “Validated, unified model for optics and heat transfer in line-axis concentrating solar energy collectors”. In: *Solar Energy* 50.4, pp. 339–355. doi: [10.1016/0038-092x\(93\)90028-m](https://doi.org/10.1016/0038-092x(93)90028-m).
- Eames, P.C, M Smyth, and B Norton (2001). “The experimental validation of a comprehensive unified model for optics and heat transfer in line-axis solar energy systems”. In: *Solar Energy* 71.2, pp. 121–133. doi: [10.1016/s0038-092x\(01\)00027-5](https://doi.org/10.1016/s0038-092x(01)00027-5).
- First Glass, Ltd (2016). *Toughened Glass*. URL: http://www.firstglass.ie/products_toughened_glass.html.
- Francesconi, Marco and Marco Antonelli (2018). “A CFD analysis to investigate thermal losses in a panel composed of several CPC concentrators”. In: *Thermal Science and Engineering Progress* 5, pp. 278–288. doi: [10.1016/j.tsep.2017.12.005](https://doi.org/10.1016/j.tsep.2017.12.005).
- Goswami, D. Yogi (2015). *Principles of Solar Engineering*. Ed. by Taylor & Francis Group. 3rd ed. CRC Press. ISBN: 9781466563780.
- Harmim, A., M. Merzouk, M. Boukar, and M. Amar (2012). “Mathematical modeling of a box-type solar cooker employing an asymmetric compound parabolic concentrator”. In: *Solar Energy* 86.6, pp. 1673–1682. doi: [10.1016/j.solener.2012.03.020](https://doi.org/10.1016/j.solener.2012.03.020).
- Hoffman, Joe D. (2001). *Numerical Methods For Engineers And Scientists*. 2nd ed. New York, USA: Marcel Dekker. ISBN: 0-8247-0443-6.
- Incropera, Frank P., David P. DeWitt, Theodore L. Bergman, and Adrienne S. Lavine (2006). *Fundamentals of Heat and Mass Transfer*. 6th ed. John Wiley & Sons. ISBN: 978-0471457282.
- Jaaz, Ahed Hameed, Husam Abdulrasool Hasan, Kamaruzzaman Sopian, Mohd Hafidz Bin Haji Ruslan, and Saleem Hussain Zaidi (2017). “Design and development of compound parabolic concentrating for photovoltaic solar collector: Review”. In: *Renewable and Sustainable Energy Reviews* 76, pp. 1108–1121. doi: [10.1016/j.rser.2017.03.127](https://doi.org/10.1016/j.rser.2017.03.127).

- Joven, Ronald (2012). "Thermal properties of carbon fiber/epoxy composites with different fabric weaves". In: *SAMPE International Symposium*.
- Kalogirou, Soteris A. (2004). "Solar thermal collectors and applications". In: *Progress in Energy and Combustion Science* 30.3, pp. 231–295. doi: [10.1016/j.pecs.2004.02.001](https://doi.org/10.1016/j.pecs.2004.02.001).
- Kienzlen, V., J. M. Gordon, and J. F. Kreider (1988). "The Reverse Flat Plate Collector: A Stationary, Nonevacuated, Low-Technology, Medium-Temperature Solar Collector". In: *Journal of Solar Energy Engineering* 110.1, p. 23. doi: [10.1115/1.3268232](https://doi.org/10.1115/1.3268232).
- Kothdiwala, A. F., P. C. Eames, and B. Norton (1997). "Experimental analysis and performance of an asymmetric inverted absorber compound parabolic concentrating solar collector at various absorber gap configurations". In: *Renewable Energy* 10.2-3, pp. 235–238. doi: [10.1016/0960-1481\(96\)00071-7](https://doi.org/10.1016/0960-1481(96)00071-7).
- Kothdiwala, A. F., P. C. Eames, B. Norton, and A. Zacharopolous (1999). "Technical note: Comparison between inverted absorber asymmetric and symmetric tubular-absorber compound parabolic concentrating solar collectors". In: *Renewable Energy* 18.2, pp. 277–281. doi: [10.1016/s0960-1481\(98\)00786-1](https://doi.org/10.1016/s0960-1481(98)00786-1).
- Kothdiwala, A. Farouk, P. C. Eames, and B. Norton (1996). "Optical performance of an asymmetric inverted absorber compound parabolic concentrating solar collector". In: *Renewable Energy* 9.1-4, pp. 576–579. doi: [10.1016/0960-1481\(96\)88355-8](https://doi.org/10.1016/0960-1481(96)88355-8).
- Kutscher, C. F. (1994). "Heat Exchange Effectiveness and Pressure Drop for Air Flow Through Perforated Plates with and without Crosswind". In: *Journal of Heat Transfer* 116.2, pp. 391–399. doi: [10.1115/1.2911411](https://doi.org/10.1115/1.2911411).
- Mallick, T and P Eames (2007). "Design and fabrication of low concentrating second generation PRIDE concentrator". In: *Solar Energy Materials and Solar Cells* 91.7, pp. 597–608. doi: [10.1016/j.solmat.2006.11.016](https://doi.org/10.1016/j.solmat.2006.11.016).
- Mallick, Tapas K., Philip C. Eames, and Brian Norton (2006). "Non-concentrating and asymmetric compound parabolic concentrating building façade integrated photovoltaics: An experimental comparison". In: *Solar Energy* 80.7, pp. 834–849. doi: [10.1016/j.solener.2005.05.011](https://doi.org/10.1016/j.solener.2005.05.011).

- Mallick, Tapas K., Philip C. Eames, and Brian Norton (2007). “Using air flow to alleviate temperature elevation in solar cells within asymmetric compound parabolic concentrators”. In: *Solar Energy* 81.2, pp. 173–184. doi: [10.1016/j.solener.2006.04.003](https://doi.org/10.1016/j.solener.2006.04.003).
- McIntire, W. R. (1979). “Truncation of nonimaging cusp concentrators”. In: *Solar Energy* 23.4, pp. 351–355. doi: [10.1016/0038-092x\(79\)90130-0](https://doi.org/10.1016/0038-092x(79)90130-0).
- MetEireann (2018). *Historical Data*. URL: <https://www.met.ie/climate/available-data/historical-data>.
- Mills, David R. and John E. Giutronich (1978). “Asymmetrical non-imaging cylindrical solar concentrators”. In: *Solar Energy* 20.1, pp. 45–55. doi: [10.1016/0038-092x\(78\)90140-8](https://doi.org/10.1016/0038-092x(78)90140-8).
- Norton, B., P. C. Eames, and Y. P. Yadav (1991). “Symmetric and asymmetric linear compound parabolic concentrating solar energy collectors: The state-of-the-art in optical and thermo-physical analysis”. In: *International Journal of Ambient Energy* 12.4, pp. 171–190. doi: [10.1080/01430750.1991.9675201](https://doi.org/10.1080/01430750.1991.9675201).
- Prapas, D. E., B. Norton, and S. D. Probert (1987). “Optics of parabolic-trough, solar-energy collectors, possessing small concentration ratios”. In: *Solar Energy* 39.6, pp. 541–550. doi: [10.1016/0038-092x\(87\)90061-2](https://doi.org/10.1016/0038-092x(87)90061-2).
- Pujol-Nadal, Ramon, Víctor Martínez-Moll, Fabienne Sallaberry, and Andreu Mojà-Pol (2015). “Optical and thermal characterization of a variable geometry concentrator using ray-tracing tools and experimental data”. In: *Applied Energy* 155, pp. 110–119. doi: [10.1016/j.apenergy.2015.06.005](https://doi.org/10.1016/j.apenergy.2015.06.005).
- Qin, Hua, Chengxin Lei, Hanfa Liu, Yong Wang, and Wenfeng Yuan (2013). “Optical design of an aspherical cylinder-type reflecting solar concentrator”. In: *Energy* 57, pp. 751–758. doi: [10.1016/j.energy.2013.05.059](https://doi.org/10.1016/j.energy.2013.05.059).
- Rabl, Ari (1976a). “Comparison of solar concentrators”. In: *Solar Energy* 18.2, pp. 93–111. doi: [10.1016/0038-092x\(76\)90043-8](https://doi.org/10.1016/0038-092x(76)90043-8).
- (1976b). “Optical and Thermal Properties of Compound Parabolic Concentrators”. In: *Solar Energy* 18.6, pp. 497–511. doi: [10.1016/0038-092x\(76\)90069-4](https://doi.org/10.1016/0038-092x(76)90069-4).

- Rabl, Ari (1985). *Active Solar Collectors and Their Applications*. Oxford University Press. 518 pp. ISBN: 0195035461.
- Ratismith, Wattana, Anusorn Inthongkhum, and John Briggs (2014). “Two non-tracking solar collectors: Design criteria and performance analysis”. In: *Applied Energy* 131, pp. 201–210. doi: [10.1016/j.apenergy.2014.06.030](https://doi.org/10.1016/j.apenergy.2014.06.030).
- Sarmah, Nabin, Bryce S. Richards, and Tapas K. Mallick (2011). “Evaluation and optimization of the optical performance of low-concentrating dielectric compound parabolic concentrator using ray-tracing methods”. In: *Applied Optics* 50.19, pp. 3303–3310. doi: [10.1364/ao.50.003303](https://doi.org/10.1364/ao.50.003303).
- Sellami, Nazmi and Tapas K. Mallick (2013). “Optical efficiency study of PV Crossed Compound Parabolic Concentrator”. In: *Applied Energy* 102, pp. 868–876. doi: [10.1016/j.apenergy.2012.08.052](https://doi.org/10.1016/j.apenergy.2012.08.052).
- Sellami, Nazmi, Tapas K. Mallick, and David A. McNeil (2012). “Optical characterisation of 3-D static solar concentrator”. In: *Energy Conversion and Management* 64, pp. 579–586. doi: [10.1016/j.enconman.2012.05.028](https://doi.org/10.1016/j.enconman.2012.05.028).
- Shams, Nassif (2013). “Design of a Transpired Air Heating Solar Collector with an Inverted Perforated Absorber and Asymmetric Compound Parabolic Concentrator”. PhD thesis. Dublin, Ireland: Dublin Institute of Technology. doi: [10.21427/D7NK67](https://doi.org/10.21427/D7NK67).
- Shams, S. M. N., M. Mc Keever, S. Mc Cormack, and B. Norton (2016). “Design and experiment of a new solar air heating collector”. In: *Energy* 100, pp. 374–383. doi: [10.1016/j.energy.2015.12.136](https://doi.org/10.1016/j.energy.2015.12.136).
- Smyth, M., P. McGarrigle, P. C. Eames, and B. Norton (2005). “Experimental comparison of alternative convection suppression arrangements for concentrating integral collector storage solar water heaters”. In: *Solar Energy* 78.2, pp. 223–233. doi: [10.1016/j.solener.2004.06.004](https://doi.org/10.1016/j.solener.2004.06.004).
- Souliotis, M., P. Quinlan, M. Smyth, Y. Tripanagnostopoulos, A. Zacharopoulos, M. Ramirez, and P. Yianoulis (2011). “Heat retaining integrated collector storage solar water heater with asymmetric CPC reflector”. In: *Solar Energy* 85.10, pp. 2474–2487. doi: [10.1016/j.solener.2011.07.005](https://doi.org/10.1016/j.solener.2011.07.005).

- Tchinda, Réné (2008). “Thermal behaviour of solar air heater with compound parabolic concentrator”. In: *Energy Conversion & Management* 49, pp. 529–540. doi: [10.1016/j.enconman.2007.08.004](https://doi.org/10.1016/j.enconman.2007.08.004).
- Tian, Meng, Yuehong Su, Hongfei Zheng, Gang Pei, Guiqiang Li, and Saffa Riffat (2018). “A review on the recent research progress in the compound parabolic concentrator (CPC) for solar energy applications”. In: *Renewable and Sustainable Energy Reviews* 82, pp. 1272–1296. doi: [10.1016/j.rser.2017.09.050](https://doi.org/10.1016/j.rser.2017.09.050).
- Tiwari, G.N. and Sangeeta Suneja (1998). “Performance evaluation of an inverted absorber solar still”. In: *Energy Conversion and Management* 39.3-4, pp. 173–180. doi: [10.1016/s0196-8904\(96\)00227-0](https://doi.org/10.1016/s0196-8904(96)00227-0).
- Tripanagnostopoulos, Y, P Yianoulis, S Papaefthimiou, and S Zafeiratos (2000). “CPC Solar Collectors With Flat Bifacial Absorbers”. In: *Solar Energy* 69.3, pp. 191–203. doi: [10.1016/s0038-092x\(00\)00061-x](https://doi.org/10.1016/s0038-092x(00)00061-x).
- Ustaoglu, Abid, Mustafa Alptekin, Junnosuke Okajima, and Shigenao Maruyama (2016). “Evaluation of uniformity of solar illumination on the receiver of compound parabolic concentrator (CPC)”. In: *Solar Energy* 132, pp. 150–164. doi: [10.1016/j.solener.2016.03.014](https://doi.org/10.1016/j.solener.2016.03.014).
- Winston, Roland (1974). “Principles of solar concentrators of a novel design”. In: *Solar Energy* 16.2, pp. 89–95. doi: [10.1016/0038-092x\(74\)90004-8](https://doi.org/10.1016/0038-092x(74)90004-8).
- Winston, Roland, Juan C. Minano, and Pablo G. Benitez (2005). *Nonimaging Optics*. Academic Press. ISBN: 0-12-759751-4. doi: [10.1016/B978-0-12-759751-5.X5000-3](https://doi.org/10.1016/B978-0-12-759751-5.X5000-3).
- Wu, S S, C D Boley, J N Florando, M M LeBlanc, W H Lowdermilk, S M Rubenchik, and J R Stanley (2012). *Deep Penetration in Aerospace Composite Materials Using Near-Infrared Laser Radiation*. Tech. rep. Livermore, United States: Lawrence Livermore National Lab. (LLNL). doi: [10.2172/1059098](https://doi.org/10.2172/1059098).
- Wu, Yupeng (2009). “Thermal Management of Concentrator Photovoltaics”. PhD thesis. Warwick, UK: University of Warwick. URL: <http://go.warwick.ac.uk/wrap/3218>.

- Zacharopoulos, A., P. C. Eames, D. McLarnon, and B. Norton (2000). “Linear Dielectric Non-Imaging Concentrating Covers For PV Integrated Building Facades”. In: *Solar Energy* 68.5, pp. 439–452. doi: [10.1016/s0038-092x\(00\)00013-x](https://doi.org/10.1016/s0038-092x(00)00013-x).